2015

Optimization of Molecular Beacon-Based Multicomponent Probes for Analysis of Nucleic Acids

Maria Stancescu
University of Central Florida

OPTIMIZATION OF MOLECULAR BEACON-BASED MULTICOMPONENT PROBES FOR ANALYSIS OF NUCLEIC ACIDS

by

MARIA STANCESCU
B.E. University Politehnica of Bucharest, 1996
M.S. Carleton University, 2004

A dissertation submitted in partial fulfillment of the requirements
for the degree of Doctor of Philosophy
in the Department of Chemistry
in the College of Science
at the University of Central Florida
Orlando, Florida

Fall Term
2015

Major Professor: Dmitry M. Kolpashchikov

ABSTRACT

Detection of single nucleotide substitutions (SNS) in DNA and RNA has a growing importance in biology and medicine. One traditional approach for recognition of SNS takes advantage of hybridization probes that bind target nucleic acids followed by measuring ΔT_m, the difference in melting temperatures of matched and mismatched hybrids. The approach enables SNS differentiation at elevated temperatures (usually 40-65^oC) often only in a narrow range of <10^oC and requires high-resolution melting devices. Here we demonstrate that a specially designed DNA probe (X sensor) can broaden ΔT_m from ~10^oC to ~16^oC and distinguish SNS in the interval of ~5-40^oC. Therefore, there is no need for heating or measuring T_m for accurate SNS differentiation. Our data indicate that this wide differentiation range is in part due to the non-equilibrium hybridization conditions.

Further we explored the idea that it is possible to improve the performance of an X sensor operable in close to equilibrium conditions by shifting its operability to non-equilibrium conditions. One way to achieve this is to introduce as many as possible structured ligands in analyte's dissociated state. Here we show that by introducing the maximum possible conformational constraints in X probe it is possible to shift its operation to non-equilibrium conditions and to improve its selectivity at temperatures <15^oC. Thus, this work points towards a new strategy for the design of highly selective hybridization sensors which operate in non-equilibrium conditions at close to room temperature. The X sensors could be utilized in qPCR, microarrays, as well as RNA analysis in living cells and for ambient temperature point-of-care diagnostics.

In the last part of this work, X sensors were used in real time detection of PCR products. The sensors were optimized to operate in PCR buffer with optimal Mg^{2+} concentration. They were able to detect the target amplicon together with nonspecific products. The results presented here suggest that X sensors might be adopted for real time PCR format.

Theses for defense:

1. It is possible to design hybridization probes that differentiates matched from mismatched analyte in a broad interval of ambient temperatures (5-40^{o}C).
2. It is possible to broaden the temperature interval in which a hybridization probe differentiates SNS, by operating under non-equilibrium conditions.
3. X sensors can detect specific analyte and differentiate it from non-specific analyte in a regular PCR buffer.

ACKNOWLEDGMENTS

I would like to thank my advisor Prof. Dmitry Kolpashchikov for the support and guidance he has provided throughout these last years of my PhD studies. His patience and dedication to his graduate and undergraduate students has been an inspiration to me. I am very grateful for being a member of his group.

I would like to thank Dr. Jef Hooyberghs of the VITO Institute, Belgium for the help with simulation of equilibrium conditions in the first chapter of this work. Also, I am very thankful to the members of my dissertation committee: Dr. Christian A. Clausen, Dr. Michael L. Shuler, Dr. Alexander Balaeff, and Dr. Eda Koculi, whose comments and suggestions have always been helpful.

I would also like to thank the past and present members of Kolpashchikov group for their support and for being such great people with whom I had the pleasure of sharing a lab. They are: Dr. Yulia Gerasimova, Dr. Evan Cornett, Martin O'Steen, Carlos Ledezma, Nanami Kikuchi, Hillary Bengtson, Alexandra Smith and Rebekah Karadeema.

Last but not least, I would like to thank my family, father and parents-in-law for their support and encouragement during these years. Special thanks are going to my husband Radu, and sons Andrei and Vlad. I am very grateful for their love and patience, without which I would not have been able to complete my PhD studies.

TABLE OF CONTENT

LIST OF FIGURES ix

LIST OF TABLES xii

LIST OF ABBREVIATIONS xiii

CHAPTER 1: GENERAL INTRODUCTION 1

Figures and tables 4

CHAPTER 2: BROADENING ΔT_M: DIFFERENTIATION OF A SINGLE NUCLEOTIDE SUBSTITUTION IN A WIDE TEMPERATURE RANGE UNDER NON-EQUILIBRIUM HYBRIDIZATION CONDITIONS 7

Introduction 7

Materials and Methods 9

Reagents 9

Fluorescence Assay 10

Results 12

Probe Design 12

SNS differentiation by the three types of hybridization probes 14

Non-equilibrium condition contributes to the broadening of differentiation temperature range 16

Discussion 17

Figures and tables 21

CHAPTER 3: OPTIMIZATION OF MB-BASED MULTICOMPONENT PROBES FOR ANALYSIS OF NUCLEIC ACIDS WITH NEARLY LINEAR STRUCTURE 31

Introduction 31

Materials and Methods 33

Reagents 33

Fluorescence Assay 34

Results and Discussion 36

Probe Design 36

Comparison of the three hybridization probes in SNS recognition 37

X_inh sensors' performance in SNS recognition 38

Kinetic responses of the three types of hybridization probes 40

Fluorescence responses of X sensors with stem-forming analyte binding arms 43

Fluorescence response of X_inh sensor to a C->T mutation 49

Recognition of different types of SNS by X sensor 50

Figures and tables 52

CHAPTER 4: MB-BASED MULTICOMPONENT PROBES FOR rt PCR APPLICATIONS 72

Introduction 72

Materials and Methods 75

Reagents..... 75

Real-time PCR Experiments 76

Melting Curves Recordings 77

Results and Discussion 78

Conclusion..... 84

Figures and Tables..... 86

REFERENCES..... 94

LIST OF FIGURES

Figure 1. Schematic representation of a fluorescent biosensor..... 4

Figure 2. Working mechanism of a molecular beacon..... 5

Figure 3. Working mechanism of an X sensor..... 6

Figure 4. Different types of hybridization probes: design and fluorescent melting profiles. 21

Figure 5. Differentiation range for the three types of hybridization probes. 22

Figure 6. Fluorescent response of X1 probes with various lengths *m* strands to the presence of DNA analytes 23

Figure 7. Differentiation range for all X1_m sensors. 24

Figure 8. Stabilization of fluorescent signal for the probe-analyte complexes depending on equilibration time given at each temperature. 25

Figure 9. Structures of analyte-probe complexes and analytes used in this study. 26

Figure 10. Optimization of fluorescence assay at RT. 27

Figure 11. Native polyacrylamide gel electrophoresis (nPAGE) of tetrapartite complex formation. 28

Figure 12. SNS recognition by different types of hybridization probes. 52

Figure 13. Differentiation range for the three types of hybridization probes. 53

Figure 14. X_inh sensor's fluorescence dependence on the length of m-analyte binding arms (y). 54

Figure 15. X_inh_short sensor's fluorescence dependence on the length of m-analyte binding arms (y). 55

Figure 16. Temperature range discrimination for different X_inh sensors. 56

Figure 17.Temperature range discrimination for different X_inh_short sensors. 57

Figure 18. Kinetic responses of the three types of hybridization probes. 58

Figure 19. Folding of DNA analytes at 37°C under experimental conditions and the X probe's hybridization position. 59

Figure 20. Melting curves of m stem-forming or linear m DNA sensors hybridized to target DNA. 60

Figure 21. Melting curves of hybrids containing stemless or stem-forming 8 nt-long m-analyte binding arms. 61

Figure 22. Melting curves of hybrids containing stemless or stem-forming 9 nt-long m-analyte binding arms. 62

Figure 23. Kinetic responses of X_inh sensors containing stemless or stem-forming 9 nt-long m-analyte binding arms. 63

Figure 24. Fluorescence responses of X_inh sensor to a C -> T mutation. 64

Figure 25. Recognition of different types of SNS by the X_inh sensor. 65

Figure 26. Differentiation range dependence on the length of binding arms for X_udg sensors. 86

Figure 27. Differentiation range dependence on Mg^{2+} concentration in Phusion® HF buffer for X_udg sensors. 87

Figure 28. Performance of X_udg sensor in Phusion® HF buffer 2 mM Mg^{2+}. 88

Figure 29. Performance of X_inh sensors for recognition of inh analytes in Phusion® HF buffer 2 mM Mg^{2+}. 89

Figure 30. Performance of X_inh sensor in detection of rt PCR amplified products. 90

LIST OF TABLES

Table 1. Sequences of oligonucleotides used in the study of three different DNA hybridization probes. 29

Table 2. Temperature characteristics for probe-analyte complexes. 30

Table 3. Sequences of oligonucleotides used in the X_inh sensor study. 66

Table 4. Temperature characteristics for different probe-analyte complexes. 67

Table 5. Temperature characteristics for X_inh sensor-analyte complexes containing long (X_F_inh) or short (X_F_inh_short) f-analyte binding arm. 68

Table 6. Temperature characteristics for X_inh probe-analyte complexes containing 8 nt stem-forming m-analyte binding arm. 69

Table 7. Temperature characteristics for X_inh probe-analyte complexes containing 9 nt stem-forming m-analyte binding arm. 70

Table 8. Temperature characteristics for probe-analyte complexes containing different SNS 71

Table 9. Sequences of oligonucleotides used in the rt PCR amplification study. 91

Table 10. Melting temperature dependence on $MgCl_2$ concentration for X_udg sensor-analyte complexes. 92

Table 11. Melting temperatures of probe-synthetic analyte complexes and PCR amplified products 93

LIST OF ABBREVIATIONS

AS	Associated state
BDP	Binary DNA sensor
DNA	Deoxyribonucleic acid
dNTP	Deoxynucleotide triphosphate
ds	Double stranded
DS	Dissociated state
DX	Double crossover
FRET	Fluorescence resonance energy transfer
4WJ	Four-way junction
LOD	Limit of detection
M	Mutant
MB	Molecular beacon
Mtb	*Mycobacterium tuberculosis*
NA	Nucleic acid
PAGE	Polyacrylamide gel electrophoresis
PCR	Polymerase chain reaction
rcf	Relative centrifuge force
RNA	Ribonucleic acid
rt	Real time
SNP	Single nucleotide polymorphism
SNS	Single nucleotide substitution
ss	Single stranded
UMB	Universal molecular beacon
WT	Wild-type

CHAPTER 1: GENERAL INTRODUCTION

Sensors are devices that respond to physical or chemical stimuli and produce detectable signals. Mainly, they consist of two components: target recognition and signal transduction (Figure 1). As an extension, fluorescent biosensors are sensors which contain a biological or biologically derived target recognition element and a physicochemical transduction element capable of converting molecular recognition events into detectable fluorescence signals [1]. Classic examples of fluorescent biosensors are the hybridization probes first introduced by Tyagi and Kramer in 1996 called molecular beacons (MB) probes [2] (Figure 2). A standard MB is a single-stranded DNA molecule with a hairpin structure containing a loop and a stem. The loop portion of the molecule complementary to a specific target is the sensing element. The stem portion consisting of five or six complementary arm sequences to which are attached a fluorophore (F) and a quencher (Q) can be considered the physicochemical transducer. In the absence of the target, the stem keeps the two moieties in close proximity such that fluorescence of the fluorophore is quenched by FRET mechanism (contact quenching). In the presence of target, MB probe undergoes a spontaneous conformational change which forces the F/Q pair to move away from each other giving rise to fluorescence upon photoexcitation of the fluorophore (Figure 2). Importantly, excess MB remains quenched and since it doesn't contribute to fluorescence signal, there is no need to separate it from the mixture. MB probes distinguish mismatches over a broader temperature range than unstructured probes do, because of their stem and loop structure which stabilizes the analyte's dissociated state (DS) [3].

X sensors are MB-based multicomponent sensors first reported by our lab for sequence-specific genotyping of short DNA fragments [4-6] (Figure 3).They consist of a universal molecular beacon (UMB), and two adaptor strands ***m*** and ***f*** that are complementary to MB (MB-binding arms) and to NA analyte (analyte binding arms), respectively. In the absence of target, MB is in closed form and coexists in solution with the two adaptor strands. Upon addition of target analyte, MB is opened up by the two adaptor strands, forming a single DNA crossover structure (also known as DNA four way junction, 4WJ) (Figure 3). In order to stabilize the 4WJ conformation that produces high fluorescence (maximum distance between fluorophore and quencher moieties), triethylene glycol linkers were added between the MB-binding and analyte binding arms (dotted lines in Figure3).

MBs have a wide variety of applications in molecular biology, genetics, and medical diagnostics, most frequently involving rtPCR [7], microarray technology [8, 9], and fluorescence in situ hybridization (FISH) [10]. For example, in living biological systems, MBs enable the visualization of DNA or RNA molecules in vivo, providing information on the location, transportation, and kinetics of these nucleic acids [10, 11]. For this type of applications MBs operable at ambient temperature regime are necessary, but such MB probes are not always easy to design [11]. Also, due to their enhanced specificity, MBs have been extensively used in single nucleotide substitution (SNS) typing [12-14]. The enhanced specificity of MB is due to the formation of the hairpin in dissociation state (DS), structure which is weaker than the MB-matched analyte complex but stronger than the MB-mismatched analyte complex. Thus, the

hairpin interferes with mismatched binding, stabilizing its DS (low ΔG). As a result, MB probes distinguish mismatches in a broader temperature range than unstructured probes do [3, 15]. It is expected that with increasing the degree of conformational constraints in DS, DS to become more stable, and so the temperature discrimination range between complexes of matched and mismatched analytes to be wider. The present work hypothesizes that it would be possible to broaden the discrimination range to its limit by using X sensor, design in which the maximum possible conformationally constraints are introduced to stabilize DS. Indeed, the X sensor has a modular design which allows introduction of one or two stem loops in addition to the stem loop of MB probe. Thus, we explore the conformationally constraint approach to design X sensors for the selective recognition of nucleic acids in a broad temperature range. Further, we explore the potential application of such sensors in real time detection of PCR products.

Figures and tables

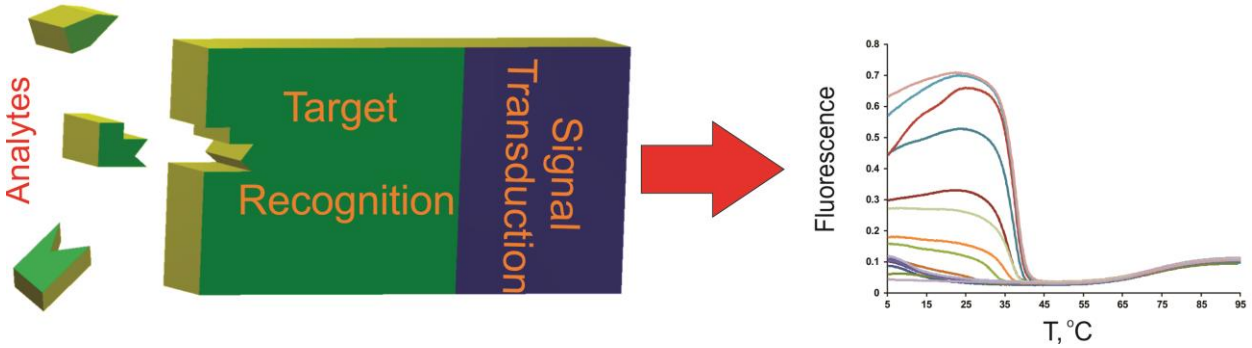

Figure 1. Schematic representation of a fluorescent biosensor

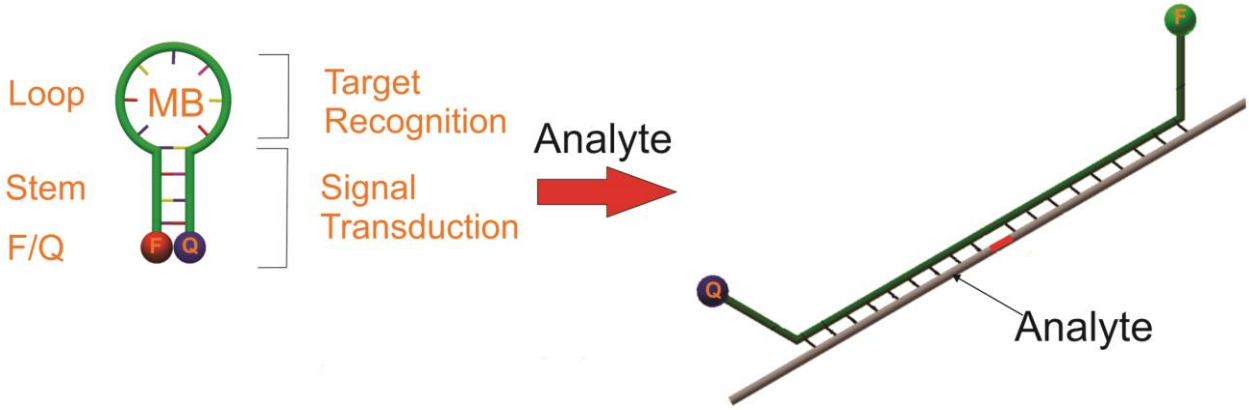

Figure 2. Working mechanism of a molecular beacon

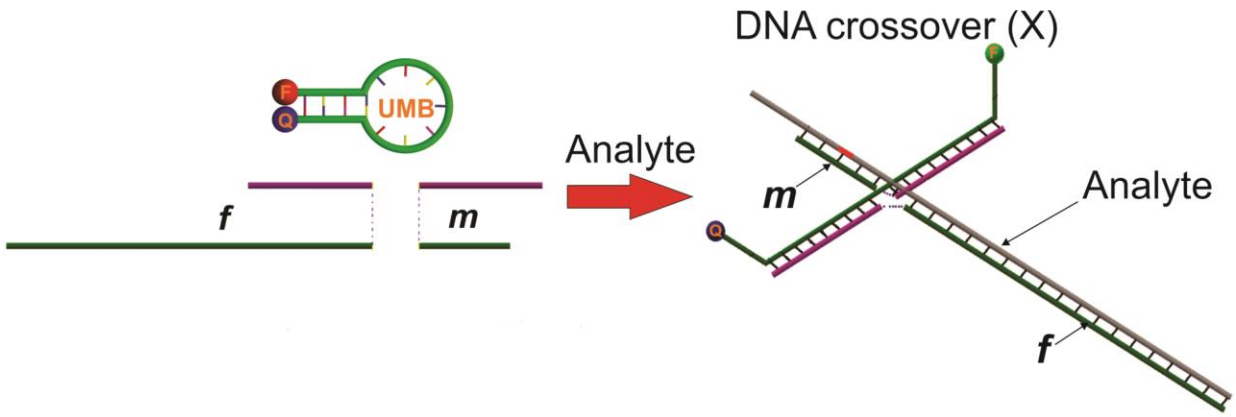

Figure 3. Working mechanism of an X sensor

CHAPTER 2: BROADENING ΔT_M: DIFFERENTIATION OF A SINGLE NUCLEOTIDE SUBSTITUTION IN A WIDE TEMPERATURE RANGE UNDER NON-EQUILIBRIUM HYBRIDIZATION CONDITIONS[†]

Introduction

Analysis of single nucleotide substitution (SNS), which include point mutation and single nucleotide polymorphisms (SNP), has a growing importance in diagnostics of genetic and infectious diseases, genome-wide association studies and forensics among other applications. Hybridization probes have been extensively used in SNS analysis [16-18]. In this approach a 15-25 nucleotide (or longer) nucleic acid probes hybridize to fragments of analyzed DNA or RNA targets containing a SNS site of interest (Figure 4A). The duplex is then destabilized (e.g. by heat) to differentiate fully matched from mismatched hydride. This approach is used by TaqMan probe in real-time quantitative PCR (qPCR) [19] and Affymetrix microarrays for SNP genotyping [9, 20] among other techniques [17, 21, 22]. However, these probes differentiate targets only within a relatively narrow temperature interval of 0.1-10°C, in which the probes form stable complexes with matched, but not with mismatched targets [21, 23] . These temperature intervals are normally above the ambient temperatures, which require instrumentation for heating and temperature control. Therefore, sophisticated and expensive instrumentation is required for maintaining precise temperature for accurate SNS

[†] Part of the work in this chapter is prepared for publication: Stancescu M, Balaeff A, Hooyberghs J, Kolpashchikov DM (2015). Broadening ΔT_m: differentiation of a single nucleotide substitution in a wide temperature range under non-equilibrium hybridization conditions.

analysis. An example of such instrumentation is modern qPCR termocyclers equipped with high-resolution melting temperature capabilities, which increase both the cost of PCR instrument and the assay time. Microarray-based SNS analysis requires precise temperature control, multiple interrogation of the same analyte by a series of probes and sophisticated data analysis, which makes it less competitive in SNS typing when compared with the new generation sequencing techniques [24]. In addition, the low accuracy in SNS differentiation at ambient temperatures hinders RNA analysis in living cells and molecular diagnostics in instrument-free formats [17, 22]. Indeed, broadening the operational temperature range for hybridization probes has been a subject of intensive investigation [23, 25-29]. In this study we demonstrate that it is possible to significantly broaden ΔT_m of a hybridization probe by implementing a non-conventional multicomponent design which enables operation under non-equilibrium conditions.

To broaden the ΔT_m of hybridization probes, '*stringency clamping*' approach has been introduced previously [30]. This approach uses '*conformationally constrained*' probes that form stable structures in dissociated states [3, 31]. One representative of such probes is the 'molecular beacon' (MB) probe, a fluorophore- and quencher-conjugated DNA hairpin (Figure 4B) [1, 32]. When bound to a complementary DNA or RNA, MB probe switches its conformation to a fully elongated, and separates the fluorophore from the quencher. It was demonstrated that ΔT_m for the MB probe is broader than that of a linear probe, and the melting temperatures of MB-target hybrids are shifted towards lower values in comparison to that of linear probes [3, 15, 33]. This is due to the formation of a competing hairpin structure that favors the dissociation of

MB from the complex with target analyte. As a result, the equilibrium is shifted towards dissociated state especially if a mismatch destabilizes the MB-analyte complex. It was hypothesized that selectivity of hybridization probes '*can be modulated by altering the degree of constraint placed on their conformation*' [33]. In other words, the more thermodynamically stable the dissociated state, the greater the degree of constraint - the broader the ΔT_m. Variations of '*conformationally constrained*' probes with a greater degree of conformational constraint include two-stem dumbbell MB probe [34] and triple-stem DNA probes [13]. However, these designs slow down the hybridization kinetics [23,24] and make such probes incapable of analyzing DNA and RNA targets folded in secondary structures [14, 35].

Here we originally aimed at pushing the idea of broadening ΔT_m by increasing the probe constraint (stabilization of DS) to its limit by using an MB-based multicomponent probe strongly stabilized in its dissociated form. We unexpectedly found that the broad differentiation range observed in our experiments is, in part, the consequence of different hybridization rates of the probe to matched and mismatched analytes.

Materials and Methods

Reagents

DNAse/protease-free water was purchased from Fisher Scientific Inc. (Pittsburg, PA) and used for all buffers and for the stock solutions of oligonucleotides. $MgCl_2$ 1 M solution was purchased from Teknova (Hollister, CA), while 1 M Trizma HCl (pH 7.4)

and TWEEN® 20 from Sigma-Aldrich (St. Louis, MO). UMB1 was custom-made by TriLink Biotechnologies, Inc. (San Diego, CA). All other oligonucleotides including MB1 (sequences listed in Table X) were obtained from Integrated DNA Technologies, Inc. (Coraville, IA). The Optical 96-Well plates (EnduraPlate™), optical adhesive film (MicroAmp®) and ROX reference dye were purchased from Life Technologies (Grand Island, NY).

Fluorescence Assay

In order to optimize the sensors assays' conditions, preliminary fluorescence experiments were performed on a Perkin-Elmer (San Jose, CA) LS-55 Luminescence Spectrometer with a Hamamatsu xenon lamp (excitation at 485 nm, emission 517 nm). A quartz cuvette with volume capacity of 100 µl was used for these measurements. To determine optimal concentration of Mg^{2+} ions in the assay' buffer, fluorescence experiments were carried out in buffers containing 50 mM Tris-HCl, pH 7.4 and 6, 8, 10, 50, 100 or 500 mM $MgCl_2$, respectively. The experimental concentration of the molecular beacon was 50 nM, and that of the target was 100 nM, while the adaptor strand concentrations were 120 nM (m7) and 200 nM (f1), respectively (Figure 8 A). To determine the limit of detection (LOD) of the sensor, the concentrations of the analytes were varied from 1 to 750 nM. In all experiments the samples were incubated for 20 minutes at room temperature (22°C). Each set of experiments were repeated three times, and data is shown as the mean with error bars representing one standard deviation from the mean. Native gel electrophoresis of X sensor in complex with

matched or mismatched analytes was also performed to confirm the formation of complexes.

Temperature-dependent fluorescence measurements were carried out using a QS6 real QuantStudio™ 6 Flex System from Life Technologies (Grand Island, NY). The assays were done in a buffer containing 50 mM Tris-HCl (pH = 7.4), 100 mM $MgCl_2$ and 0.1% (v/v) TWEEN® 20. Prior to mixing, the stock solutions of oligonucleotides and MB probes were thawed and let to equilibrate to room temperature for at least 20 min. A master mix solution containing 50 nM of MB1 or L1 probe and 50 nM of ROX dye was prepared. ROX is a passive reference dye, whose fluorescence does not change with temperature, and which helps correcting for changes in signal within a run due to non–PCR-related artifacts. To this solution 100 nM of target DNA was added for all probes, and 120 nM of adaptor strand m and 200 nM of adaptor strand f for X probes only. For each set of samples prepared we had three controls: (1) master mix, (2) master mix and the adaptor strands and (3) ROX dye only. The samples were loaded into a 96-well plate (30 µl per well), which was sealed with an optical adhesive cover, vortexed and then spun at 660 rcf for 20 sec. Care was taken such that to avoid the formation of air bubbles in the wells. The solutions were fast heated (1.6°C/s) to 95°C, melted at 95°C for 1 min, and fast cooled (1.6°C/sec) to 5°C. After 30 min of equilibration at 5°C, the temperature was raised back to 95°C (0.05°C/sec), while fluorescence intensity was recorded continuously about every 0.2°C. Additional annealing followed by melting experiments were carried (Cooling-Heating cycles) as follow: melting at 95°C for 1 min, followed by cooling to 5°C in 1°C increments with sample equilibration at each degree

for different duration of times - 19 sec, 60 sec, 600 sec or 1800 sec, respectively; heating from 5°C to 76°C was done similarly in 1°C increments with 19 s, 60 sec, 600 sec or 1800 sec equilibration times at each new degree.

Optical filter set x1-m1 recommended by system's manufacturer which supports FAM™ and SYBR® Green dyes were used. The QuantStudio™ 6 Flex System was calibrated for well factors, background, and dye fluorescence. Melting data for each DNA sample were initially processed with the QuantStudio™ Real-Time PCR Software (version 1.1), and further exported into Excel. The values were averaged over at least two wells and then replotted.

Results

Probe Design

In this study, three types of hybridization probes were used: conventional linear probe and MB probe, as well as multicomponent probe introduced by us earlier [4] (Figure 4, upper panels). The multicomponent probe, dubbed here 'X probe', consisted of a universal MB (UMB) probe and the two adaptor strands ***m*** and ***f*** (Figure 4C, upper panel). Both ***m*** and ***f*** contain UMB- and analyte- binding arms and form a DNA crossover (X) structure in the presence of the complementary analyte [4, 6]. UMB did not form contacts with the analyte and, therefore, could be used universally for the analysis of any target [5]. The X structure contained UMB probe in its elongated highly fluorescent conformation. The higher degree of thermodynamic stabilization of the dissociated state (conformational constraint) in comparison with linear probe is achieved

due to (i) MB probe hairpin structure; (ii) the residual hybrid between the analyte and strand ***f*** (Figure 4 C, left); (iii) the entropy factor due to complex dissociation into three fragments (strand ***m***, UMB and strand ***f***-analyte complex) rather than two as in the case of linear and MB probes. The length of the analyte-binding arm of strand m can be fine-tuned to make it extra-sensitive to the presence of a single base mismatch. A series of four X probes for recognition of the same SNS site were designed. All X probes used the same UMB probe, UMB1, as a reporter, and strand *f* (X1-f), but differed by the lengths of the analyte-binding arms of strands *m*, which varied from 6 to 9 nucleotides (X1_m 6-9, Table 1).

The nucleotide sequences of the DNA analytes, the linear probe (L1) and the MB probe (MB1) were previously used by Tsourkas et al. [15, 33]. The idea was to reproduce the results of other research group and compare the performance of X probe with the well-recognized prior findings. The analyte sequence corresponded to a fragment of the udg gene encoding human uracil DNA glycosylase (UDG), named here udg_A and udg_G (Table 1). Tsourkas et al. used dual labeled linear probe with a fluorophore on the 5’ and a quencher on the 3’ ends. In general, however, this design does not provide high turn-on ratio upon hybridization to a target [36, 37]. In our design, L1 was labeled only with a fluorophore, while the quencher was conjugated to the 3’ end of the analyte (Figure 4A). This design deemed to be more general in providing high signal turn-on ratio. In addition, it attracted significant attention both in the past [38-40], and recently [41-47]. Unlike MB and X probes, which decreased fluorescence when dissociated from the target, L1 probe increased fluorescence in DS.

SNS differentiation by the three types of hybridization probes

Figure 4 (lower panels) shows melting profiles of the three hybridization probes with both matched and mismatched analytes. Figure 4A (lower panel) shows the inverse fluorescent values (1/F) over temperature for L1 probe in order to simplify data comparison with that for MB1 and X1 probes shown in panels B and C. The T_m values for the L1 hybrids with matched and mismatched targets (Table 2) were found to be 3-4°C lower than that reported by Tsourkas et al., and close to the predicted by nearest-neighbor model (NN) for DNA hybridization (The DINAMelt Web Server) [48]. The possible source of difference of the T_m values is due to the different probe design and buffer conditions. However, the ΔT_m, the parameter that characterizes SNS differentiation efficiency, was 9.6°C, which is identical to the value reported previously [33]. As expected, MB1 differentiated mismatched target in a broader ΔT_m than L1 probe with T_m shifted by 2-3°C toward lower values (Table 2).This results correlates well with the previous findings [33].

Figure 4C shows the melting curves of X1_m7 with a 7-nt analyte-binding arm of strand m. The melting temperatures for the X probe were shifted toward low values by > 30°C, while ΔT_m was broadened by 6-7°C (Table 2). Thus, the effects reported for conformationally constrained probes earlier [3, 15, 33] were even more pronounced for the X probe. To assess the efficiency of SNS differentiation, we plotted F_m/F_{mm} as a function of temperature for the 3 probes, where F_m and F_{mm} is the fluorescence in the presence of matched and mismatched analytes, respectively (Figure 5A). The differentiation range for the L1 and MB1 probes were close to each other with the

expected shift to lower temperatures and broadening for the MB probe. The profile for X probe has significantly more pronounced shift to low temperatures and broadening.

Differences in ΔT_m are commonly used to asses discrimination abilities of hybridization probes [15, 33]. However, the data presented in Figure 5A suggest that X1 probe efficiently differentiate analytes even at the T_m for mismatched analyte (19°C) with differentiation parameter $F_m/F_{mm} > 4$. To point out this practically significant feature of X1 probe, we introduced another quantitative parameter, $\Delta T_{1.5}$ (Table 2). Based on our experience, fluorescent output signal is measured with standard deviation (σ) of ~15% with 3σ (confidence interval 99%) corresponding to ~45-50%. In other words, statistically distinguishable signals should differ by ~ 50%. Figure 5 shows a threshold at 1.5 F_m/F_{mm}, which corresponds to 50% higher signal in the presence of matched than in the presence of mismatched analyte. Based on this empiric criterion, MB1 differentiated analytes in the temperature interval of 17.1°C, which is 2.5°C broader than for L1 probe. The X1 probe allowed SNS differentiation in the widest temperature range of all the three probes ~ 35°C (Table 2). X probes with other strands ***m*** also differentiated the mismatched target at all operational temperatures. However, fluorescence above the background was observed for sensor with X1_m8 and X1_m9 (Figure 6). The T_m values for different X sensors were shifted as expected to the higher values for X1_m8 and X1_m9 and to the lower values for X1_m6 (Table 2, Figures 6). A poorer performance was also observed for X1_m8 and X1_m9 than for X1_m6 and X1_m7 at low temperature (Figure 7).

Non-equilibrium condition contributes to the broadening of differentiation temperature range

Importantly, fluorescence of the X probe in the presence of mismatched analyte (dotted line) was at the background level at leading SNP differentiation even at low temperatures. However, theoretical predications in the assumption of thermodynamic equilibrium suggest negligible differentiation of matched from mismatched analytes at temperatures <15 ^{o}C (Figure 5B). To explain this discrepancy of the theory and the experiment, we investigated the change in fluorescence of the hybridized samples allowing different times for equilibration at each temperature. Both linear and MB probe achieved near equilibrium state during the shortest time of 19 sec allowed for equilibration. Notable the melting profiles measured by cooling from 75 ^{o}C to 5 ^{o}C the hybridization samples followed by heating from 5 ^{o}C to 75 ^{o}C were symmetric (Figure 8A and B) further proving the near equilibrium conditions for L1 and MB1 probe-analyte complexes. In contrast, X1 sensor demonstrated significant difference in fluoresce depending on the time given for equilibration as well as strong hysteresis (Figure 8C, D). Analysis of the dependence the fluorescence on the equilibration time reveals significant stabilization of probe-analyte complexes for L1 and MB1 probe after 19-60 sec. However, fluorescence continues to grow for X1_m7 probe after 60 sec equilibration, and even further after 600s but only for mismatched complex (insert in Figure 8D). In addition, the slop of the curve for mismatched complex in the range 60-600 sec is higher than that for matched analyte suggesting slow elaboration of the first. This data indicate that X sensor operated under non-equilibrium conditions: the equilibration with mismatched is slower than with matched analyte, which results to the

high discrimination factor observed for X sensor at low temperatures (Figures 4A, 8D). Figure 9 shows the analyte-probe complexes formed by the three types of probes used in this study. Figures 10 shows the preliminary fluorescence assays carried out in order to determine the optimal Mg^{2+} concentration in the buffer (panels A, C) and the limit of detection (LOD) of the sensor (panels B, D). Based on these results we decided on the optimal Mg^{2+} concentration (100 mM) and the analyte concentration (100 nM) for further experiments. Figure 11 presents the native polyacrylamide gel electrophoresis (nPAGE) analysis of samples containing the X sensor in the presence or absence of the target. The band pointed by the yellow arrow represents the complex formed with the WT target (Figure 11, top panel) before dye staining. The band indicated by the blue arrow represent the residual duplex formed between the f-analyte binding arm and either WT or SNP analytes after SYBR gold staining (Figure 11, bottom panel). Thus, this residual duplex is present in DS of both complexes with WT and SNP analytes.

Discussion

Broadening the temperature intervals for selective recognition of SNS is an important practical task since it can simplify and make more accurate tests for single nucleotide polymorphisms and genetic mutations [21, 25-29]. Shifting the operation temperatures of hybridization probes to ambient temperatures (~20-40°C), on the other hand, opens a possibility to detect SNS at room temperature and in living cells.

Earlier, Tsoukas et al. demonstrated that T_m for one type of conformationally constrained probes, MB probes, is shifted towards lower values [15, 33]. Moreover, MB

probes differentiated SNS in a broader temperature range than linear probe. We aimed at exploring the idea of 'conformational constrain' to its extreme by designing X probe in which the dissociated state (Figure 4C, upper panel) is highly stabilized by both enthalpy and entropy factors. The base pairs in UMB stem and in strand ***f***-analyte complex contribute to the enthalpy–driven stabilization of X probe's DS in comparison with a linear probe. The dissociation of the X complex into 3 parts rather than two (as in the case of linear and MB probes) contributes to ΔS gain for DS. Such design was expected to enable unprecedented broadening of ΔT_m.

Indeed, analysis of SNS in DNA fragments revealed superior performance of X sensor in comparison with linear and MB probes. Specifically, the ΔT_m for X sensor was 6.8 and 5.2°C broader than that of linear and MB probes, respectively. Moreover, based on the practical criteria, X sensor is capable of differentiating SNS in the temperature range 20.2 and 17.7°C broader than linear and MB probes, respectively (compare $\Delta T_{1.5}$ columns of Table 2). Importantly, unlike linear and MB probe, X sensor differentiated SNS at ambient temperatures of ~20-40°C.

Interestingly, the left wing of F_m/F_{mm} over temperature profile for X sensor (Figure 4) deviate from the parabolic dependence found for linear and MB probes. This can be explained by non-equilibrium conditions at lower temperatures. In order to prove this hypothesis we studied the dependence of fluorescent response of the probe-analyte complexes allowing different times for equilibration of the hybridization samples. It was found that unlike linear and MB probes, X sensor did not reach equilibrium under experimental conditions. Importantly, the hybridization mixture with mismatched analyte

reaches equilibrium slower than that with matched analyte. This observation suggests the new strategy for the design of highly selective hybridization probe that operate under non-equilibrium conditions. It seems that multicomponent probe design is one of the possible approaches to implement this strategy.

Besides high selectivity, the advantages of X sensor include the following. (i) Modular design: – each component (UMB, ***f*** and ***m*** stands) can be individually optimized to serve their functions. (ii) Universality of some components: both UMB and UMB-binding arms of strands ***f*** and ***m*** can be designed ones for particular conditions and then used uniformly for each new analyte. (iii) The sensor can be adopted to the analysis of RNA with stable secondary structures [6].

Interestingly, all four X probes with different lengths of analyte binding arms distinguished SNS within the full range of temperatures, at which the X probe was bound to the matched analyte. However, unlike X sensor with X1_m6 and X1_m7, the X1_m8 and X1_m9 produced noticeable signal above the background in the presence of mismatched analyte (Figure 5). This observation suggests that the selectivity of X sensor can be controlled by the length of analyte binding arm of strand *m*.

Furthermore, the X complex studied here was unstable at the temperatures above 40°C due to the short UMB-binding arms of strands ***m*** and ***f*** (9 bases in each case). Following studies with longer UMB and UMB binding arms are needed to determine how far the differentiation range can be shifted towards higher temperatures. Is it possible to design a probe that differentiates SNS in all practically significant temperature from 5 to 90°C?

However, even in the present format the selectivity of X sensor is clearly pronounced for low temperatures including ambient, which is a traditional challenge for probes longer than 15 nucleotides [21, 27-29] . Broadening ΔT_m observed in this study may appear to be the general property of binary and multicomponent probes of various designs [17]. This property is practically useful for the design of SNS-specific sensors for qPCR, microarrays, as well as RNA analysis in living cells and for ambient temperature point-of-care diagnostics, which promise to diversify the range of formats available for diagnostics of genetic and infectious diseases. This study, therefore, provides a potentially general basis for construction of hybridization-based probes for SNS differentiation under given experimental conditions. Both analytes, but particularly the WT one (udg_G), fold into stable secondary structures (Figure 9) in the assays' conditions (50 mM monovalent cation, 100 Mm divalent cation). This fact might have also contributed to the stabilization of DS, and the improvement of probe's performance. Thus, it was important to assess the probe's performance in hybridization reactions with analytes containing minimum secondary structures.

Figures and tables

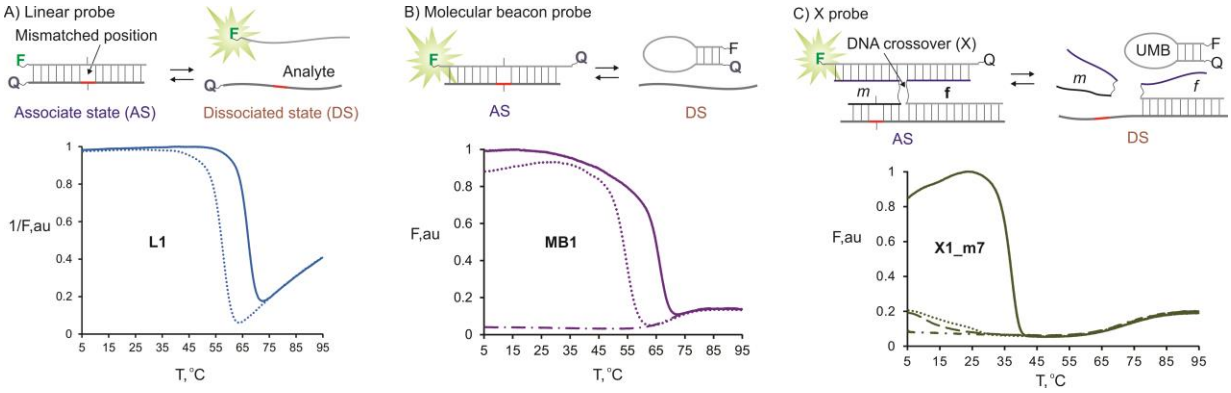

Figure 4. Different types of hybridization probes: design and fluorescent melting profiles.

A) Linear probe. Upper panel: unfolded DNA probe hybridizes to a nucleic acid analyte. In this study the analyte was labeled by a quencher dye (Q), while the probe was conjugated with a fluorophore (F) to enable fluorescent detection of complex formation. Bottom panel: Inverted fluorescence (1/F) of the linear probe L1 in the presence of matched udg_G_Q1 (solid line) and mismatched (dotted line) udg_A_Q1 analytes at different temperatures.

B) MB probe. Upper panel: MB probe upon hybridization to a complementary target. Lower panel: Fluorescent response of MB1 in the presence of fully matched udg_G (solid line) or mismatched udg_G (dotted line) at different temperatures. Dash-dotted line is melting of MB1 alone.

C) X1 probe. Upper panel: Strands *m* and *f* bind analyte and a universal MB probe (UMB) to form a fluorescent crossover (X) complex. UMB-binding arms of strands *f* and *m* are in blue. Low panel: Melting temperature for X1 probe (UMB1, X1_f, X1_m7) in the presence of fully complementary udg_G (solid line) or mismatched udg_G (dotted line). Dash-dotted line corresponds to the melting of UMB1 alone, while dashed line represents the melting of X1 (no target).

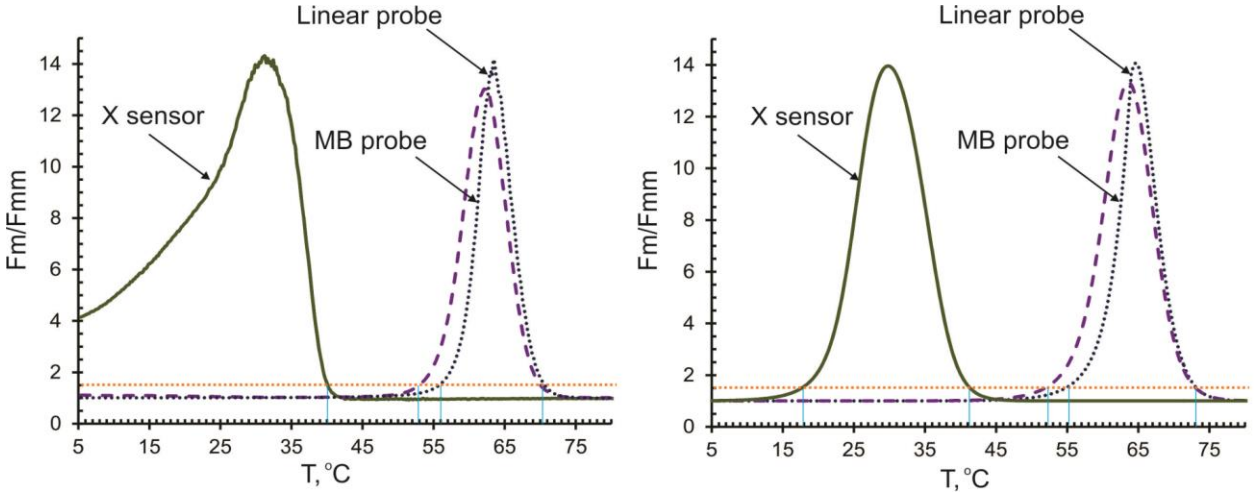

Figure 5. Differentiation range for the three types of hybridization probes.

A) The ratio of fluorescence produced by each probe in the presence of fully matched analyte (F_m) to that of mismatched analyte (F_{mm}) are plotted against temperature for linear probe (blue dotted line), MB probe (purple dashed line) and X sensor (green solid line). The threshold F_m/F_{mm} ~ 1.5 is indicated by the orange dotted line. The intercepts of the graphs with the 1.5 threshold are indicated by vertical red lines; the values that correspond to the intercept are given in Table 2.

B) Theoretical prediction of the profiles shown in panel B in the assumption of thermodynamic equilibrium: the conformational constraints are modeled as an enthalpy correction on the free energy of the nearest neighbor model.

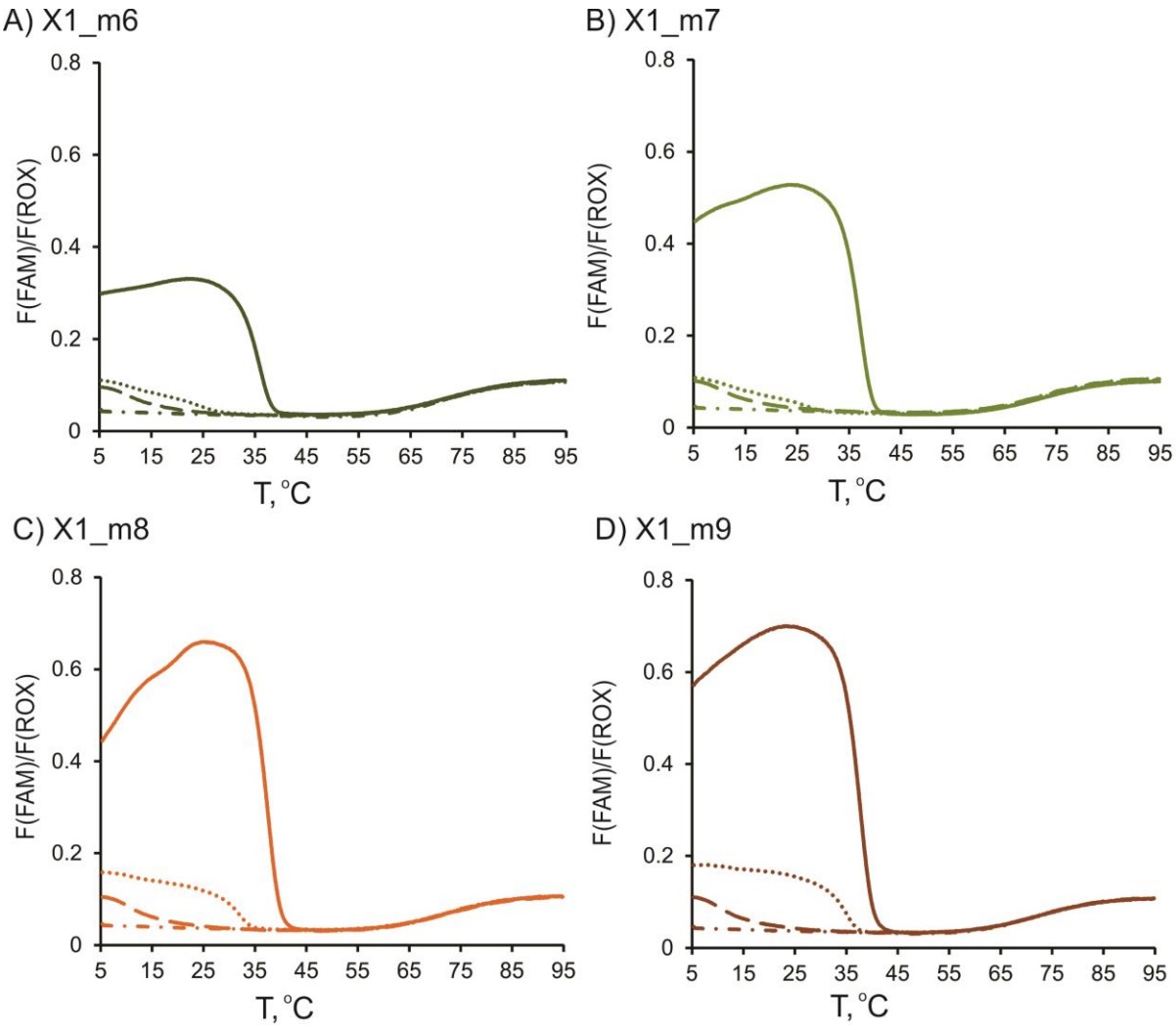

Figure 6. Fluorescent response of X1 probes with various lengths *m* strands to the presence of DNA analytes

Solid lines represent melting of the matched analyte complex, while dotted lines of the mismatched one. Dashed lines represent the background, while dot-dashed lines represent UMB1 alone. All reaction mixtures contained 50 mM Tris-HCl (pH = 7.4), 100 mM $MgCl_2$, 50 nM UMB1; 200 nM X1_f and 120 nM different stand *m* as follows A) X1_m6; B) X1_m7; C) X1_m8; D) X1_m9.

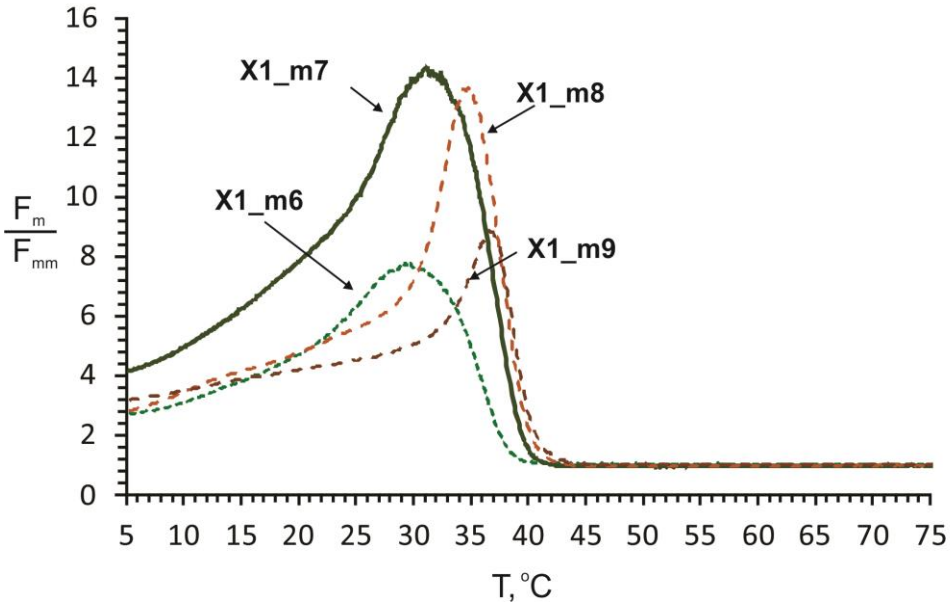

Figure 7. Differentiation range for all X1_m sensors.

Ratio of fluorescent responses of X sensors to the presence of fully matched (F_m) to mismatched (F_{mm}) analytes at different temperatures.

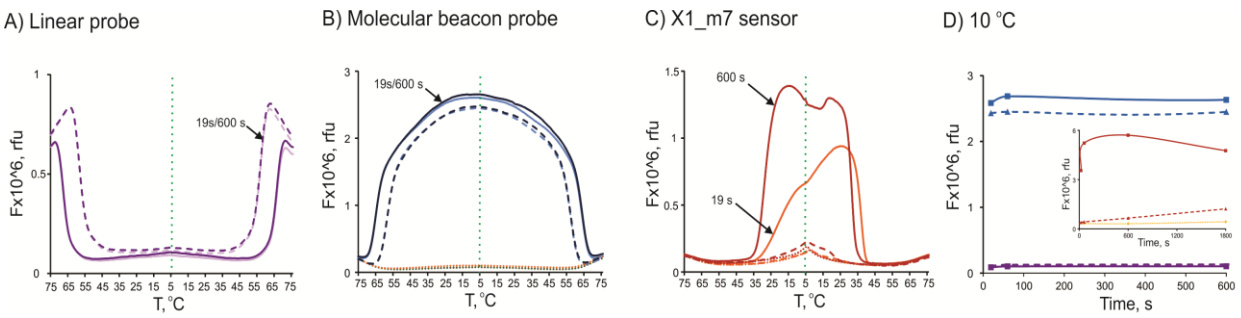

Figure 8. Stabilization of fluorescent signal for the probe-analyte complexes depending on equilibration time given at each temperature.

A) L1 probe equilibrated for 19 (light purple) and 600 (purple) sec, B) MB1 probe equilibrated for 19 (light blue) and 600 (blue) sec C) X1_M7 probe equilibrated for 19 (orange) and 600 (red) sec. D) Dependence of fluorescence on equilibration time at 10^{o}C data for 19, 60 and 600, 1800 sec (inserted figure) allowed for equilibration are shown. Solid and dashed lines represent data for matched and mismatched complexes, respectively.

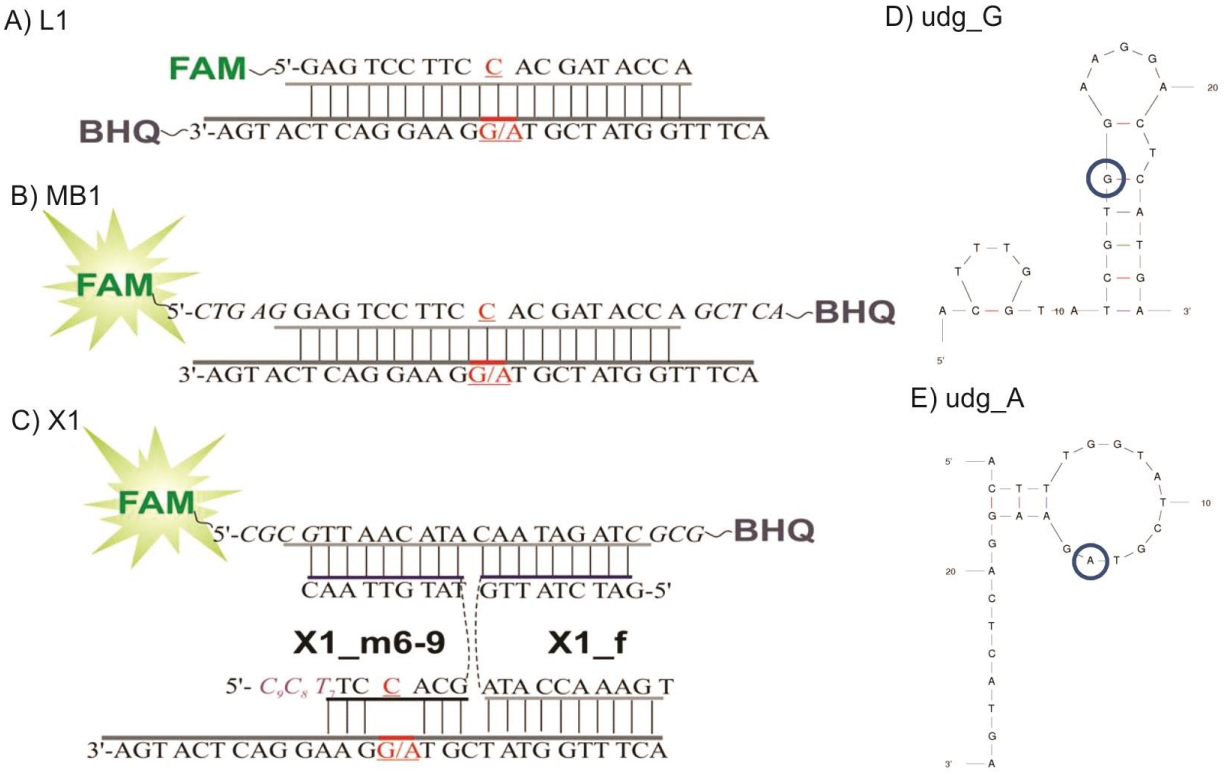

Figure 9. Structures of analyte-probe complexes and analytes used in this study.

A) L1; B) MB1; C) X1. SNS positions are red underline. TEG linkers are shown as dashed lines in panel C. Purple C7, C8 and T7 indicate nucleotides that are absent in X1_m6 adaptor strand in panel C. Folding of DNA analytes at 10°C under experimental conditions: udg_G (D) and udg_A (E). The position of point mutations in the sequence is blue circled.

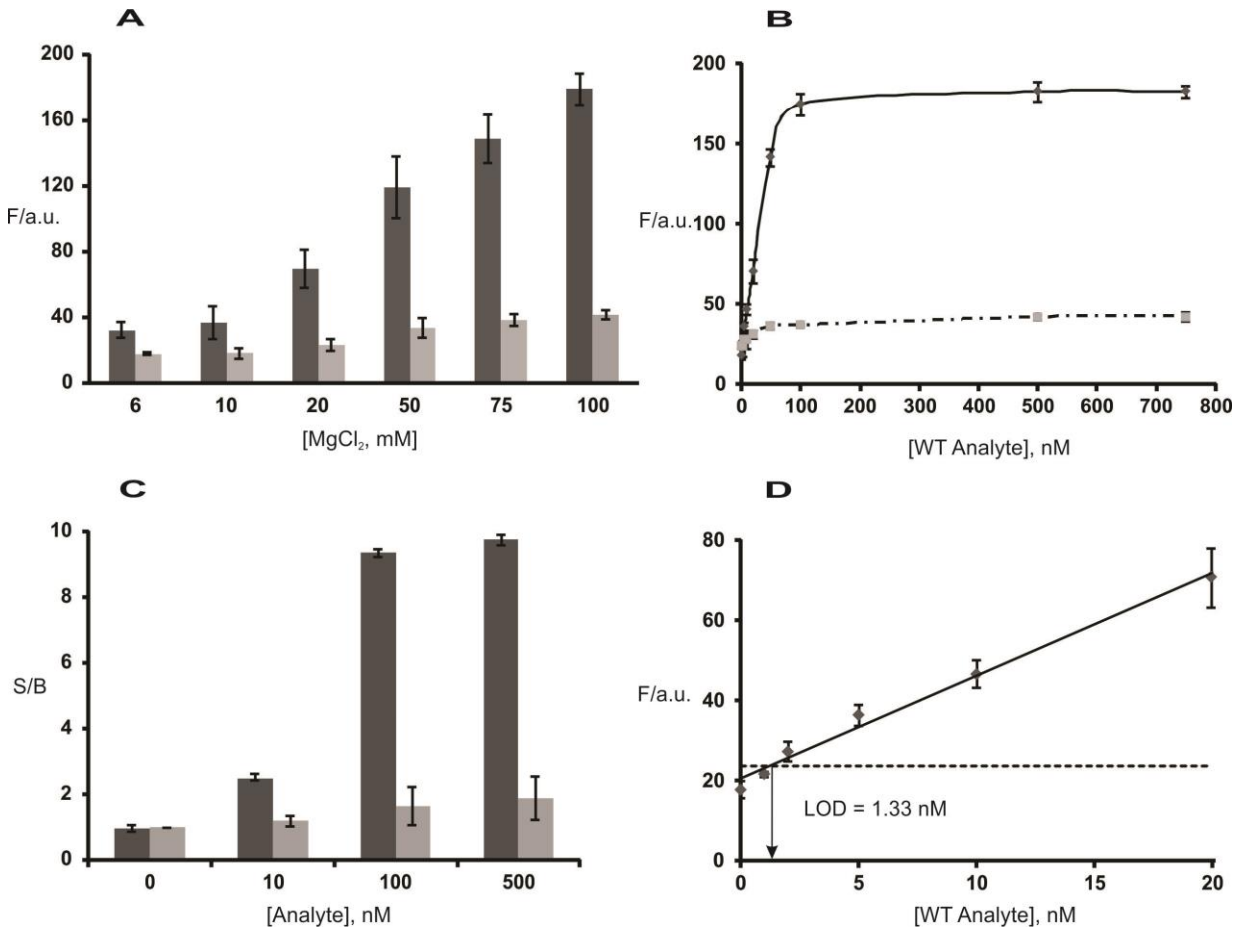

Figure 10. Optimization of fluorescence assay at RT.

A) Fluorescent response of X2_f_m7 sensor in complex with WT (black columns) or SNP (gray columns) in a buffer containing different concentrations of $MgCl_2$

B) Fluorescent response of X2_f_m7 sensor in the presence of various concentrations of WT (solid line) and SNP (dash-dot line).

C) Signal-to-noise ratios for X2_f_m7 sensor representing the mean of three independent experiments with error bars indicating one standard deviation.

D) X2_f_m7 sensor's performance. The limit of detection (LOD) was calculated as the analyte concentration that triggered a fluorescent signal equal to the average fluorescence of the background from three independent measurements plus three standard deviations of the average background fluorescence. The grey dashed lines represent the respective threshold and the arrow points the LOD.

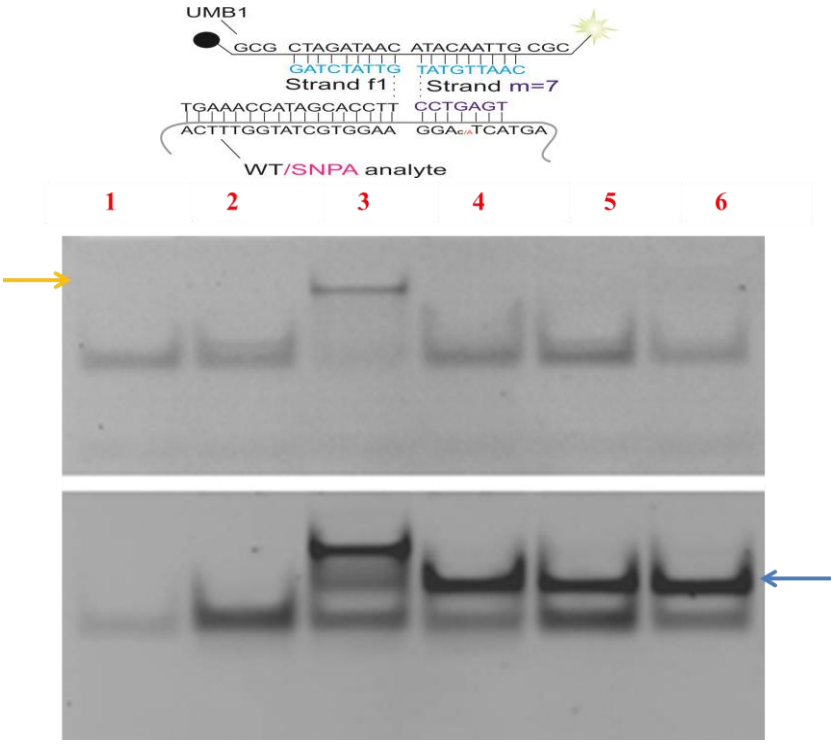

Figure 11. Native polyacrylamide gel electrophoresis (nPAGE) of tetrapartite complex formation.

100 nM UMB1 fluorophore mimic, UMB1' (UMB1 but without quencher) was incubated alone (lane 1) or with 400 nM of m7 and ***f*** staples and 100 nM of WT or SNP analytes (lanes 2-6) as follow: Lane 2: UMB1', m7 and ***f***; Lane 3: UMB1', m7, ***f*** and WT; Lane 4: UMB1', m7, ***f***, SNP; Lane 5: UMB1', ***f*** and WT; Lane 6: UMB1', ***f*** and SNP. Each well was loaded with a total of 120 ul sample out of which 20 ul was the nPAGE-loading buffer (50% glycerol, 100 mM $MgCl_2$, 50 mM Tris-HCl pH 7.4, 0.05 % bromophenol blue, 0.05 % xylene cyanol). The 1.8 mm thick gel was run for 75 min at 100 V and room temperature. The figure shows photos of the same gel taken before staining (top) and after SYBR Gold staining (bottom). The complex is indicated by the yellow arrow.

Table 1. Sequences of oligonucleotides used in the study of three different DNA hybridization probes.

Name	Sequence	Purification
udg_A_Q1	5'-ACT TTG GTA TCG TAG AAG GAC TCA TGA/BHQ1/	HPLC
udg_G_Q1	5'-ACT TTG GTA TCG TGG AAG GAC TCA TGA /BHQ1/	HPLC
udg_A	5'-ACT TTG GTA TCG TAG AAG GAC TCA TGA	SD
udg_G	5'-ACT TTG GTA TCG TGG AAG GAC TCA TGA	SD
L1	/FAM/-5'- GAGTCCTTCCACGATACCA	HPLC
MB1	/FAM-5'-*CTG AGC* GAG TCC TTC CAC GAT ACC A *GCT CA*/BHQ1/	HPLC
UMB1	/FAM/-5'-*CGC G*TT AAC ATA CAA TAG AT*C GCG*/BHQ1/	HPLC
X1_f	5'-GAT CTA TTG/teg/ATA CCA AAG T	SD
X1_m6	5'-TCC ACG/*teg*/TAT GTT AAC	SD
X1_m7	5'-TTC CAC G /*teg*/TAT GTT AAC	SD
X1_m8	5'-CTT CCA CG/*teg*/TAT GTT AAC	SD
X1_m9	5'-CCT TCC ACG/*teg*/TAT GTT AAC	SD
X2_f	5'-GAT CTA TTG/*teg*TTCC ACG ATA CCA AAG T	SD
X2_m7	5'-TGA GTC C/*teg*/TAT GTT AAC	SD

Table 2. Temperature characteristics for probe-analyte complexes.

Probes	**L1** (liner)			**MB1** (molecular beacon)			**X1_m7** (X)		
Parameters	T_m/T_m(NN)	ΔT_m	$\Delta T_{1.5}$	T_m	ΔT_m	$\Delta T_{1.5}$	T_m	ΔT_m	$\Delta T_{1.5}$
Matched target	67.1/65.4	9.6	14.8 (55.8-70.6)	65.4	11.2	17.1 (52.9-70.0)	35.6	16.4	35.0 (5.0-40.0)

T_m,°C, melting temperatures determined for the data presented in Figure 2; T_m (NN), melting temperature predicted by the nearest-neighbor model (NN); ΔT_m, the difference of melting temperatures of fully matched and mismatched hybrids; $\Delta T_{1.5}$,°C the temperature interval in which fully matched analyte produces signal 1.5 times greater than a mismatched analyte.

CHAPTER 3: OPTIMIZATION OF MB-BASED MULTICOMPONENT PROBES FOR ANALYSIS OF NUCLEIC ACIDS WITH NEARLY LINEAR STRUCTURE

Introduction

In this chapter the idea of broadening the matched-mismatched temperature discrimination range is extended to an X sensor capable of detecting a target bearing a negligible secondary structure with higher specificity than its MB or linear probes counterparts. The quest was to design and further optimize the X sensor, such that to obtain robust sequence discrimination in a wide temperature range without modifying the reaction conditions (i.e. buffer). One approach to consider is to introduce additional conformationally constrained structures in the system (beside the beacon's hairpin).

Kramer and co-workers have shown that structured probes exhibit greater sensitivity to mismatches than unstructured probes do [3]. This is because the structured probes stabilize the probe-analyte's dissociated state (DS), reducing its free energy, ΔG, and thus by bringing ΔG of DS closer to ΔG of probe-analyte's associated state (AS), it was possible to better discriminate mismatch from match analytes [1]. It is expected that the more "conformationally constrained" the structures the broader the discrimination SNS range. However, there are kinetic and thermodynamic penalties imposed by the secondary structures present either in the probe or in the target or in both that need to be considered– complex formation is slow, and for the latest resulting hybrids have lower melting temperatures and free energies than for the first [49]. In comparison, unconstrained probes hybridize to their targets in seconds, but with lower

specificity. For practical consideration the design of MB probes applicable to our X probes should be chosen depending on the application. For example, if high sensitivity to mismatch is required like in SNP detection, the greater “conformational constrained” probes should be used, while in applications where a fast sensor response is more important like in real-time study of RNA expression *in vitro,* less “conformationally constrained” probe should be employed [15].

On the same line, the loop region of a hairpin conventionally designed to be complementary to the targets, are better exposed for hybridization as compared to linear probes [8]. Further, it has been shown that the lengths of loops and stems of MB probes have a significant impact on probe’s specificity and hybridization kinetics: a long loop decreases specificity and increases kinetic rate constants, while a long stem has an improved ability to discriminate mismatches in a broad temperature range, but with the same kinetic penalty [15, 49]. A compromise of the two approaches has been shown to be a structured probe with probe region shared between the stem and the loop, the so called “shared-stem” MB probes [33]. These probes formed more stable duplexes with fully complementary targets, but their specificity to discriminate mismatches was poorer than for conventional MB probes.

In the first chapter we showed that an X probe was capable of discrimination SNP in a broad temperature range in part because of the difference in the hybridization rates of the probe to matched and mismatched analytes. Practically the X probe operated under non-equilibrium conditions. Here we applied an X sensor to analyze DNA that does not form stable secondary structures at least in close to ambient

temperature interval 26-40°C. We found that recognition of such analyte by X sensor takes place under near equilibrium conditions with SNP discrimination approaching that theoretically predicted. We then show that by introducing additional conformational constraints in probe's design we can change its kinetics in hybridization reactions with matched and mismatched analytes, shift its operation to non-equilibrium conditions which resulted in a significant improvement of probe's performance in discriminating SNP. To assess the performance of our probes we compare the melting of hybrids formed with conventional X sensor (no stem and loops present) with the ones of standard MB and linear probe counterparts. Further, we add stem-loop components to one or both analyte binding arms of the X sensor and monitor the melting of complexes resulted with the same nearly free of secondary structure analyte, either fully complimentary or containing one single base pair mismatch.

Materials and Methods

Reagents

DNAse/protease-free water was purchased from Fisher Scientific Inc. (Pittsburg, PA) and used for all buffers, stock and working solutions of oligonucleotides and probes. $MgCl_2$ 1 M solution was purchased from Teknova (Hollister, CA), while 1 M Trizma HCl (pH 7.4) and TWEEN® 20 from Sigma-Aldrich (St. Louis, MO). UMB1 was custom-made by TriLink Biotechnologies, Inc. (San Diego, CA). All other oligonucleotides including MB_inh and LP_inh (sequences listed in Table X) were

obtained from Integrated DNA Technologies, Inc. (Coraville, IA). The Optical 96-Well plates (EnduraPlate™), optical adhesive film (MicroAmp®) and ROX reference dye were purchased from Life Technologies (Grand Island, NY). The concentrations of oligonucleotides in stock solutions were determined from Lambert Beer equation. Absorptions of these solutions at 260 nm and RT were measured with a Perkin-Elmer Lambda 35 UV/Vis spectrometer (San Jose, CA), while the corresponding extinction coefficients were determined by using OligoAnalyzer 3.1 software (Integrated DNA Technologies, Inc.). Working solutions of adequate concentrations were prepared for all oligonucleotides and probes and stored to -20°C until use.

Fluorescence Assay

Temperature-dependent fluorescence measurements were carried out using a real time QuantStudio™ 6 Flex System from Life Technologies (Grand Island, NY). The assays were done in a buffer containing 50 mM Tris-HCl (pH = 7.4), 100 mM $MgCl_2$ and 0.1% (v/v) TWEEN® 20. Prior to mixing, the stock solutions of oligonucleotides and MB probes were thawed and let to equilibrate to room temperature for at least 20 min. A master mix solution containing 50 nM of adequate probe and 50 nM of ROX dye was prepared. In general, to this solution 100 nM of target DNA was added for all probes, and 120 nM of adaptor strand m and 200 nM of adaptor strand f for X probes only. In some experiments, different concentrations of adaptor strands m and f were used, but for each particular case the assay's conditions are mentioned in figure legend. For each set of samples prepared we had three controls: (1) master mix, (2) master mix and the

adaptor strands and (3) ROX dye only. The samples were loaded into a 96-well plate (30 µl per well), which was sealed with an optical adhesive cover, vortexed and then spun at 660 rcf for 20 sec. Care was taken such that to avoid the formation of air bubbles in the wells. In a typical melting curve experiment, the solutions were fast heated (1.6°C/s) to 95°C, melted at 95°C for 1 min, and fast cooled (1.6°C/sec) to 5°C. After 30 min of equilibration at 5°C, the temperature was raised back to 95°C (0.05 °C/sec), while fluorescence intensity was recorded continuously about every 0.2°C. In addition annealing and melting experiments were carried out in order to monitor the sensors' equilibration time at different temperatures. The minimum continuous heating/cooling rate which can be programed with the QS6 RT PCR instrument is 0.02°C/sec. However, slower temperature rates can be achieved by raising/lowering the temperature stepwise, at each new °C holding the temperature for a set time. The thermal treatment used in these experiments included a software controlled sequence consisting of 2 PCR stages flanked at the beginning and at the end by 2 Hold stages. In the first Hold stage the temperature was ramped fast (1.6°C/sec) to 95°C and hold there for 1 min. In the 2 PCR stages that follow, the samples were annealed and then melted in 1°C increments from 75°C to 5°C and back from 5°C to 75°C with different equilibration times: 19 sec, 60 sec or 600 sec, respectively. These times correspond to 0.05, 0.02, 0.002°C/sec rates of temperature change, respectively. In the last Hold stage the temperature was ramp down to 25°C.

Optical filter set x1-m1 recommended by system's manufacturer which supports FAM™ and SYBR® Green dyes were used. The QuantStudio™ 6 Flex System was

calibrated for well factors, background, and dye fluorescence. Melting data for each DNA sample were initially processed with the QuantStudio™ Real-Time PCR Software (version 1.1), and further exported into Excel. The experiments were done in triplicates.

Results and Discussion

Probe Design

In this study, three types of hybridization probes were used (Figure 12 upper panels): conventional linear probe (A), MB probe (B), as well as X probe described earlier (Figure 2) [4] (C). As an analyte, we chose a DNA fragment of the operon of a gene responsible for *mycobacteria tuberculosis* resistance to antibiotic isoniazid (**Inh**). The structure of Inh analyte contained minimal secondary structures with SNS site located in an opened region under experimental condition (Figure 19A). The sensor called here 'X_inh sensor' consists of an MB probe and the two adaptor strands ***m*** and ***f*** (panel C, top). Both ***m*** and ***f*** contain analyte binding arms and the MB-binding arms and forms a DNA crossover (X) structure in the presence of complementary DNA or RNA analyte [30,31]. The X structure contains MB probe in its elongated highly fluorescent conformation. The high degree of thermodynamic stabilization of dissociated state (conformational constraint) is achieved due to (i) MB probe hairpin structure plus (ii) the residual hybrid between the analyte and strand ***f***. In this design we can finely tune the length of analyte binding arm of m strand to make it extra-sensitive to the SNS position, so a single base misspairing dramatically destabilizes the complex. Alternatively, one or both analyte binding arms can be designed to contain a stem-loop structure, and thus

additional conformational constraint can be added to the probe. As an analyte, we chose a DNA fragment of the operon of a gene responsible for *mycobacteria tuberculosis* resistance to antibiotic isoniazid (**Inh**). The structure of Inh analyte contained minimal secondary structures with SNS site located in an opened region under experimental condition (Figure 19A). Our initial aim was to compare the performance of the 3 types of hybridization probes: linear, MB probe and X sensor at analyzing A->G mutation in **Inh** analyte (see Table 4 for sequences). Linear probe was designed to position the SNS site close to the middle of the duplex; this ensures the best differentiation of mismatched from matched duplex [32]. The probe contained a quencher on the 3' end while the analyte was 5' fluorescein–labeled. At higher temperatures, the duplex dissociated thus increasing fluorescent signal.

Comparison of the three hybridization probes in SNS recognition

Figure 12 (lower panels) shows melting profiles of the three inh hybridization probes in complex with either matched (solid lines) or mismatched (dashed lines) analytes. Fluorescence of complexes formed by LP_inh probes (lower panel A) is shown as reverse values ($1-F_{target}/F_{background}$) in order to simplify data comparison with MB_inh (lower panel B) and X_inh probes (lower panel C), respectively. In addition, Figure 12C shows the melting curves of hybrids formed by X_m6_inh sensor (6-nt long m-binding arm). Melting temperatures of hybrids formed by all probes are given in Table 5. While a decent ΔT_m of 7.0 ^oC is seen for LP_inh probe, the MB_inh probe proved greater ΔT_m of 8.2, as predicted by Bonnet et al. [3] and Tsourkas and Bao [15]. Melting

temperatures for the X_inh probe were shifted to low values by ~ 30°C, while ΔT_m was broadened by 6-7°C (Table 5) as seen before for X_udg probe. The discrimination abilities of the three hybridization probes were compared using F_m/F_{mm} and $\Delta T_{1.5}$ (see chapter 2). MB_inh differentiated analytes with $\Delta T_{1.5}$ =12.7°C, which is only about 0.5°C broader than for LP_inh probe. The X_inh probe allowed SNS differentiation in the widest temperature range of all the three probes, $\Delta T_{1.5}$ = 19°C (Figure 13). These data are in agreement with that obtained for X_udg sensor. However, as opposed to the X_udg sensor which showed relatively high F_m/F_{mm} values at low temperature range (~5-15^{o}C), the X_inh didn't, its F_m/F_{mm} dependence with temperature being symmetric and resembling more a bell-shaped curve similar to MB and LP probes. This observation suggests that hybridization of X_inh probe with target analytes might have been close to equilibrium.

X_inh sensors' performance in SNS recognition

To compare the performance of different X_inh sensors, we designed a series of probes for recognition of **Inh** analyte of the same SNS site. We opted for two sets of X_inh probes. Within a set, the X probes contain the same strand ***f***, but the ***m*** analyte-binding arm varied from 6 to 9 nucleotides (X_m 6-9, Table 4). The two sets differed by the length of ***f***-analyte binding arm: one had 19 nt-long ***f*** (X_F_inh), while the other had 9 nt-long *f* (X_F_inh_short). Fluorescence above background was observed for all sensors in complex with mismatched analyte (Figures 14 and 15). For all sensors in complex with either matched or mismatched analytes, increasing the length of strand m

shifted T_m of hybrids to higher values as expected (Table 6). At first glance surprising, the complexes of sensors with shorter ***f*** (X_F_inh_short) had slightly higher T_m values than complexes of sensors with longer f (X_F_inh) (Table 6). However, unlike X_F_inh_short strand which is too short to fold, the longer X_F_inh strand folds into a stable secondary structure (T_m = 37.1°C, ΔG = -1.99 kcal/mole) at 10°C. In addition, the analyte forms also a stable secondary structure (ΔG = -6.02 kcal/mol) bellow 15°C. It has been shown that a probe's self-structure competes with hybridization to the target, decreasing complex stability, but without having an effect on thermal stability (T_m) [50]. However, when secondary structures were present in both target and probe molecules, there was a decrease not only in free energies of probe-target duplexes, but also in T_m, which might be our case, too [49]. Furthermore, the target and probe's secondary structures imposed kinetic obstacles which in our case might be translated into the different fluorescence values and shape of the melting curves for the two sensors at low temperatures – lower values and steep slopes for complexes with long ***f*** strand and higher values and slow slopes for complexes with short ***f*** strand (Figures 14, 15). Due to the high stability of secondary structure of the ***f*** strand below 15°C, there is a high competition between stem-forming and duplex-forming reactions, which slowed the hybridization of the long sensor to the analyte as observed. As temperature increased above 15°C, the ***f***-stem structure is less favorable (higher ΔG), complex prevailed, and fluorescence reached a plateau (Figure 14).

It is interesting to note that bellow ~14°C, the short sensors with more than 6 nt long m-analyte binding arm produced slight lower fluorescence in complex with the

mismatched analyte signal than with matched (Figure 15). Thus, while these short sensors were capable of mismatch discrimination bellow ~14 °C, the corresponding long sensors were not. We defined a temperature discrimination interval, $\Delta T_{1.5}$ given by the intersection of each F_m/F_{mm} curve with a threshold set at 1.5 (Figures 16, 17). The values calculated for each discrimination interval were as follow: 19°C (m=6), 16.6°C (m=7), 13.6°C (m=8), and 8.2°C (m=9) for the long X_inh sensors (Figure 16) and 16°C (m=6), 16°C (m=7), 13.4°C (m=8), and 6.6°C (m=9) for the short X_inh sensors, respectively (Figure 17). Thus, with values of ~3°C higher, the X_F_inh sensors performed better than their short counterparts. This was predicted by theory: as more conformational constrains are added to a probe, as wider its temperature discrimination range is expected to be [3].

Kinetic responses of the three types of hybridization probes

By recording fluorescence versus temperature curves while increasing (heating or dissociation curve) or decreasing (cooling or annealing curve) we aimed to study the dynamic response of the sensor depending on the increase or decrease of the temperature (Figure 18). It was assumed that the profiles should be symmetric in the case of thermodynamic equilibrium. In order to determine thermodynamic parameters these curves should be at equilibrium, meaning no hysteresis should be observed. As seen in Figure 18A-B cooling/heating curves for MB and linear probes have no hysteresis at a cooling/heating rate of 0.02°C /sec (19 sec equilibration times at each new temperature). However, the cooling and heating curves of X_udg sensor do not

overlapped and particularly in the low temperature regime (Figure 18D), even for heating/cooling rates as slow as 0.002°C /sec (600 sec equilibration times at each new temperature). Furthermore, for hybrids of X_udg sensors presented before (chapter 2) the dissociation and association processes were not reversible even at a rate of ~0.0007°C /sec (30 min equilibration times at each new °C). Thus, complexes of X_udg sensors were hard to equilibrate particularly in the low temperature regime, and they didn't reach thermodynamic equilibrium even if allowing very long equilibration times. Hybrids of X_inh sensor on the other hand, could be considered an intermediate case, since cooling/heating rate of 0.002°C /sec (600 sec equilibration at each °C) were slow enough to diminish hysteresis in both fully matched and mismatched annealing/melting curves, but not sufficient to eliminate it (Figure 18C). We concluded that under experimental conditions at a rate of 0.002°C /sec, the X_inh operated under close to equilibrium conditions. In order to evaluate the equilibration times for each probe-analyte hybrid, we extracted fluorescence data from melting curves presented in Figure 18A-D at different temperatures and heating rates. Data at 10 °C showed that LP_inh probe achieved equilibrium in a matter of few seconds, while MB_inh probes slightly slower (bellow 60 sec though), but not as slow as X_udg sensors which gave continuously growing slopes from 19 sec to 600 sec equilibration times for both matched and mismatched analytes (Figures 18E-F). For X_inh sensor, the slopes were not as steep as for X_udg sensor, and after 600 sec the signal for matched didn't flatten, but the one for mismatched seemed to reach a plateau (panel E). Data at 20°C, showed almost the same trend as at 10°C for all sensors (panel F). We concluded that

although the X_inh hybrids with matched and mismatched analytes didn't reach equilibrium by 600 s, they were close to reaching it. Fluorescence lines for complexes of X sensors with mismatched analyte are below the ones for corresponding complexes with mismatched analyte, as opposed to LP_inh or MB_inh probes for which the lines for mismatched rose above the ones for matched analyte. Thus, X sensors showed a better discrimination than LP_inh or MB_inh probes at both 10°C and 20°C.

Theoretically the hybridization for X_inh should take shorter time than for X_udg. On one hand, wild type (inh_C) and mutant (inh_T) analytes both fold into a single structure (Figure 19A), which is almost linear at 37°C. Also, the C->T mutation circled in blue is located on the linear portion of the analyte. The ***m*** and ***f***-analyte binding arms hybridize in tandem to the analyte: while ***f***-adaptor strand un-winds the slight secondary structure, the ***m***-binding arm strand hybridizes to the linear portion of the analyte (Figure 19A, red dashed line). On the other hand, wild type and mutant udg analytes fold in more complex secondary structures as shown in Figure 19B-C. The G->A mutation is located in the large loop of predicted structure. Unwinding these structures is expected to be slow, particularly at low temperatures, as observed in Figure 18D-E. First, at 10 °C f_udg forms a relatively stable stem and loop structure (ΔG = -1.99 kcal/mole), which has to be unwound prior to hybridizing to the analyte. Second, udg analyte's secondary structure is very stable at 10°C (ΔG = -9.08 kcal/mole). Thus, even though ***m*** and ***f*** strands cooperatively open the long stem of the wild type analyte (Figure 19B), the process is expected to be slow and it is not surprising that it didn't reach equilibrium even after 600 sec (Figure 18D-F). Opening the secondary structure of mutated analyte

should be even slower since adaptor stand m did not help in opening the stem of the analyte (Figure 19C). Thus, the hybridization process for X_inh should reach completion faster than for X_udg, which was observed in Figure 18 E, F.

Fluorescence responses of X sensors with stem-forming analyte binding arms

In chapter 2 we demonstrated that operation under non-equilibrium conditions improves SNS discrimination at low temperatures for X_udg sensor. In order to enable SNS achieve the non-equilibrium performance of X_inh sensor, we introduced additional conformational constrain in the form of stem loop in analyte binding arm of adaptor strand ***m*** (Figure 20). Some of these sequences were predicted to have more than one possible conformation, however only the lowest energy structures are considered. The ***f***-analyte binding arm is either long (X_F_inh) and folds into a stable structure at low temperature, or short (X_F_inh_short) which does not fold (Figure 20). A variant of X_F_inh is X_F_inh2, a one bp shorter fragment, which folds into a stable structure at 10°C (ΔG = -1.99 kcal/mole). Using X_F_inh2 instead of X_F_inh, allowed the point mutation to be positioned in the middle of the ***m*** fragment complementary to the analyte, which has been shown to result in maximum specificity.

In the absence of the analyte, the stem-forming sensor consisting of 18 bp duplex formed between UMB1 and its MB-binding arms, would have one (short sensor) or two (long sensor) terminal stem-loops corresponding to each analyte binding arm. Figure 20 present two long sensors containing a 4-nt long stem (X_m6sl4) and a 5-nt long stem (X_m8sl5), respectively. Both sensors produced a high background (Figure

20, dash-dotted lines). Both sensors gave a high fluorescence background (Figure 20, dashed dot lines). Since there is no significant hybridization between ***m*** or ***f-***analyte binding arms and UMB1, the high fluorescence background observed, might be due to the high number of base pairs formed by these sensors at low temperature, 27 bp (X_m6sl4) and 28 bp (X_m8sl5), respectively. Once the analyte is added, the resulting fully matched hybrids of both stem-forming sensors melted in two steps. The sensor with m6sl4 stem-adaptor strand has T_m = 13°C for the first step, and T_m = 30.3°C for the second step. The corresponding stemless hybrid melted in one step at 31.4°C. The sensor with m8sl5 stem-adaptor strand has T_m = 17°C for the first step, and T_m = 37.3°C for the second step. The corresponding stemless hybrid melted also in one step at 37.2°C. Mfold software predicts very stable ***m***-stem analyte binding arms for both sensors at 5°C: ΔG = -6.33 kcal/mole (X_m6sl4_inh) and ΔG = -7.61 kcal/mole (X_m8sl5_inh), respectively. The high stability of the sensors resulted from both the free energy contribution of the m-stems and of the f-stem, might explain the complex melting behavior of hybrids formed by these sensors (see traces labelled stem m in Figure 20). The first melting step might be in fact the result of ***m***-analyte binding arm falling off the analyte and self-folding into the corresponding stable stem. The residual complex fully melted in the second melting step similar to the stemless sensors (see traces labelled linear m in Figure 20). It is worth noting that fluorescence signals of hybrids with stem-forming ***m*** are lower than those of hybrids with stemless ***m***. This is more likely due to the difference in hybridization rates of the two types of sensors, the one with ***m*** stem being expected slower than the stemless ***m*** one. Although the stem-forming sensors of

this design gave high background and had a complex melting behavior, their ΔT_m was ~0.8°C higher than of stemless sensors (Table 7), which proved a modest increase in selectivity.

It has been shown that a longer or more stable stem should give more specific MBs, since the difference in temperature of the phase transition between the matched and mismatched analytes is increased. In order to achieve this goal, we designed a set of stem-forming X probes with ***m***-analyte binding arms predicted to fold in secondary structures comprising 2 (m8sl2), 4 (m8sl4) or 5 (m8sl5) nt-long stems, respectively. In order to have less variable in the system we kept the ***f***-analyte binding arm stemless (f_inh_short, Table 4). To allow a better comparison, the melting curves of matched and mismatched complexes formed by these sensors were normalized to a value of 1 (Figure 21A-D). Predicted secondary structure of ***m***-binding arm for each sensor is shown in the insert of each panel. Their stability at 5°C, expressed by the more negative free energy (ΔG_{mstem}) with lengthening the stem, increased in the order: m8sl2 (ΔG =-3.21 kcal/mole) < m8sl4 (ΔG =-5.45 kcal/mole) < m8sl5 (ΔG =-7.61 kcal/mole). The stemless ***m*** has ΔG_{m8}=2.28kcal/mole. Each stem-loop ***m***-binding arm has 8 bases complementary to the analyte, and in each case not only the loop but also one arm of the stem participates in hybridization (share-stem probe). It has been shown that share-stem probes can shift the equilibrium towards probe-analyte complex (AS) [33]. Additionally, we used high concentrations of both adaptor strands (1.25 uM) for the same purpose. Since the free energy of probe-target was the same for all sensors (8-nt duplex, ΔG_p = 0.3 kcal/mole), it was expected that the more bp were added to the stem

(thus lowering the free energy), the higher the difference between ΔG_p and ΔG_{mstem}, and so the preference for hybridization to be less favorable. We observed this in our experiments (Figure 19), since fluorescence signal of fully matched complex is slightly decreasing from panel A (no stem) to panel D (5 bp stem). In addition, a point mutation in the target would increase the difference between ΔG_p and ΔG_{mstem} even further, and so it was expected to see an amplified effect on binding of the sensors to mismatched target. This was again the case, but only to the 4-bp stem sensor (panels A to C), the 5-bp stem sensor (m8sl5) showing a more complex melting behavior (panel D). It is possible that the melting of hybrids capable of forming very stable ***m***-stem analyte binding arms (m8sl5) to proceed by detachment of ***m*** from the analyte first, followed by folding of it as discussed above. Hybrids of stem-forming sensors with short ***f*** adaptor strands gave higher melting temperatures than the ones with longer ***f*** for the same considerations mentioned above (Figure 15) for linear ***m*** and short ***f***-analyte binding arm (Table 7). As predicted by theory, complexes of stem-forming sensors with 8 nt-long analyte binding arms gave a slightly broader ΔT_m than of corresponding stemless sensors, ~1.5°C higher (X_F_inh_short in Table 7). The highest ΔT_m is shown by the sensors containing the longest stem (m8sl5), while the best discrimination (F_m/F_{mm}) is achieved by the sensors containing a 4-nt long stem (m8sl4).

Keeping into account these findings, we designed a stem-forming sensor, with ***m***-binding arm containing a stable 4-nt stem and 4-nt loop structure (ΔG=-5.5 kcal/mole at 5°C), and a total of 9 bases complementary to the part of analyte, which includes the mismatch position (m9sl4, Figure 22B, upper panel and insert). For better allele

differentiation, the complementary sequence was chosen such to allow the SNP to fall in the middle of it (upper panels Figure 22A-B) [16]. The other analyte-binding arm (f_inh2) was long and folded also (insert panel A) into a relatively stable stem (ΔG=-2.37 kcal/mole at 5°C). Thus, this stem-forming sensor (X_m9sl4_inh2) contained greater conformational constraints than previous stemless ***m*** probe (X_m9_inh2), and so it was expected to have a high SNP differentiation ability [15]. The ***f***-binding arm to the analyte was the same for both sensors (Table 1). All profiles were normalized to a value of 1, such that to better compare the different melting curves. The hybrid of X_m9_inh2 sensor with fully matched analyte showed the highest fluorescence, and its melting followed the path explained earlier for the X_m9_inh sensor (Figure 14). At low temperatures (<15°C), fluorescence of the hybrid with fully matched analyte falls below that of the hybrid with mismatched analyte, giving an unusual shape to the melting curve, which is different than observed before (Figure 22A). However, increasing the concentrations of both staples didn't improve discrimination of stemless ***m*** sensor at low temperature. Discrimination was indeed significantly improved by replacing the linear ***m*** with stem ***m***-analyte binding arm as shown in Figure 22B. The highly stem sensor X_m9sl4_inh2 discriminated matched from mismatched analyte in a wider temperature range ($\Delta T_{1.5}$=35°C) than its stemless counterpart X_m9_inh2 ($\Delta T_{1.5}$ = 10.2°C) (Figure 22C). However, a negligible difference in ΔT_m was observed between the two types of sensors (Table 8). The ***m***-stem slowed down melting of mismatch containing complex more than of fully match containing complex, ensuring a better differentiation between the two.

In order to determine the equilibration times needed to achieve maximum fluorescence, a set of cooling/melting experiments were performed in parallel for both sensors (Figure 23). The samples were first melted at 95°C, then cooled and heated again to allow them equilibrate for different times at each °C: 19 sec, 60 sec and 600 sec, respectively. Figure 23 panel A shows the cooling-heating curves for stemless sensor, and panel B for ***m***-stem sensor. In general melting/cooling profiles for hybrids of stemless sensor recorded at a given equilibration time didn't overlap, however towards the 600 sec equilibration times the difference became much smaller. However, melting/cooling profiles for hybrids of m-stem sensor didn't show any tendency to equilibrate even at the highest equilibration time allowed. Thus, although hybrids of none of the sensors reached thermodynamic equilibrium, we can say that the ones of stemless sensors are closer to equilibrium than the ones of stem-m sensors. Melting profiles of hybrids containing fully matched analytes for both sensors had similar slopes (solid lines), but they were different for hybrids containing the mismatched analytes (dashed lines): slower melting slopes were given by stem-forming than stemless sensors, particularly at short equilibration times. Cooling profiles of complexes formed by each sensor either with matched or mismatched analytes were also different: stemless ***m*** sensors gave steeper slopes than stem-forming ***m*** sensors. These observations point to the difference in hybridization rates between the hybrids with matched and mismatched analytes for both X_inh, but more for the stem-forming sensor, which showed slower hybridization rates. It has been shown that secondary structures slow down hybridization [51], but at the same time accelerate melting [52],

which at least partially explains the complex cooling-heating profiles seen in Figure 23. For each sensor the fluorescence dependence with equilibration times was plotted at 10°C (panel C) and at 22°C (panel D), respectively. Fluorescence data were extracted from the melting portion of the thermal profiles shown in Figure 23 A and B. At 10°C fluorescence reached a plateau only for the fully matched hybrid of stemless sensor, all the other samples showing fluorescence dependencies with different slopes, and so slow kinetic. At 22°C both matched and mismatched hybrids of stemless sensor seemed to plateau, but not the corresponding hybrids with stem-forming sensor. Overall, it seems that the stemless sensor was close to equilibrium conditions at least at 22°C, while stem forming sensor was not at both chosen temperatures. The performance in SNP discrimination of the first was poor ($\Delta T_{1.5}$ = 10.2°C). However, by introducing the maximum possible conformational constraints allowed by our spatially designed DNA probe it was possible to shift its operation to non-equilibrium conditions and so to improve its performance ($\Delta T_{1.5}$ = 35 °C). Thus, this work points towards a new strategy for the design of highly selective hybridization sensors which operate in non-equilibrium conditions in a close to ambient temperature range.

Fluorescence response of X_inh sensor to a C->T mutation

Melting profiles of complexes formed by X_m7G_inh sensor (see Table 4 for sequences) with fully matched and mismatched analytes are shown in Figure 24 A. The complex with fully matched analyte melted at 36.7°C, while with mismatched analyte at 25.2°C, which gave a ΔT_m of 11.5°C. The intersection of the F_m/F_{mm} curve with the

threshold value set at 1.5 ($\Delta T_{1.5}$) gave a discrimination interval for this sensor of 18.2°C. However, by changing only one single nucleotide in the m-analyte binding arm (X_m7G_inh), namely by replacing the middle base which is a G with an A (X_m7A_inh) we made this sensor very sensitive to a C->T mutation in the analyte. Thus, the X_m7A_inh sensor discriminated mismatched from matched analyte from 5 to 37.5°C (Figure 24C), about double than the X_m7G_inh sensor. The complexes of X_m7A_inh sensor with fully matched analyte melted at 35.5°C, while with mismatched analyte complex at 25.9°C, respectively, which gives a ΔT_m of 9.6°C. So, even though ΔT_m of X_m7A_inh sensor is lower than of X_m7G_inh, its $\Delta T_{1.5}$ improved considerably.

Recognition of different types of SNS by X sensor

In this study, the performance of X sensor to detect different SNS (i.e deletion, insertion or SNP) was compared. The analytes tested had the same main structure as the inh_C analyte, but modified such that one C nucleotide was either substituted with a T nucleotide (inh_T), deleted (inh_C_del), or inserted (inh_C_ins) at the same position in the sequence (Figure 25 top panels). Each mutation destabilized the corresponding complex with the X sensor to a certain degree as seen in the difference in melting temperatures: the complex with SNP mutation melted at the lowest temperature, while the one with a C insertion at the highest (Figure 25, left panel and Table 9). The performance of X_inh sensor to detect different types of mutations indicated as $\Delta T_{1.5}$ intervals increased in the following order SNP<Del<Ins as shown in Figure 30, left panel. These latest examples showed that the X sensors were able to recognize not

only SNP but also different types of SNS in a broad temperature range including ambient temperature.

Overall for this chapter, we can conclude that it was possible to broaden the interval for SNS differentiation by operating under non-equilibrium conditions. This opens a new venue for the design of highly selective hybridization probes. Thus, X sensors could be utilized in qPCR, microarrays, as well as RNA analysis in living cells and for ambient temperature point-of-care diagnostics.

Figures and tables

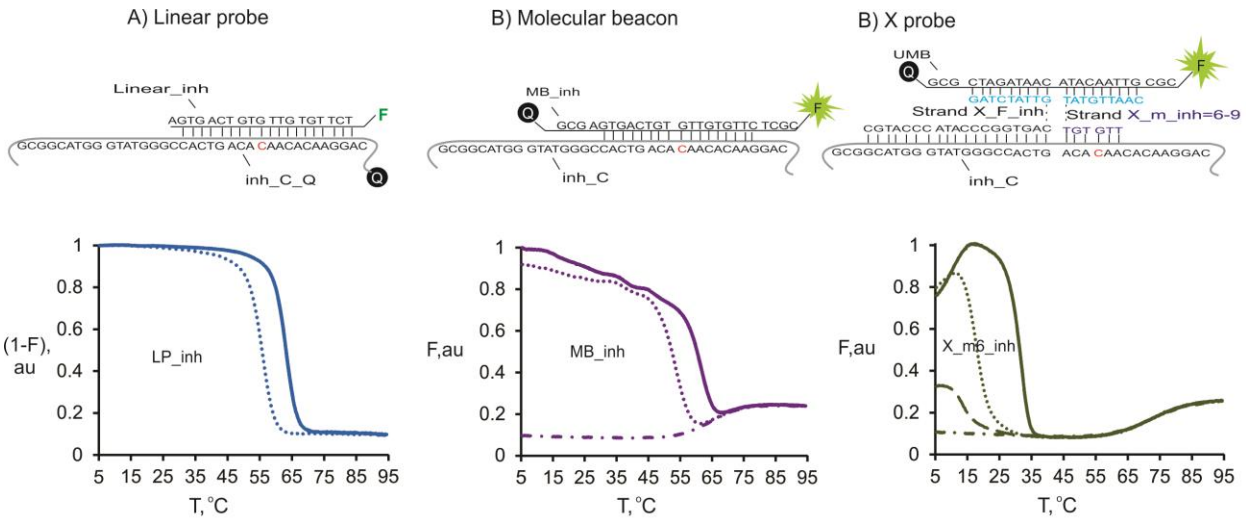

Figure 12. SNS recognition by different types of hybridization probes.

A) Linear probe. Upper panel: Linear probe hybridized to the matched analyte. The analyte was labeled by a quencher dye (Q), while the probe was conjugated with a fluorophore (F) to enable fluorescent detection of complex formation. Bottom panel: Reverse fluorescence (1-F) of the probe in the presence of matched Inh_C_Q (solid lines) and mismatched (dotted lines) Inh_T_Q analytes at different temperatures. The reverse fluorescence is presented to simplify comparison the data with panels B and C since linear probe, as designed, increased fluorescence upon melting, not decreasing as MB probe and X sensor.

B) Molecular beacon probe. Upper panel MB probe hybridizes to complementary target and produces fluorescent signal. The SNP position is shown in red, and the mutation is C ->T.

C) X sensor. Upper panel: Fluorescent crossover (X) complex formed by strands **X_F_inh** and **X_m_inh** when binding to analyte **Inh_C** and MB probe. MB-binding arms of strands ***f*** and ***m*** are in cyan. Low panel: Melting temperature curves for X sensors with 6-nucleotides long m-analyte binding (**X_m-6_inh** in Table 2).

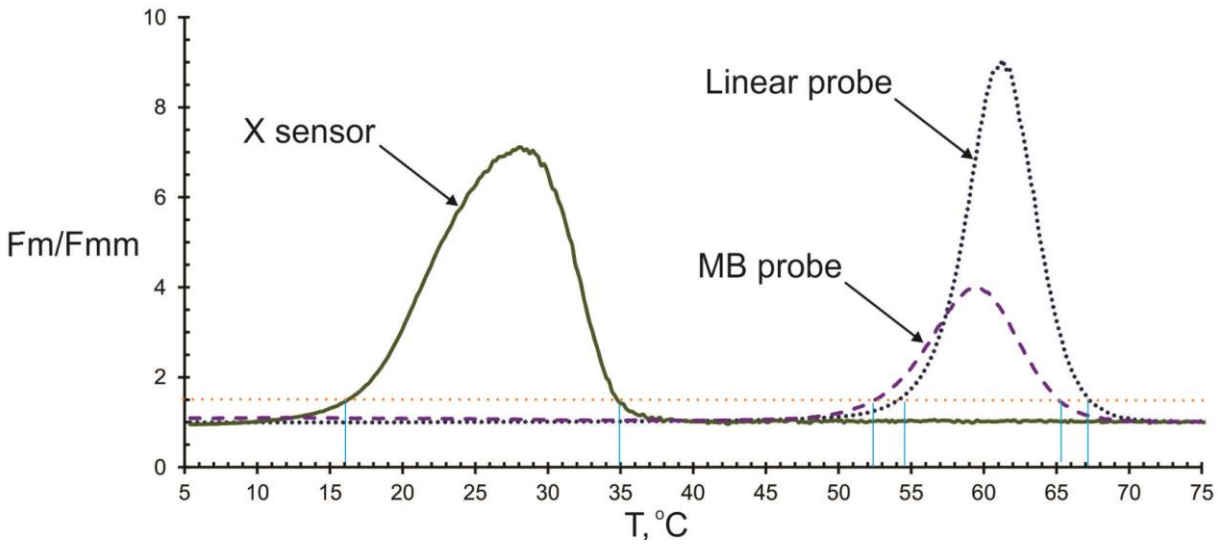

Figure 13. Differentiation range for the three types of hybridization probes.

The ratio of fluorescence produced by each probe in the presence of fully matched analyte (F_m) to that of mismatched analyte (F_{mm}) are plotted against temperature for LP_inh (blue dotted line), MB_inh probe (purple dashed line) and X_inh sensor (X_m-6_inh, green solid line). The threshold F_m/F_{mm} ~ 1.5 is indicated by orange dotted line.

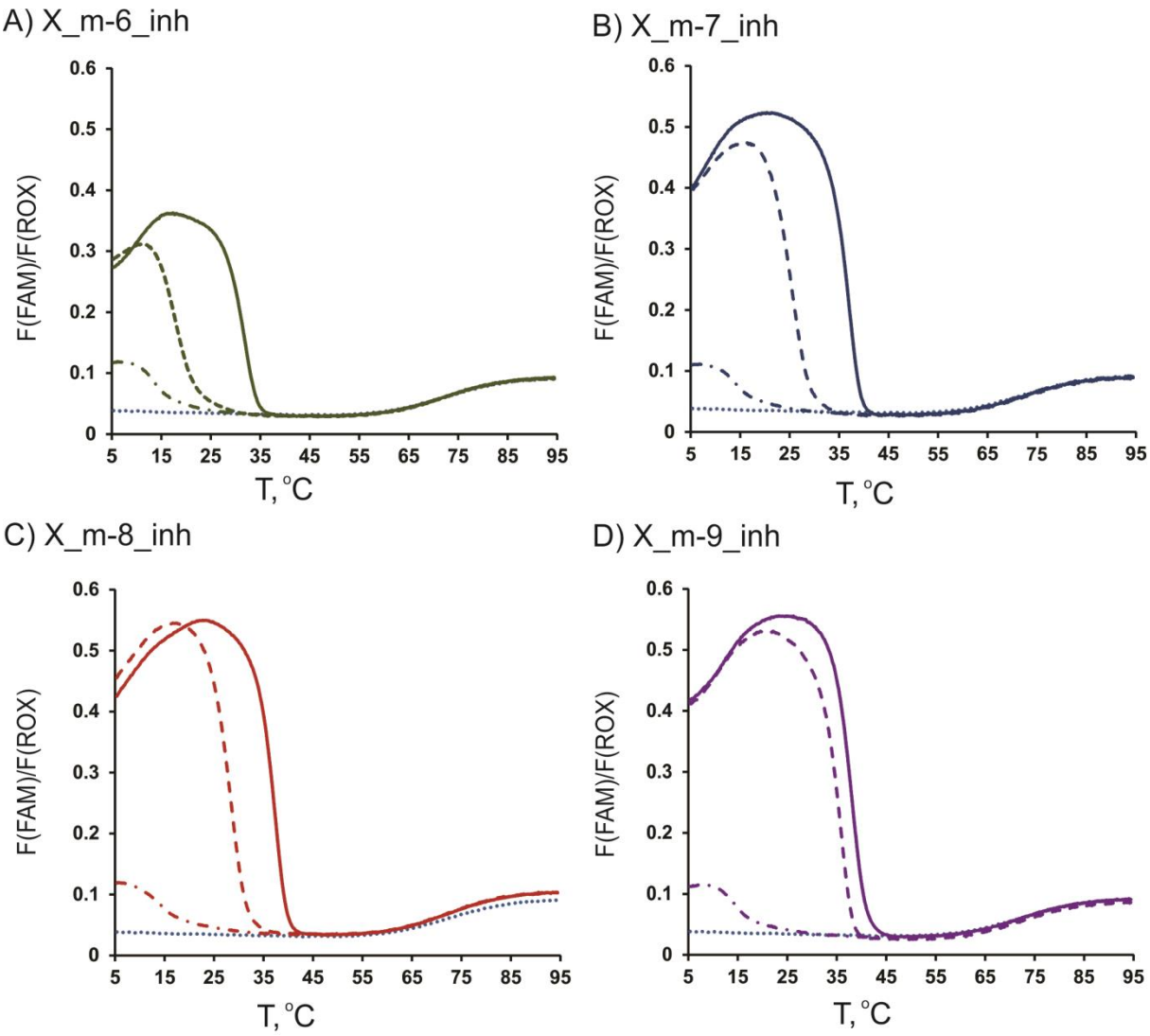

Figure 14. X_inh **sensor's fluorescence dependence on the length of m-analyte binding arms (y).**

Melting curves of X_inh sensors with different length m-analyte binding arm in complex with fully matched (solid lines) or mismatched analyte (dashed lines). Dotted-lines represent UMB1 alone. Background fluorescence is represented by dash-dotted lines. The reaction mixtures contain 50 mM Tris-HCl (pH = 7.4), 100 mM $MgCl_2$, 50 nM UMB1, 200 nM X_F_inh, and 120 nM X_m-y_inh, where y = 6 nt (A), 7 nt (B), 8 nt (C), and 9 nt (D) respectively.

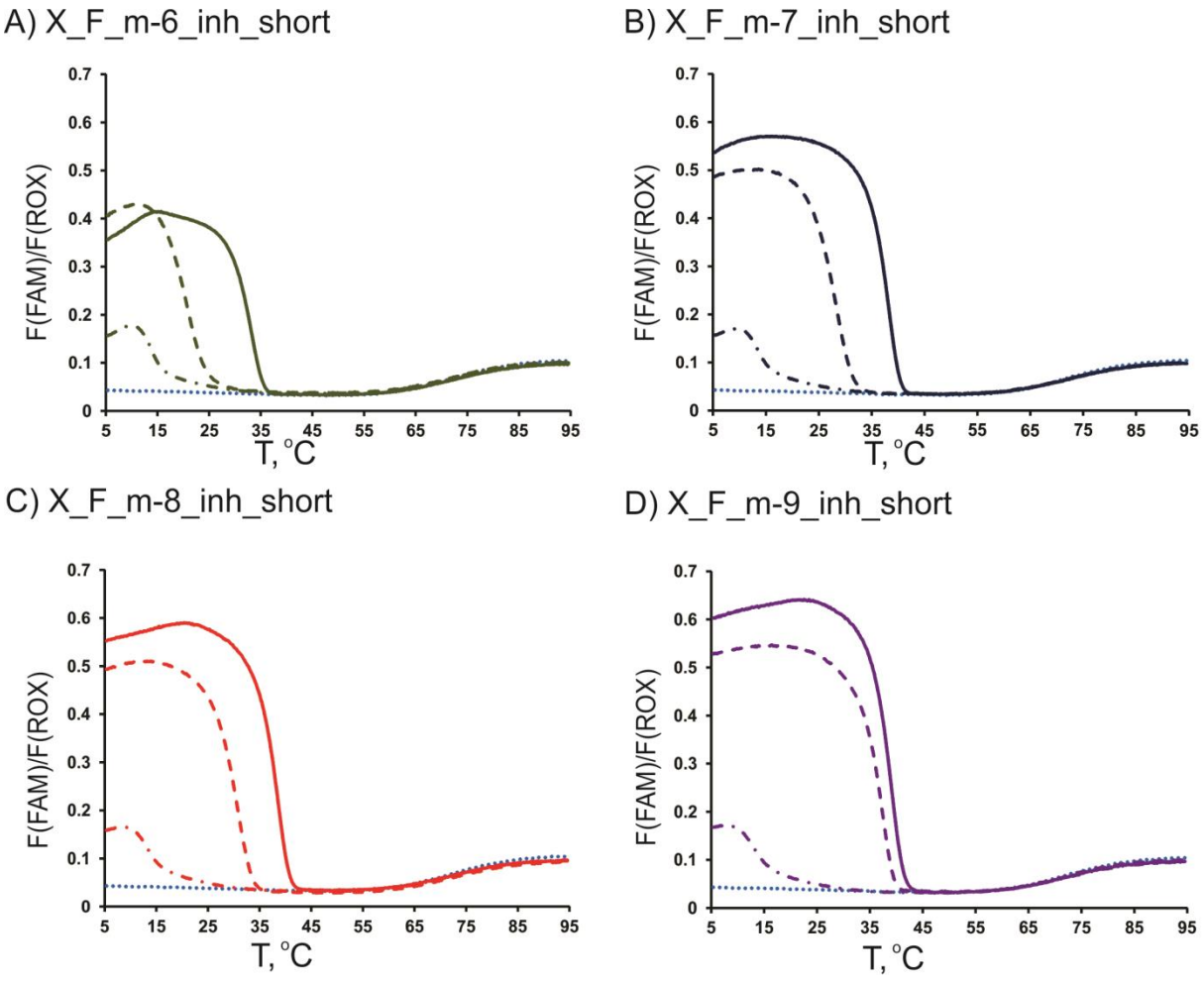

Figure 15. X_inh_short **sensor's fluorescence dependence on the length of m-analyte binding arms (**y**).**

Melting curves of X_inh sensors with different length m-analyte binding arm in complex with fully matched analyte (solid lines) or with mismatched analyte (dashed lines). Dotted-lines represent UMB1 alone. Background fluorescence is represented by dash-dotted lines. The reaction mixtures contain 50 mM Tris-HCl (pH = 7.4), 100 mM $MgCl_2$, 50 nM UMB1, 200 nM X_F_inh_short, and 120 nM X_m-y_inh, where y = 6 (A), 7 (B), 8 (C), and 9 (D) respectively.

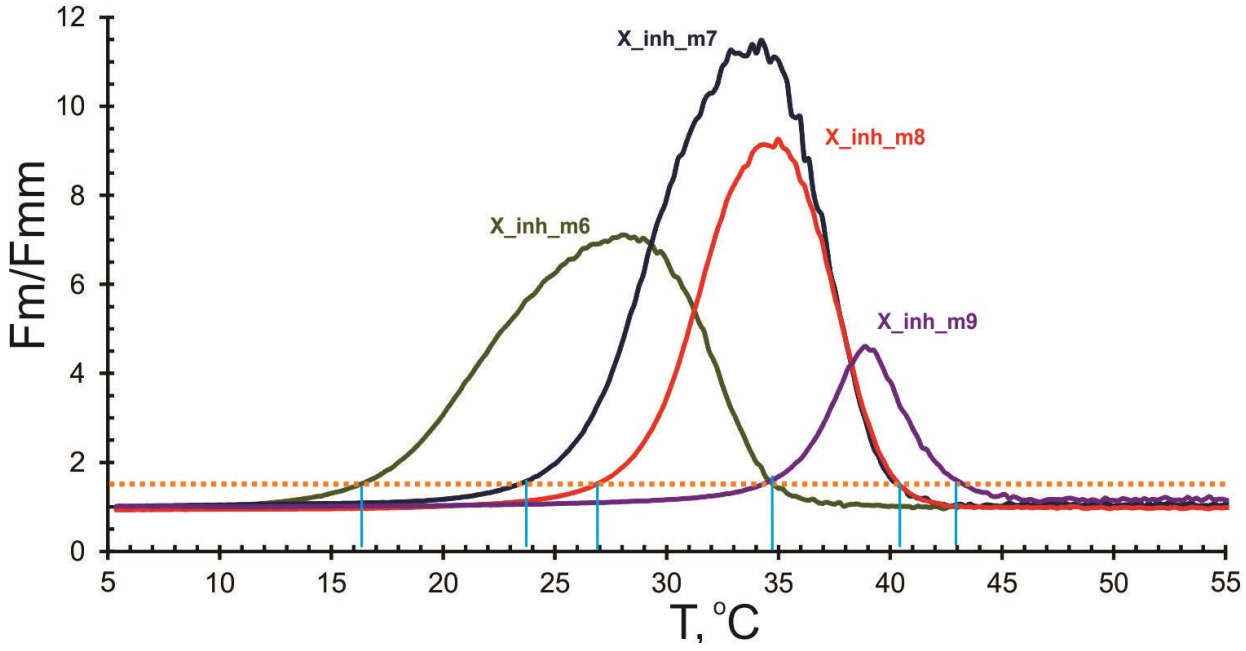

Figure 16. Temperature range discrimination for different X_inh **sensors.**

Ratio of fluorescence responses of **X_inh** sensors to the presence of fully matched (F_m) to mismatched (F_{mm}) analytes with temperature. The temperature range broadens with increasing the length of m-analyte binding arms. The threshold F_m/F_{mm} ~ 1.5 is indicated by orange dotted line.

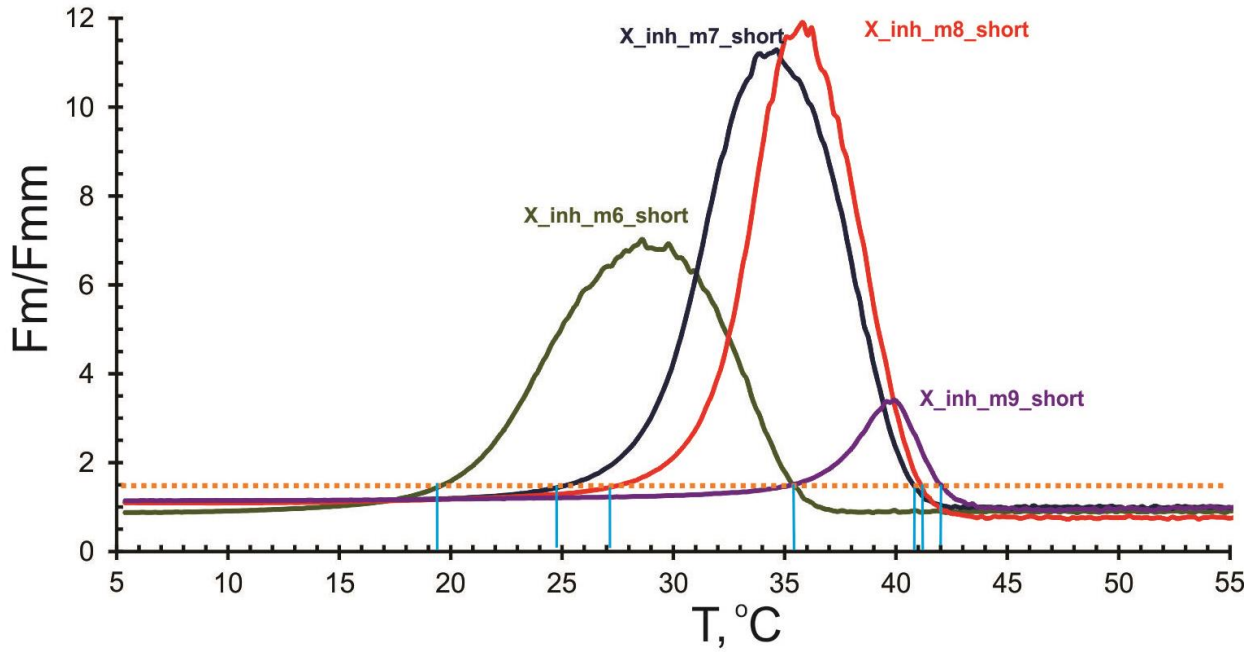

Figure 17.Temperature range discrimination for different X_inh_short sensors.

Ratio of fluorescence responses of **X_inh** sensors to the presence of fully matched (F_m) to mismatched (F_{mm}) analytes with temperature. The temperature range broadens with increasing the length of m-analyte binding arms. The threshold F_m/F_{mm} ~ 1.5 is indicated by orange dotted line.

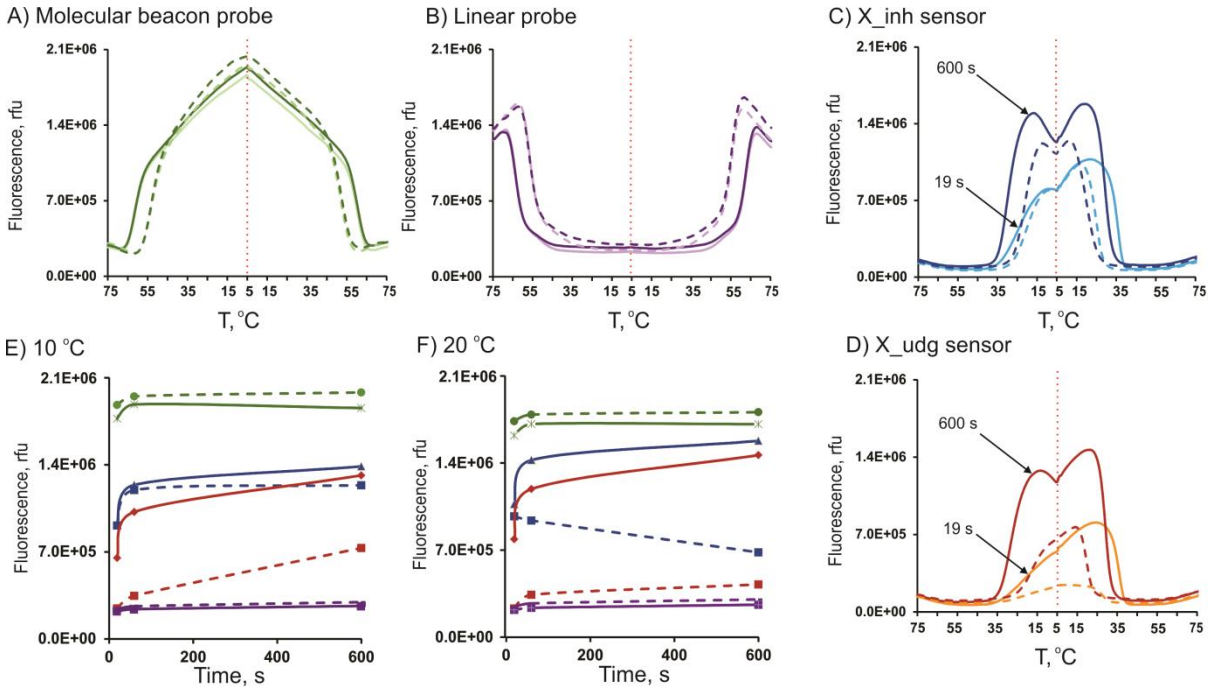

Figure 18. Kinetic responses of the three types of hybridization probes.

A)-D): Cooling-melting curves of molecular beacon probes, MB_inh (A) linear probes, LP_inh (B), and X sensors – X_inh (C) and X_udg (D), respectively. The figures show data recorded at 19 s (light colors) and 600 s (dark colors) equilibration times for each new temperature. Solid lines represent melting of fully matched complexes, while dashed lines the melting of mismatched ones with corresponding probes. The vertical red dotted line starting at 5°C shows the boundary between the cooling (left side) and the heating (right side) curves.
E)-F): Kinetic responses of all sensors at 10°C (E) and 20°C (F), respectively. Data were taken from the melting curves presented in figures A) - D) and from the on heating curves recorded for 600 s equilibration time (not shown).

Assays' conditions: (A) 50 nM MB_inh and 100 nM target (either inh_C or inh_T), (B) 50 nM LP_inh and 100 nM target (either inh_C_Q1 or inh_T_Q1), (C) 50 nM UMB1, 120 nM mG-7_inh, 200 nM F_inh, 100 nM target (either inh_C or inh_T), and (D) 50 nM UMB1, 120 nM m-7_udg, 200 nM f3_udg, 100 nM target (either udg_G_2 or udg_A_2 for X_udg). In all cases the buffer contained 50 mM Tris-HCl (pH = 7.4), 100 mM $MgCl_2$ and 0.1% Tween 20.

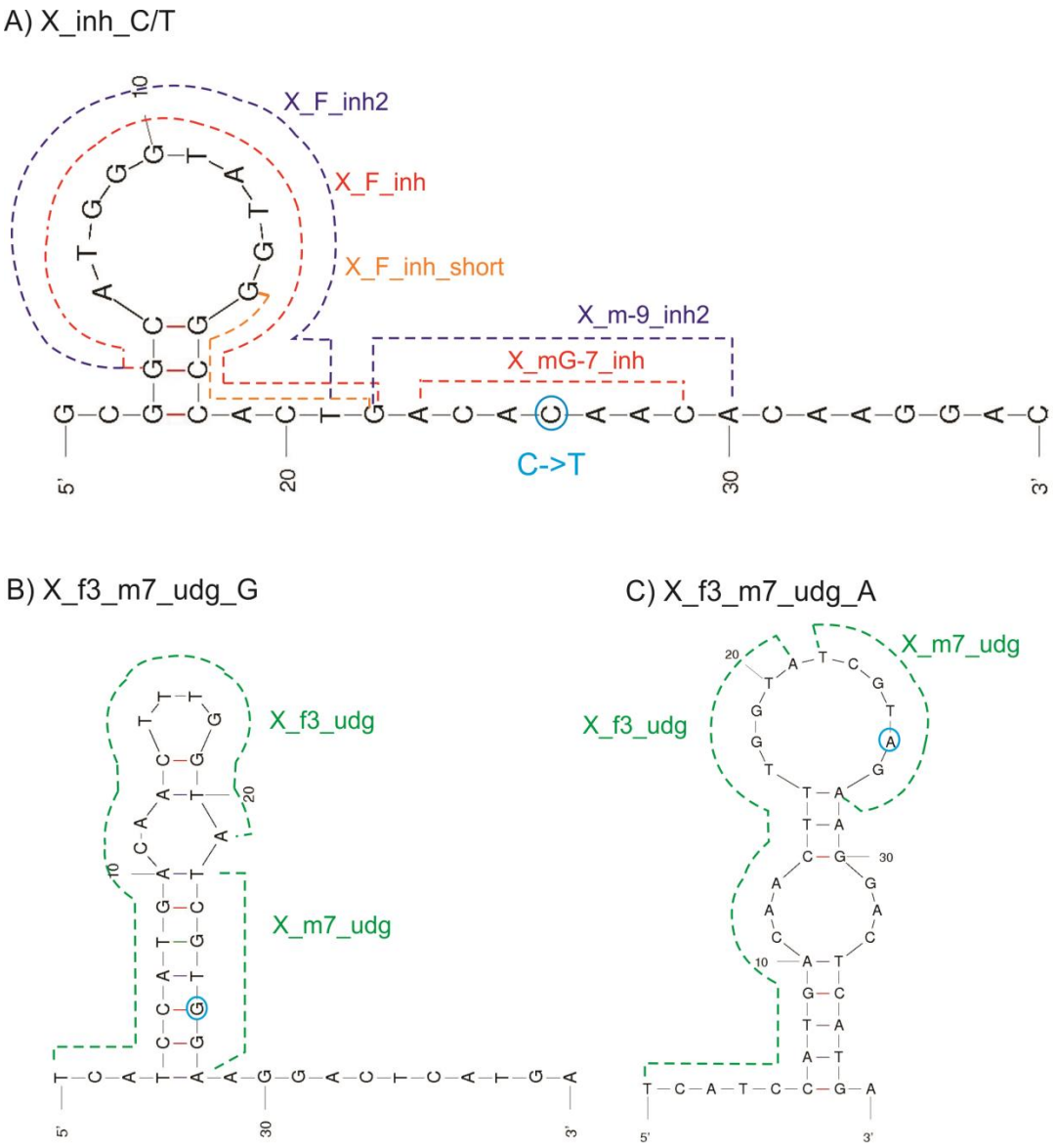

Figure 19. Folding of DNA analytes at 37°C under experimental conditions and the X probe's hybridization position.

A)-C): mfold predicted structures of inh_C/T (A), udg_G (B), and udg_A (C) analytes at 37°C, 50 mM monovalent ion and 100 mM Mg^{2+} are shown in black. Note that there is only one structure for inh analyte, while for udg there are two structures, one for each mutation. The m and f–analyte binding arms of X_inh and X_udg sensors are sketched along the corresponding analytes for better representation of hybridization sites. Three X_inh sensors are shown color coded along Inh_C/T analyte: (A) X_m-9_F_inh2 (purple), X_mG-7_F_inh (red) and X_mG-7_F_inh_short (yellow). For the last 2 sensors the m-binding arm is the same, so only one is shown for clarity, (X_mG-7_inh, in red). One X_udg sensor is shown along udg_G/A analytes: (B, C) X_m-7_udg. The point mutations are bleu circled.

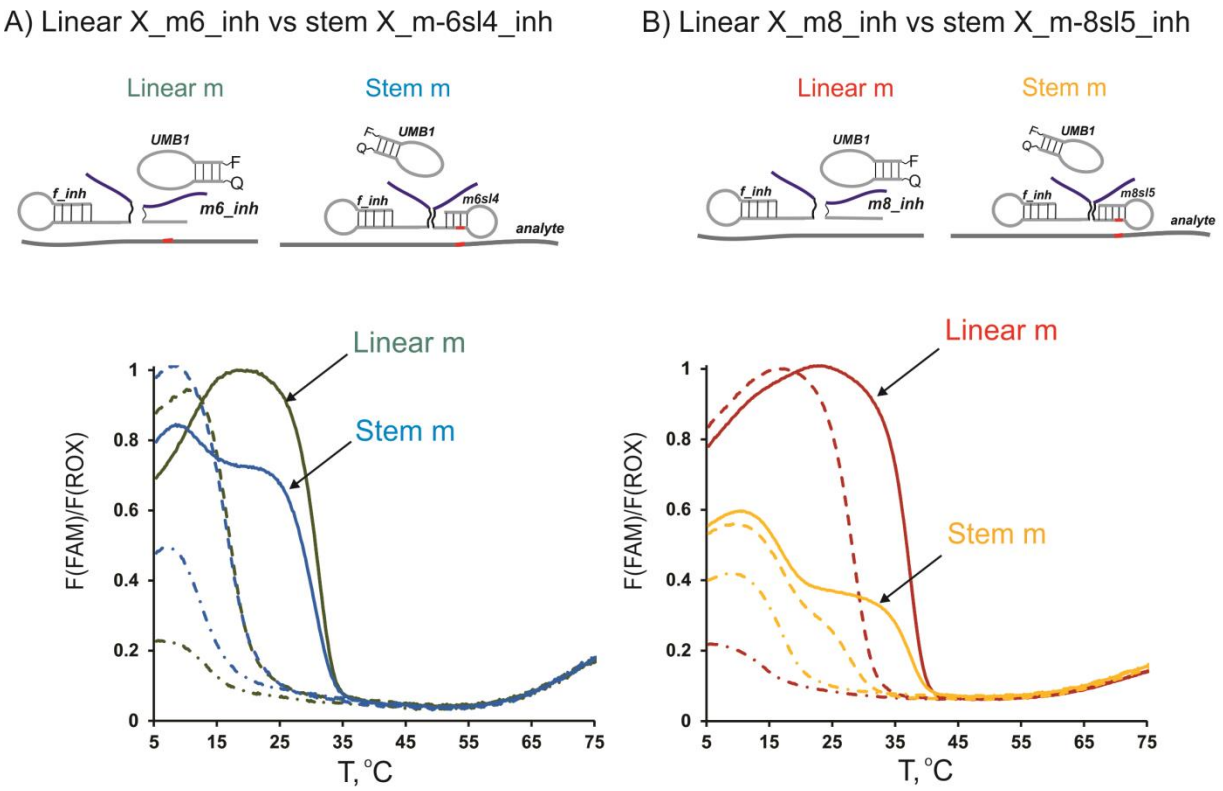

Figure 20. Melting curves of m stem-forming or linear m DNA sensors hybridized to target DNA.

A) Upper: Hybridization of stem-forming m adaptor strand m6sl3 to the analyte in the presence of UMB1 and f_inh (right). Strand m6sl4 has a 4 base pair stem, and 6 of its nucleotides form the binding arm to analyte. On the left is shown the same process but for a 6-nt long linear m analyte binding arm. Bottom: melt curves of complexes with stem-forming (bleu) and linear (green) m-analyte binding arms, respectively.

B) Upper: Hybridization of stem-forming m adaptor strand m8sl5 to the analyte in the presence of UMB1 and f_inh (right). Strand m8sl5 has a 5 base pair stem, and 8 of its nucleotides form the binding arm to analyte. On the left is shown the same process but for a 8-nt long linear m analyte binding arm. Bottom: melt curves of corresponding complexes with stem-forming (yellow) and linear (red) m-analyte binding arms, respectively.

The reaction mixtures contain 50 mM Tris-HCl (pH = 7.4), 100 mM $MgCl_2$, 0.1% Tween 20, 50 nM UMB1, 200 nM strand ***f***, and 120 nM strand ***m.***

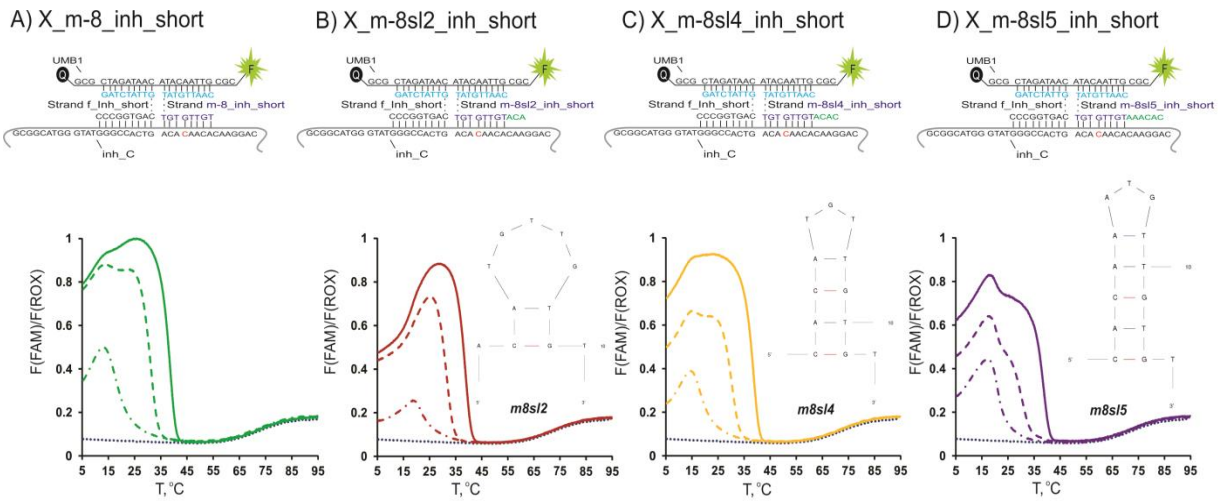

Figure 21. Melting curves of hybrids containing stemless or stem-forming 8 nt-long m-analyte binding arms.

A) Upper: Complex formed upon hybridization of stemless X_m-8_inh adaptor strand to inh_C analyte in the presence of UMB1 and X_f_inh_short. Bottom: melt curves of fully matched (inh_C, solid, green line) and mismatched complexes (inh_T, dashed green line).

B) Upper: Complex formed upon hybridization of stem-forming X_m-8sl2_inh adaptor strand to inh_C analyte in the presence of UMB1 and X_f_inh_short. Bottom: melt curves of fully matched (inh_C, solid red line) and mismatched complexes (inh_T, dashed red line).

C) Upper: Complex formed upon hybridization of stem-forming X_m-8sl4_inh adaptor strand to inh_C analyte in the presence of UMB1 and X_f_inh_short. Bottom: melt curves of fully matched (inh_C, solid yellow line) and mismatched complexes (inh_T, dashed yellow line).

D) Complex formed upon hybridization of stem-froming X_m-8sl5_inh adaptor strand to inh_C analyte in the presence of UMB1 and X_f_inh_short. Bottom: melt curves of fully matched (inh_C, solid purple line) and mismatched complexes (inh_T, dashed purple line).

The most stable secondary structures predicted by mfold for various m-stems in the assay's conditions* at 10°C are shown in the inserted figures.

*Assays' conditions: 50 nM UMB1, 1.25 uM strand *m*, 1.25 uM strand *f*, 100 nM target (either inh_C or inh_T) mixed in a buffer containing 50 mM Tris-HCl (pH = 7.4), 100 mM $MgCl_2$ and 0.1% Tween 20.

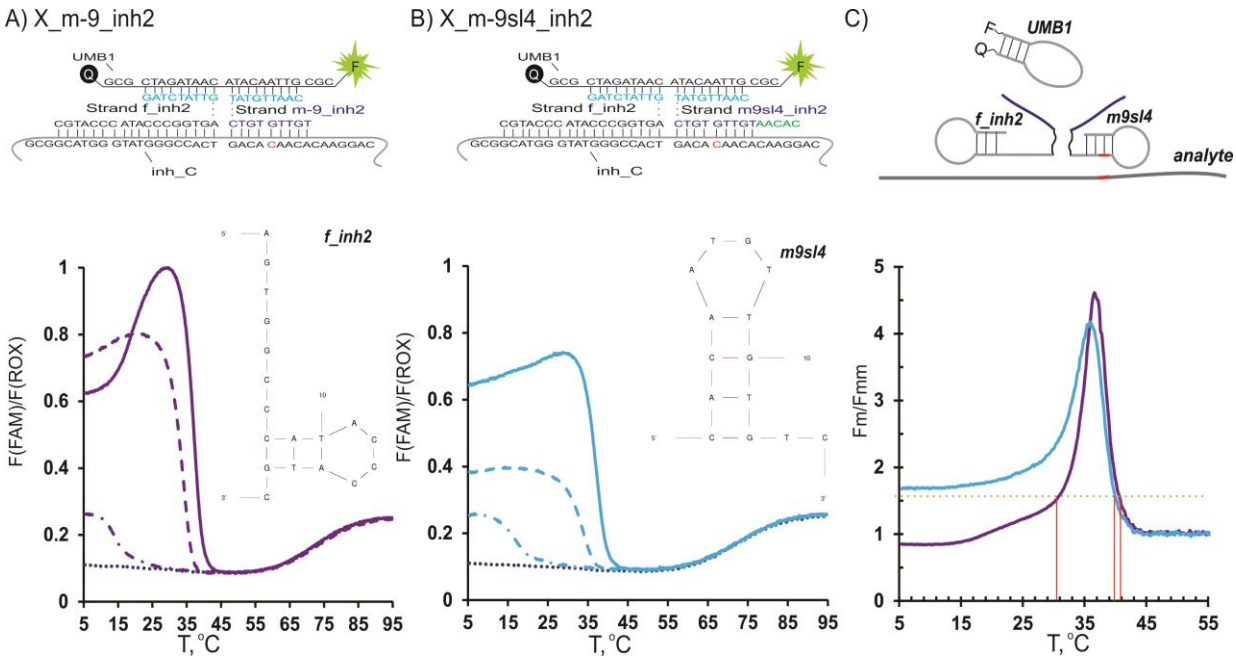

Figure 22. Melting curves of hybrids containing stemless or stem-forming 9 nt-long m-analyte binding arms.

A) Upper: Complex formed upon hybridization of stemless X_m-9_inh2 adaptor strand to inh_C analyte in the presence of UMB1 and X_f_inh2. Bottom: corresponding melt curves of fully matched (inh_C, solid purple line) and mismatched complexes (inh_T, dashed purple line).

B) Upper: Complex formed upon hybridization of stem-forming X_m-9sl4_inh2 adaptor strand to analyte inh_C in the presence of UMB1 and X_f_inh2. Bottom: corresponding melt curves of fully matched (solid blue line) and mismatched complexes (dashed blue line).

C) Upper: Schematic of X_m-9sl4_inh2 and X_f_inh2 hybridization to the analyte in the presence of UMB1. The locations of the SNP on analyte, and of its complement on m adaptor strand are red underline. Note that the base on m-binding arm corresponding to the mismatch in the analyte is part of the stem. Bottom: Ratio of fluorescence responses of X_inh sensors containing stemless (purple) or stem-forming (bleu) m-analyte binding arms to the presence of fully match (F_m) to mismatched (F_{mm}) analytes at different temperatures. The threshold F_m/F_{mm} ~ 1.5 is indicated by orange dotted line.
Inserted figures depict folding of adaptor strands f-inh2 (panel A) and m-9sl4 (panel B), respectively as predicted by mfold in the conditions of the assay at 10°C.
Assays' conditions: 50 nM UMB1, 60 nM ***m*** strand, 120 nM ***f*** strand, 100 nM target (either inh_C or inh_T) mixed in a buffer containing 50 mM Tris-HCl (pH = 7.4), 100 mM $MgCl_2$ and 0.1% Tween 20.

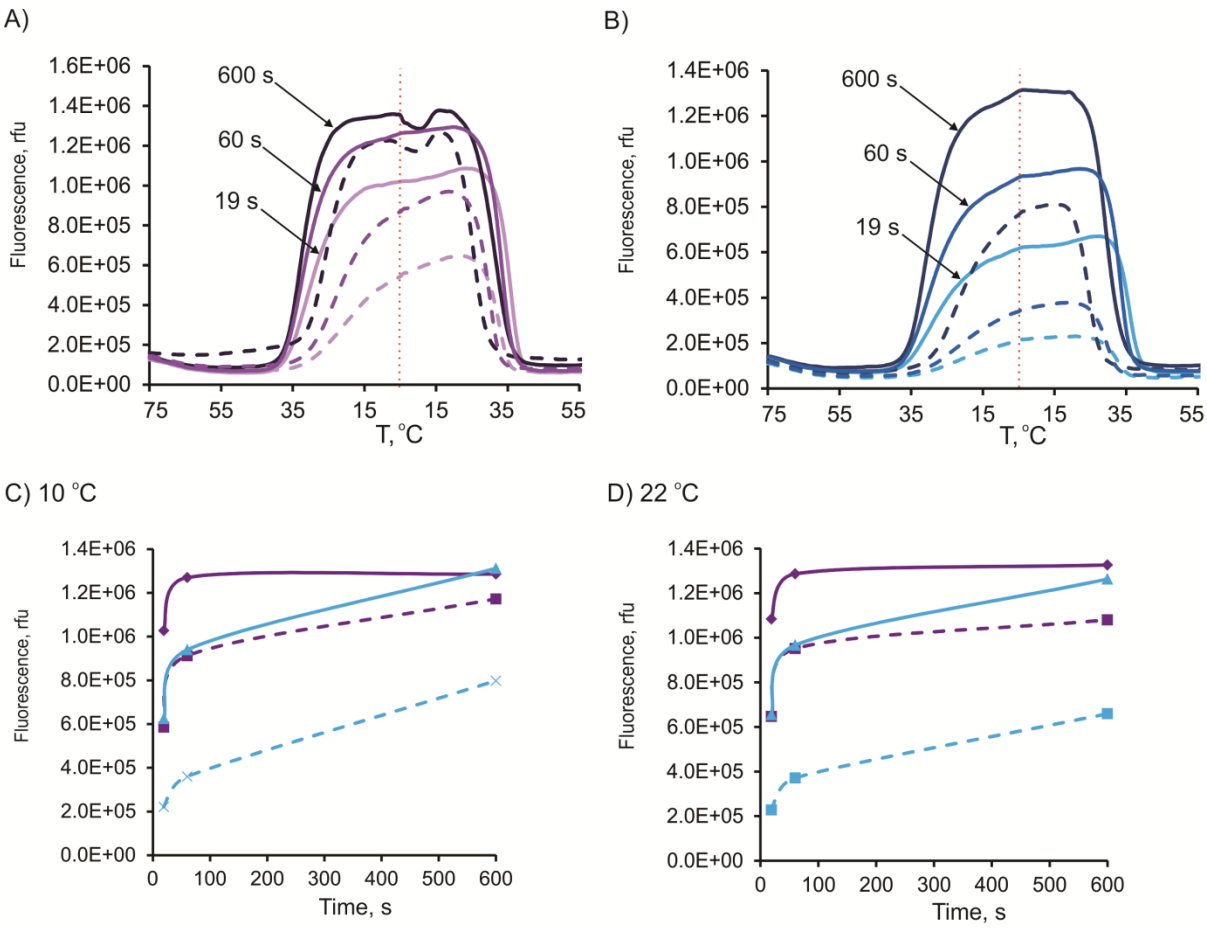

Figure 23. Kinetic responses of X_inh sensors containing stemless or stem-forming 9 nt-long m-analyte binding arms.

A)-B): Cooling-heating curves of stemless X_f_m-9_inh2 sensor (A) and stem-forming X_f_m9sl4_inh2 sensor (B) at different equilibration times: 19 s, 60 s, and 600 s respectively. The melting curves are color coded: light colors (19 s equilibration times), shade colors (60 s equilibration times), and dark colors (600 s equilibration times), respectively. Solid lines represent melting of fully matched complexes, while dashed lines melting of mismatched ones. Red dotted line shows the boundary between the cooling (left side) and the heating (right side) portion of the thermal profiles.
C)-D): Kinetic responses of the sensors at 10°C (C), and 22°C (D), respectively. Data were taken from the melting curves presented in panels A) and B). The assays' conditions were the same as in Figure 20.

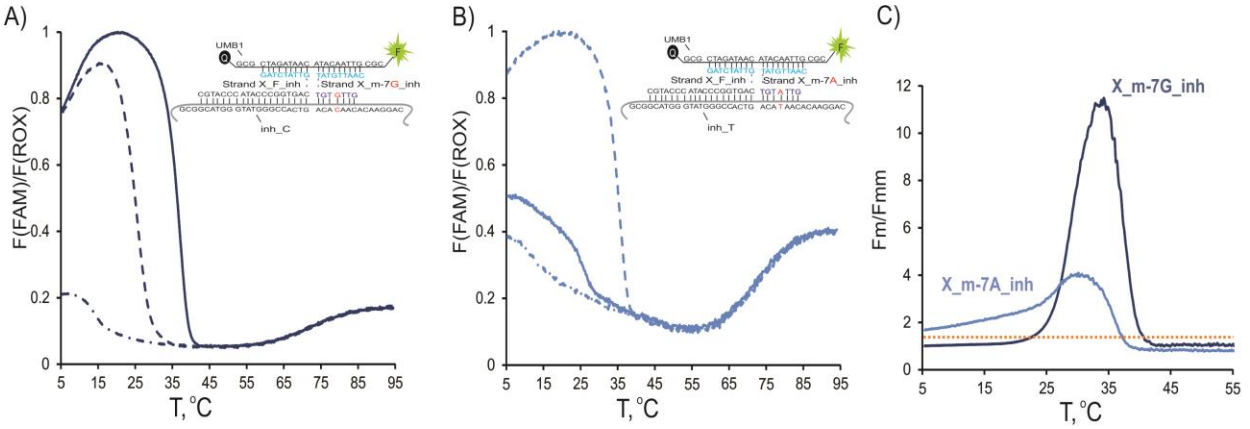

Figure 24. Fluorescence responses of X_inh sensor to a C -> T mutation.

A) Melting curves of X_F_m7G_inh sensor in complex with fully matched (solid line) and mismatched (dashed line) analytes. A schematic of the complex formed with the fully matched analyte is shown in the inserted figure.

B) Melting curves of X_F_m7A_inh sensor in complex with fully matched (dashed line) and mismatched (solid line) analytes. X_F_m7A_inh is fully complimentary to mutated analyte (C->T mutation).

C) Ratio of fluorescence responses of X sensors to the presence of corresponding fully matched (F_m) to mismatched (F_{mm}) analytes. The threshold F_m/F_{mm} ~ 1.5 is indicated by orange dotted line. The reaction mixtures contained 50 mM Tris-HCl (pH = 7.4), 100 mM $MgCl_2$, 0.1% Tween 20, 50 nM UMB1, 200 nM strand ***f***, and 120 nM strand ***m***.

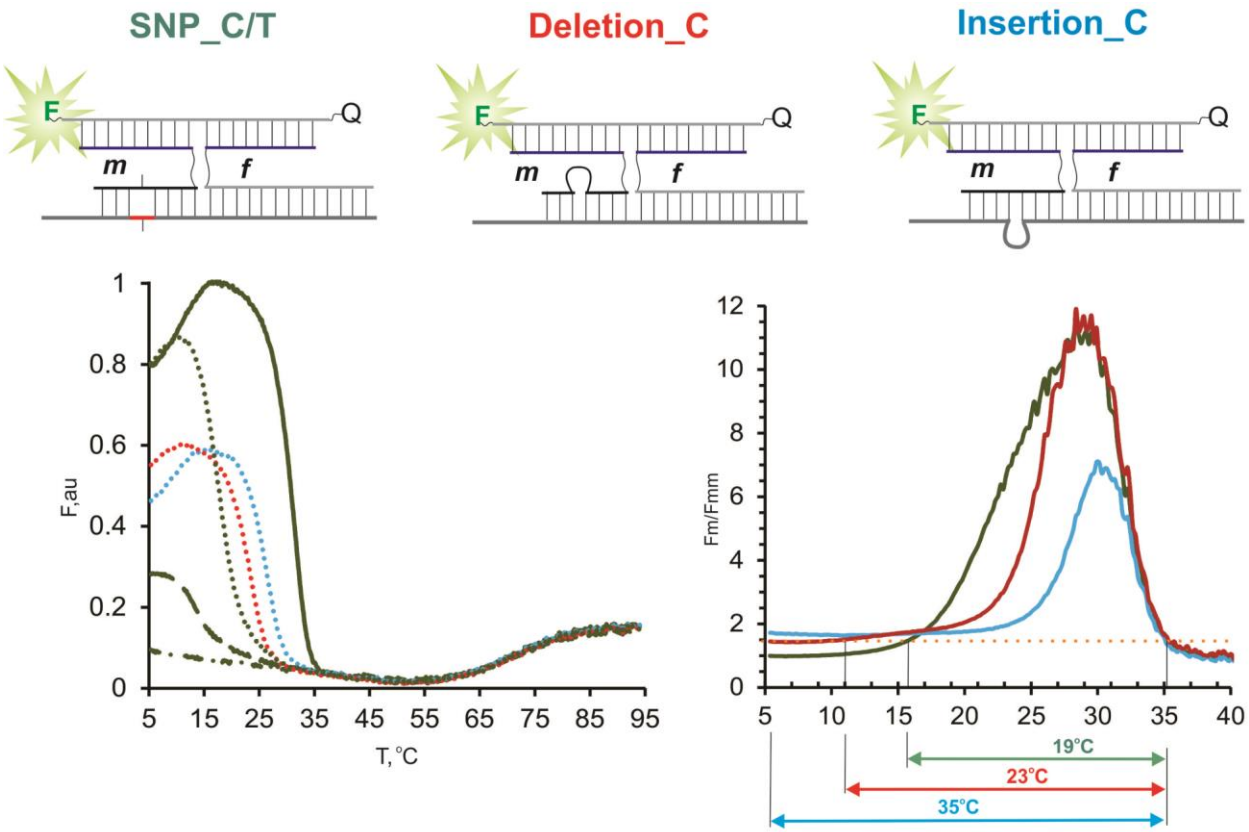

Figure 25. Recognition of different types of SNS by the X_inh sensor.

Top panels: X_inh sensor in complex with inh analyte containing different types of SNS as indicated. Bottom panels: Left: Melting curves of **X_inh** in complex with inh analyte containing one C->T mutation (green dotted lines), one C nt insertion (bleu dotted line), or one C nt deletion (red dotted lines). Melting of fully matched complex is represented by green solid line, of UMB alone by dash-dotted lines, and of X sensor (background fluorescence) by dashed line. Right: Sensor's performance in recognizing different SNS shown as the ratio of fluorescence responses of X sensors to the presence of fully matched (F_m) to mismatched (F_{mm}) analytes at different temperatures. $\Delta T_{1.5}$ intervals are indicated by color-coded arrows corresponding to each complex. The threshold F_m/F_{mm} ~ 1.5 is indicated by orange dotted line.
The reaction mixtures contained 50 mM Tris-HCl (pH = 7.4), 100 mM $MgCl_2$, 0.1% Tween 20, 50 nM UMB1, 200 nM strand ***f***, 120 nM strand ***m,*** and 100 nM analyte.

Table 3. Sequences of oligonucleotides used in the X_inh sensor study.

Name	Sequence	Purification
inh_T	5’-GCG GCA TGG GTA TGG GCC ACT GAC ATA ACA CAA GGA C	SD
inh_C	5’-GCG GCA TGG GTA TGG GCC ACT GAC ACA ACA CAA GGA C	SD
inh_T_Q1	5’-GCG GCA TGG GTA TGG GCC ACT GAC ATA ACA CAA GGA C/BHQ1/	HPLC
inh_C_Q1	5’-GCG GCA TGG GTA TGG GCC ACT GAC ACA ACA CAA GGAC/BHQ1/	HPLC
LP_inh	/FAM/-5’-TCT TGT GTT GTG TCA GTG A	HPLC
MB_inh	/FAM/-5’-CGCTC TTG TGT TGT GTC AGT GACG/BHQ1/	HPLC
UMB1	/FAM/-5’-CGC GTT AAC ATA CAA TAG ATCGCG/BHQ1/	HPLC
X_F_inh	5’-GAT CTA TTG/teg/CAG TGG CCC ATA CCC ATG C	SD
X_F_inh_short	5’-GAT CTA TTG-teg- CAG TGG CCC	SD
X_m-6 _inh	5’-TT G TGT/teg/TAT GTT AAC	SD
X_m6sl4_inh	5’-CACATT TT G TGT/teg/TAT GTT AAC	SD
X_mG-7 _inh	5’-GTT G TGT /teg/TAT GTT AAC	SD
X_mA-7_inh	5’-GTT A TGT /teg/TAT GTT AAC	SD
X_m-8 _inh	5’-TGT TGT GT /teg/TAT GTT AAC	SD
X_m-8sl2_inh	5’- ACATGT TGT GT/teg/T ATG TTA AC	SD
X_m-8sl4_inh	5’- CACATGT TGTGT /teg/TAT GTT AAC	SD
X_m-8sl5_inh	5’- CACAAATGT TGT GT/teg/T ATG TTA AC	SD
X_m-9_inh	5’-GTG TTG TGT/teg/TAT GTT AAC	SD
X_F_inh2	5’-GAT CTA TTG/teg/AG TGG CC CAT ACCC ATGC	SD
X_m-9_inh2	5'-TGT TGT GTC/teg/TAT GTT AAC	SD
X_m-9sl4_inh2	5'-CACAA TGT TGT GTC/teg/TAT GTT AAC	SD
X_del_inh	5’-GCG GCA TGG GTA TGG GCC ACT GAC AAA CAC AAG GAC	SD
X_ins_inh	5’-GCG GCA TGG GTA TGG GCC ACT GAC ACCAA CAC AAG GAC	SD
udg_G_2	5’- TCATCCA TGACA ACTTT GGTA T CGT GGA AGG ACTCAT GA	SD
udg_A_2	5’-TCATCCA TGACA ACTTT GGTA T CGT AGA AGG ACTCAT GA	SD
X_f3_udg	5’-GAT CTA TTG/teg/TAC CAA AGT TGT CAT GGA TGA	SD
X_m7_ udg	5’-TC C ACG A/teg/TAT GTT AA	SD

* teg- triethylene glycol linkers; SD, standard desalting; BHQ1, black hole quencher 1; FAM, fluorescein label; SNS sites are underlined; self-complementary regions of MB probes are in italic.

Table 4. Temperature characteristics for different probe-analyte complexes.

	Linear		MB		X sensor				X sensor S-L	
					m = 6		m = 8		m = 8; sl = 5	
Analytes	T_m	ΔT_m	T_m	ΔT_m	T_m	ΔT_m	T_m	ΔT_m	T_m	ΔT_m
inh_C	63.0	**7.0**	61.7	**8.2**	31.7	**13.9**	38.4	**7.2**	38.5	**8.9**
inh_T	56.0		53.5		17.8		31.2		29.6	

*Estimated precision in T_m is +/- 0.2 ^{o}C

Table 5. Temperature characteristics for X_inh sensor-analyte complexes containing long (X_F_inh) or short (X_F_inh_short) f-analyte binding arm.

	X_F_inh			X_F_inh_short		
	Tm inh_C	Tm inh_T	ΔT_m	T_m inh_C	T_m inh_T	ΔT_m
m-6	31.7	17.8	13.9	33	20.8	12.2
m-7	36.7	25.2	11.5	38	28.3	9.7
m-8	37.2	28.4	8.8	38.4	30.7	7.7
m-9	37.9	35.6	2.3	38.9	37.1	1.8

*Estimated precision in T_m is +/- 0.2 ^{o}C

Table 6. Temperature characteristics for X_inh probe-analyte complexes containing 8 nt stem-forming m-analyte binding arm.

	X_F_inh			X_F_inh_short		
	T_m inh_C	T_m inh_T	ΔT_m	T_m inh_C	T_m inh_T	ΔT_m
m-8	37.5	29.3	8.2	38.5	31.2	7.3
m-8sl3	37.6	29.7	7.9	38.6	31.4	7.2
m-8sl4	37.4	28.7	8.7	38.4	30.1	8.3
m-8sl5	37.3	28.3	9	38.5	29.6	8.9

*Estimated precision in T_m is +/- 0.2 ^oC

Table 7. Temperature characteristics for X_inh probe-analyte complexes containing 9 nt stem-forming m-analyte binding arm.

	X_F_inh2[1]				X_F_inh2[2]		
	Tm inh_C	Tm inh_T	ΔT_m	$\Delta T_{1.5}$	T_m inh_C	T_m inh_T	ΔT_m
m-9	36.7	33.6	3.1	10.2	37.4	33.7	3.7
m-9sl4	36.8	33.5	3.3	35	37.1	33.5	3.6

*Estimated precision in T_m is +/- 0.2 ^{o}C
[1]Concentration of adaptor strands: 120 nM ***f***, 60 nM ***m***
[2]Concentration of adaptor strands: 200 nM ***f***, 500 nM ***m***

Table 8. Temperature characteristics for probe-analyte complexes containing different SNS

	X_m6_F_inh2			MB	
Analytes	T_m	ΔT_m	$\Delta T_{1.5}$	T_m	ΔT_m
inh_C	31.7	**13.9**		61.7	**8.2**
inh_T	17.8		19	53.5	
inh_del	23.1	**8.6**	24	49.5	**12.2**
inh_ins	26.2	**5.5**	30	55.3	**6.4**

*Estimated precision in Tm is +/- 0.2 ^{o}C

CHAPTER 4: MB-BASED MULTICOMPONENT PROBES FOR RT PCR APPLICATIONS

Introduction

Nucleic acids analysis have wide applications in clinical diagnostic, ranging from genotyping of individuals [53-58], diagnostics of heredity diseases [59, 60] or disease-related genetic mutations [61-63]. In general, for most of these applications minute amount of target sequence is available, and so they mostly rely on polymerase chain reaction (PCR) to amplify the target. The basis of PCR is the ability of DNA polymerase to extend the primers hybridized to the complementary portion of corresponding DNA template. The process takes place in three steps: (1) denaturing at 95°C to fully separate the dsDNA template, (2) annealing at a temperature in general bellow 65°C such that to allow primers' hybridization to the DNA template and (3) extension at 72°C where polymerase has highest activity in catalyzing dNTPs addition to complementary DNA template. The three-step cycle can be repeated multiple times, and the amount of product obtained is proportional with the number of rounds. The amplified target products can then be analyzed by gel electrophoresis coupled with dye staining for visualization. However, this approach is time consuming, and can potentially induce contamination in the tested samples since it involves opening the reaction tubes and multiple handling.

A more desirable approach is real time PCR (rt PCR) in which amplification and detection of the samples are done in sealed tubes, so the risk of contamination is minimal, and in real time which is very beneficial in certain application [59, 64]. The

amplification process can be monitored using nonspecific like SYBR Green I and EVAGreen or specific detection probes like adjacent probes [65], Taq Man probes [66], Scorpion primers [67] and Molecular Beacons [2]. The dsDNA-binding dyes bind to all dsDNA sequences, and so primer-dimers and nonspecific amplification products cannot be distinguished [68]. In contrast, the probe-based approaches enable design of the probe sequence complementary to a target within the expected amplicon, so it is very unlikely for them to bind false amplicons or primer-dimers. These hybridization probes are fluorophore-labeled oligonucleotides. Taq Man probes are dual labeled randomly coiled oligonucleotide, and since the donor and acceptor molecules remain in close proximity (10-100 Å), the energy of the excited state of donor fluorophore is transferred to the quencher, thus the intensity of the fluorescence of the acceptor increases, while of the donor decreases. When probe hybridizes to the amplicon sequence it is chemically cleaved by 5'-3' exonuclease activity natural to a number of DNA polymerases including thermophilic Taq polymerase used in PCR. Fluorophore released in solution produces increase fluorescent signal. Another probe-based approach uses adjacent probes, when the donor fluorophore on one probe is brought in close proximity to the acceptor fluorophore on a second probe when both probes hybridize on the target. Upon excitation by a light source, the energy of the donor fluorophore is transfer to the acceptor, thus the fluorescence of the donor decreases, while the one of the acceptor increases. This is due to an increase in the efficiency of fluorescence resonance energy transfer (FRET)[69].

MB probes, on the other hand have a hairpin structure, bringing the two fluorophores in very close proximity, such that quenching is acquired by heat dissipation, the so called contact quenching mechanism [7, 70]. The main advantage of contact quenching is that all fluorophores are equally well quenched. MB probes have attracted particular attention as detection probes in rt PCR for two main reasons: (1) due to their hairpin structure, molecular beacons undergo a conformational change upon hybridization to a target, which improves selectivity of target recognition in comparison with linear probes; (2) they can be labeled in any color, which allowed them to be used successfully in multiplex detection assays [71, 72].

In a typical rt PCR experiment with MB as a detection probe, at 95°C the dsDNA and the stem of MB are melted apart, as a result MB probe is fluorescent. As temperature is lowered to allow primers to anneal to template ssDNA, the stem hybrid is also reformed which causes the MB probe to return to its low fluorescent state. In the following step, MB' loop hybridizes to the target, and fluorescence is restored. Each cycle is repeated, and as the target is amplified the fluorescence increases proportionally. In order to achieve the maximum of rt PCR assays, a set of parameters must be optimized independently: probe design, primer design and optimization of assay's conditions using a dye (i.e. EvaGreen) as internal control. In addition, melting temperature experiments can be helpful in further identification of rt PCR amplified products, particularly when both specific and non-specific products are expected [73].

In this chapter we used knowledge acquired in designing multicomponent MB-based probes (presented in Chapters 2 and 3), and applied X probe for the detection of

amplified products in rt PCR assays. First, an X_udg sensor was optimized to detect synthetic DNA target sequence in a wide temperature range (from 5°C to ~40°C) in a commercial available PCR buffer. Further, an X_inh sensor with a similar design as X_udg was modified to recognize the near linear C_inh analyte. Lastly, the X_inh sensor was tested in rt PCR assays. The results presented here suggest that X sensors might be adopted for rt PCR format.

Materials and Methods

Reagents

DNAse/protease-free water was purchased from Fisher Scientific Inc. (Pittsburg, PA) and used for stock and working solutions of oligonucleotides and probes. Phusion® High-Fidelity DNA Polymerase, Phusion® HF buffer, $MgCl_2$, 50 mM and dNTPs were purchased from New England Biolabs (Ipswich, MA). UMB1 was custom-made by TriLink Biotechnologies, Inc. (San Diego, CA). All other oligonucleotides including forward and reverse primers (sequences listed in Table 1) were obtained from Integrated DNA Technologies, Inc. (Coraville, IA). In order to restrict the extension of adaptor strands during the PCR cycles, their 3'-ends were blocked with phosphate groups. The fragment of inhA promoter region from Mycobacterium Tuberculosis CDC 1551 was a generous gift from Dr. Rohde (UCF). The Optical 96-Well plates (EnduraPlate™), optical adhesive film (MicroAmp®), 8-tube strip with optical caps and ROX reference dye were purchased from Life Technologies (Grand Island, NY). The concentrations of oligonucleotides in stock solutions were determined from Lambert

Beer equation. Absorptions of these solutions at 260 nm and RT were measured with a Perkin-Elmer Lambda 35 UV/Vis spectrometer (San Jose, CA), while the corresponding extinction coefficients were determined by using OligoAnalyzer 3.1 software (Integrated DNA Technologies, Inc.). Working solutions of adequate concentrations were prepared for all oligonucleotides and probes and stored to -20°C until use.

Real-time PCR Experiments

The dsDNA inhA fragment of Mtb CDC 1551 containing forward inh_F1 primer 5'-TTCCTGGCTTCCGAGGAT-3', reverse inh_R1 primer
5'- AGTCGGTGATGATTCCGCTA-3' and the 37-nucleotide target sequence was amplified in real-time PCR. The rt PCR assays were carried out using a real time QuantStudio™ 6 Flex System from Life Technologies (Grand Island, NY). The reaction mixture (25 ul) contained 200 uM dNTP mix, 500 nM of inh_F1 primer and 50 nM of inh_R1 primer, 0.5 ul of 0.02u/ul Phusion® High-Fidelity DNA Polymerase, 50 nM UMB1, 250 nM m9/10_inh, 500 nM f10_inh and DNA template (0.3 ng/ul) mixed in Phusion® HF buffer supplemented with $MgCl_2$ to a total concentration of 2 mM. Similar mixtures were prepared for EVA Green dye: each mixture contained all components mentioned above, but the X sensor's components which were substituted with EVA Green (100 nM). The samples were loaded into 8-strip tubes with optical caps (20 µl per tube), vortexed and then spun at 660 rcf for 20 sec. Care was taken such that to avoid the formation of air bubbles in the tubes. The experiments were repeated at least twice and analyzed with the QS6 software v1. The PCR cycles were: 98°C, 3 min (the

first cycle), followed by 98°C - 19 sec, 67°C – 20 sec, 72°C - 20 sec (35-40 cycles), and the final extension step at 72°C – 30 sec. Additional 2 steps at 20°C were used for reading fluorescence of samples containing the X sensor: the first step for 5 min and the second for 20 sec. In each PCR experiment a set of 2 samples - no template control (NTC) and sample containing the template DNA were amplified in the presence of EVA Green, and served as controls for PCR conditions. Formation of expected PCR products was verified by agarose gel electrophoresis and melting curve analysis.

Melting Curves Recordings

Melting experiments were performed in duplicates on the SYBR detection channel on the same PCR machine. For optimization of the X_sensor, the reactions contained in general 50 nM UMB1, 50 nM ROX passive dye and 100 nM synthetic analytes (matched or mismatched), but different combinations of adaptor strands with various concentrations (see figure legends for each particular assay). The samples were mixed in the above mentioned PCR buffer without dNTP, primers, Phusion® High-Fidelity DNA polymerase and Mtb CDC 1551 template. Melting temperatures were determined directly from the QS software as the first derivative maxima. The samples were loaded into a 96-well plate (20 µl per well), which was sealed with an optical adhesive cover, vortexed and then spun at 660 rcf for 20 sec. Care was taken such that to avoid the formation of air bubbles in the wells. In a typical melting curve experiment, the solutions were fast heated (1.6°C/sec) to 95°C, melted at 95°C for 1 min, and fast cooled (1.6°C/sec) to 5°C. After 30 min of equilibration at 5°C, the temperature was

raised back to 95°C (0.05°C/sec), while fluorescence intensity was recorded continuously about every 0.2°C. Melting of amplified products was done following the same protocol.

Results and Discussion

X sensors can significantly improve SNS detection in rt PCR due to the broad temperature interval they can differentiate SNS. Modification that needs to be done is blocking of the 3'-ends by e.g. a phosphate group. In addition, since the hybrids formed by X sensors melt at a temperature much lower than the annealing temperature (T_a) of potential primers additional steps are required for fluorescence reading at each PCR cycle. This increases the assay's time, but also the chance of nonspecific PCR products formation. Nonetheless, our sensors have the advantage of being able to discriminate match from mismatch analytes in a wide range of temperatures, and so they have a great potential for use in multiplex detection of SNS.

The focus of this part of research was to design and optimize an X sensor capable of rt PCR detection of a DNA fragment responsible for *Mtb* resistance to antibiotic isoniazid (**Inh**) in a commercial available PCR buffer. A 37-nt target sequence **5'-GCG GCA TGG GTA TGG GCC ACT GAC ACA ACA CAA GGA C-3'** of inhA promoter region from *Mtb* CDC 1551 with a total of 151 bp was chosen as shown below:

5'-TTCCTGGCTTCCGAGGATGCGAGCTATATCTCCGGTGCGGTCATCCCGGTCG

ACG**GCGGCATGGGTATGGGCCACTGACACAACACAAGGAC**GCACATGACAGGA

CTGCTGGACGGCAAACGGATTCTGGTTAGCGGAATCATCACCGACT-3'

(the primers are underlined, the target sequence is highlighted in bold and the position of mutation is both underlined and highlighted).

The optimal X sensor for use in rt PCR assays would have high discrimination range (F_m/F_{mm}) and high melting temperatures in a buffer containing optimal Mg^{2+} ions concentration. As shown in chapters 2 and 3, in a buffer containing high concentration of Mg^{2+} ions (100 mM), the widest discrimination range was obtained for sensors with the shortest m-analyte binding, while the highest T_m by the sensors with the longest m-analyte binding arms. The performance of several X_udg sensors mixed in Phusion® HF buffer containing 1.5 mM Mg^{2+} is presented in Figure 26. In our attempt to increase T_m, we designed X_udg sensors with longer f and m-MB binding arms. Figure 26A demonstrates the discrimination range of different X sensor dependence on the length of MB-binding arm of strand f. The more nt are added (f9 to f12) the further the maximum of each curve is shifted towards higher T values (see also Table 11 for T_m values), but at the expense of losing in differentiation range i.e. from 35°C – f9, 27°C – f10, 13°C – f11, to 10°C – f12 if F_m/F_{mm} threshold is set at 1.5. Based on these results we selected strand f9 for further experiments due to the broadest differentiation range of 5-35°C. Figure 26B demonstrates the results of optimization of analyte binding arm of m strand. In this case the same f9 strand was used. As expected, the longer the m-analyte binding arm the wider the discrimination range and so X sensor that used m strand with-10 nt analyte binding arm (m10) was capable of discriminating mismatched from matched analytes in all temperature range 5-36°C. Since none of the sensors gave both the highest T_m and the widest discrimination range, the compromise chosen was a

sensor with an intermediate performance. As a result, further optimization assays were performed with the X_udg sensor containing 10-nt long m and f-MB binding arms, and 9-nt long m-analyte binding arm.

It has been shown that Mg^{2+} concentration affects PCR specificity and efficiency: concentrations of 1-1.5 mM resulted in nonspecific amplification, most likely because primers cannot bind to DNA template in the absence of sufficient Mg^{2+} ions, while concentrations of 2-2.5 mM produced specific products [74]. On the other hand, 4WJ-containing multicomponent strand associates are stabilized by Mg^{2+} ions [75], which shield negative charges of repealing negatively charged DNA strands. In our previous experiments, therefore, we use 50-100 mM Mg^{2+}, which is incompatible with PCR conditions. It was important to verify that X sensor can be tailored to operate under Mg^{2+} conditions of rt PCR. Thus, we tested the performance of X_udg sensor in recognizing of matched and mismatched analytes, in Phusion® HF buffer supplemented with Mg^{2+} ions to a total concentration of 1.5 mM, 2 mM, 4 mM, 8 mM and 10 mM, respectively (Figure 27). The maxima of F_m/F_{mm} curves shifted to higher temperature, while the base of the curves flattened with increasing the concentration of Mg^{2+} ions. As shown in Figure 27, the maximum temperature discrimination range is obtained for samples prepared in Phusion® HF buffer containing 2 mM Mg^{2+}. This Mg^{2+} concentration is near optimal for PCR. Therefore, in contrast to our expectations relatively low Mg^{2+} concentration of PCR buffers is unlikely to create an obstacle in application of X sensors in rt PCR.

The effect of adaptor strand concentrations on sensor's performance was also tested. By increasing the adaptor strand concentration we aimed to shift the equilibrium towards complex formation, thus to increase the fluorescent signal. Different concentrations of m and f strands were chosen: 120/240 nM, 250/500 nM, 500/1000 nM, respectively. (Figure 28B) The concentrations of UMB1 and targets (inh_C and inh_T) were kept the same in these assays - 50 nM and 100 nM, respectively. Although a slight increase in T_m of hybrids (Δ~1.5°C) was observed with increasing the concentration of both staples, F_m/F_{mm} doesn't show a clear trend, the intermediate m/f concentration (250/500 nM) showing the broadest discrimination range (~40°C). Melting curves of this sensor in complex with either matched (WT) or mismatched (SNP) analytes are shown in panel A, while corresponding melting temperatures (T_m) is presented in Table 11. Thus, increasing adaptor strand concentrations to 250/500 nM seemed to slightly help to increase fluorescent signal in the low temperature regime particularly, but higher concentration didn't. At the same time, the increase in T_m was insignificant for complexes with high staple concentrations, and so we decided to use 250/500 nM m/f in further experiments.

This latest design was applied to the X_inh sensor, which consisted of MB, two adaptor strands ***m*** and ***f,*** each with 10-nt long MB binding arms, 18-nt f-analyte binding arm, and 10-nt long m-analyte binding arm, respectively. (Figure 29B, upper panel). The 3'-ends of the adaptor strands were phosphorylated, to block the 3' OH groups of the strands and prevent them from serving as promoters of DNA polymerization (Table 11). The fluorescence response of this sensor to matched and mismatched analytes

was tested in melting experiments initially (Figure 29B, lower panel). This sensor had high T_m (Table 12), and high background fluorescence (Figure 29B, lower panel). Lowering UMB1 concentration to 20 nM, lower the background fluorescence, but at the same time decreased significant the signal of matched hybrid, which is not desirable in rt PCR assays particularly in complex environments like living cells due to potential false-negative results [76]. The X_inh sensor with 9-nt long MB-binding arms showed a better performance at low temperature (Figure 29A), but lower melting temperatures than X_inhp. (Table 11) Thus, although the X_inhp sensor with 10-nt long MB binding arms showed poorer discrimination at low temperature than the X_inh sensor with 9-nt long MB-binding arms, we decided to pursue in our rt PCR trials, at least in preliminary format, with the first since there is still a 20°C-window with good discrimination (Figure 29C).

It has been shown that when using equal concentrations of forward and reverse primers (symmetric PCR), in later cycles, the amplified strands reanneal before the probe can bind to generate fluorescence. This might be an issue particularly if resulting products are meant to be investigated by melt-curve analysis [73]. The problem can be overcome by using different primer concentrations (asymmetric PCR) [77, 78]. In our rt PCR assays we used higher concentration of forward primer which resulted in more of the strand complementary to the X_probe, thus allowing more fluorescence to be generated. A ratio of 10 to 1 forward: reverse primer was used.

Figure 30 shows the results of PCR amplification monitored with either X_inhp sensor (A) or EVA Green (B) and the identification of corresponding products based on

melting-curve analysis (C) or agarose gel electrophoresis analysis (D). Samples containing EVA Green were prepared and used as internal controls for rt PCR assays. It should be noted that a total of 40 cycles were needed to detect the amplified products, but in Figure 30 panels A and B are shown only the last 20 cycles. In order to monitor amplification with X_inh sensor two low temperature stages were added to the PCR sequence, steps needed for sample equilibration and fluorescence reading. In this case, beside the amplified target products, nonspecific amplified products resulted also in both non-template and template containing samples for both X_inhp and Eva Green PCR amplifications (panel A). This is most evident in the amplification plot of non-template samples for X_inhp (panel A), but also in the melting curves (panel C). It has been shown that the cycling conditions, particularly temperature and holding time affect the sensitivity and selectivity of rt PCR assay [79]. Moreover, protocols with reduced temperature (i.e. 25°C), especially during fluorescence reading resulted in nonspecific product formation [80]. However, the X sensor needed longer equilibration times than MB probes did for example (see chapter 3). In addition, according to manufacturer's specifications, the QS6 rt PCR machine measures fluorescence at the beginning of set hold step over a period of ~30 s. This time might not be sufficient for equilibration of hybridization reaction. Furthermore, the hybrids formed with X sensors have lower melting temperatures (T_m = 38.9°C) than the primers (T_m = 65°C), so two additional low temperature (20°C) holding steps were necessary to be added to the PCR protocol, the first to allow equilibration of the samples (5 min), and the second for fluorescence reading (20 sec).

First derivative of melting curves of amplified products showed more than one peak, which reflects a complex melting behavior and the presence of non-specific products. However, the peak at T_m = 38.3°C most likely corresponded to the target amplified product (Figure 30C), since T_m of the complex with synthetic analyte was 38.9°C. Agarose gel electrophoresis of X_inhp sensor products showed multiple bands for products resulted from PCR sequence with low temperature steps (Figure 30D, left side of the ladder). The band seen at ~150 bp (pointed by the blue arrow) is most likely the target ssDNA. It appears weak, since a low amount of ssDNA is expected to result (asymmetric PCR). The upper bands present in both no template and template-containing samples corresponded to non-specific products. EVA Green and X_inhp rt PCR amplification products resulted in the PCR conditions without the two low temperature steps, gave mainly 2 bands: one at ~150 bp and the other at ~220 bp and they correspond to target ssDNA and target dsDNA, respectively (Figure 30D, right side of the ladder).

Conclusion

In summary, a multicomponent MB-based sensor was optimized for recognition of an analyte with complex secondary structures in a PCR commercial available buffer containing 2 mM Mg^{2+} ions concentration. The design of the sensor was applied to an X_inh sensor capable to recognize a DNA fragment responsible for *Mtb* resistance to antibiotic isoniazid. This sensor was capable of monitoring in real time the PCR amplification of target products, but its performance was poor since nonspecific

amplification products also resulted. These products most likely formed during the low temperature stages of the PCR cycles, which were necessary for thermal equilibration and fluorescence acquisition. The results presented in this chapter are important steps in real time detection of PCR products with X sensors.

Figures and Tables

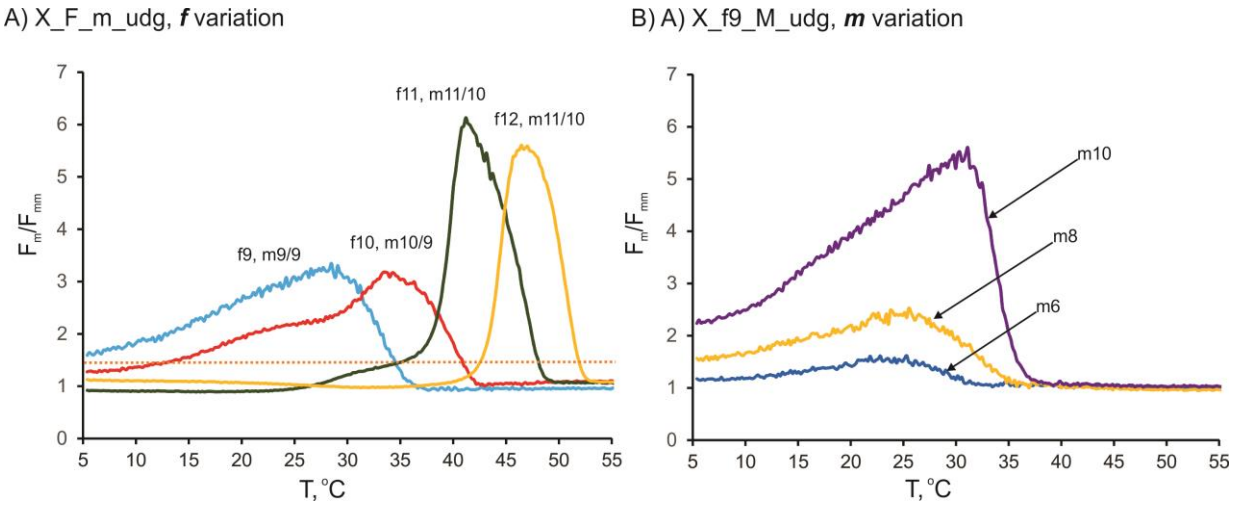

Figure 26. Differentiation range dependence on the length of binding arms for X_udg sensors.

The ratio of fluorescence produced by each X_udg probe in the presence of fully matched (F_m) to that of mismatched (F_{mm}) is shown as a function of temperature. The threshold value is indicated by yellow dotted line.

A) Dependency on the length of f-MB binding arm: 1 uM fx/y (x=9, 10, y=9, 10, 11, 12)_udg and 0.5 uM m9/ y (y= 6, 8, 10)_udg were mixed in Phusion® HF buffer containing 1.5 mM $MgCl_2$; x = length of analyte binding arm, y = length of MB-binding arm.

B) Dependency on the length of m-analyte binding arm: f-analyte binding arm was 9-nt long. 200 nM f9_udg and 200 nM m9/ x (x= 6, 8, 10)_udg were mixed in Phusion® HF buffer 1.5 mM $MgCl_2$.

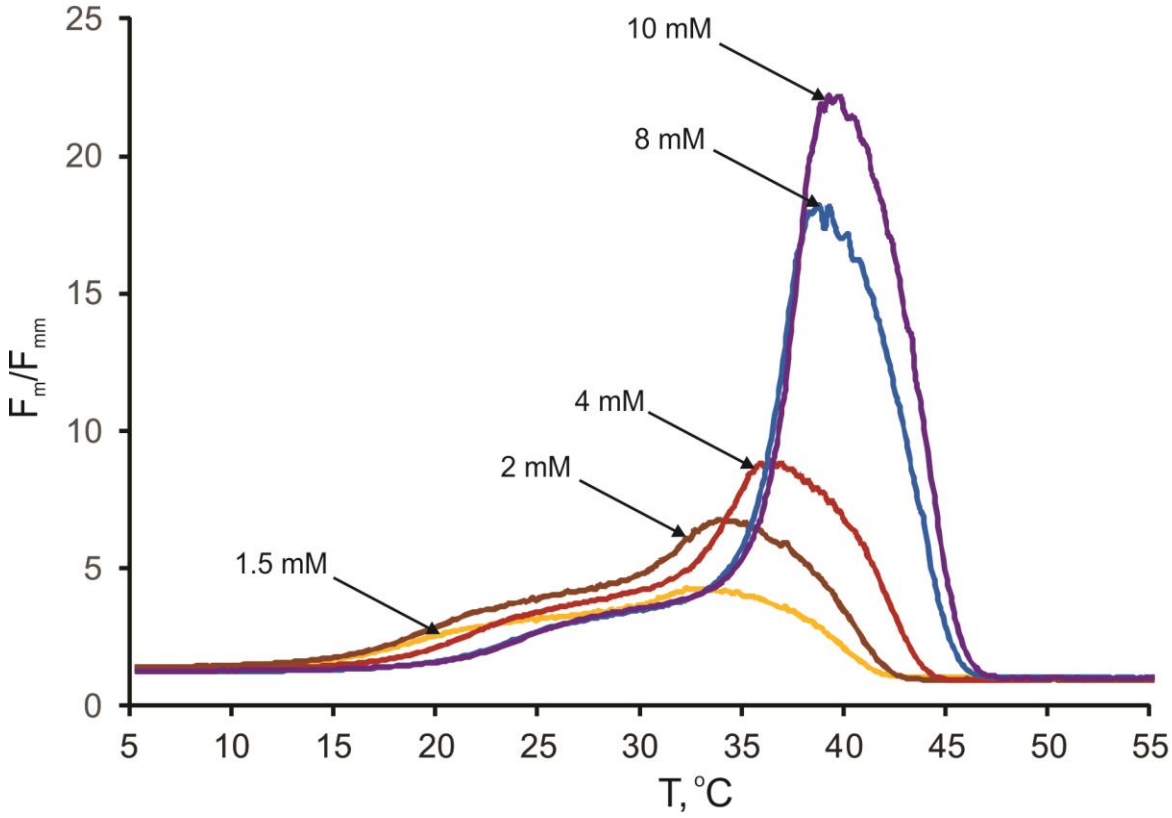

Figure 27. Differentiation range dependence on Mg^{2+} concentration in Phusion® HF buffer for X_udg sensors.

Assays' conditions: Adaptor strands, MB and analytes' concentrations were kept the same in all experiments - 1 uM f10_udg and 0.5 nM X_m10/9_udg, 50 nM UMB1, and 100 nM of each analyte (udg_G_2 and udg_A_2).

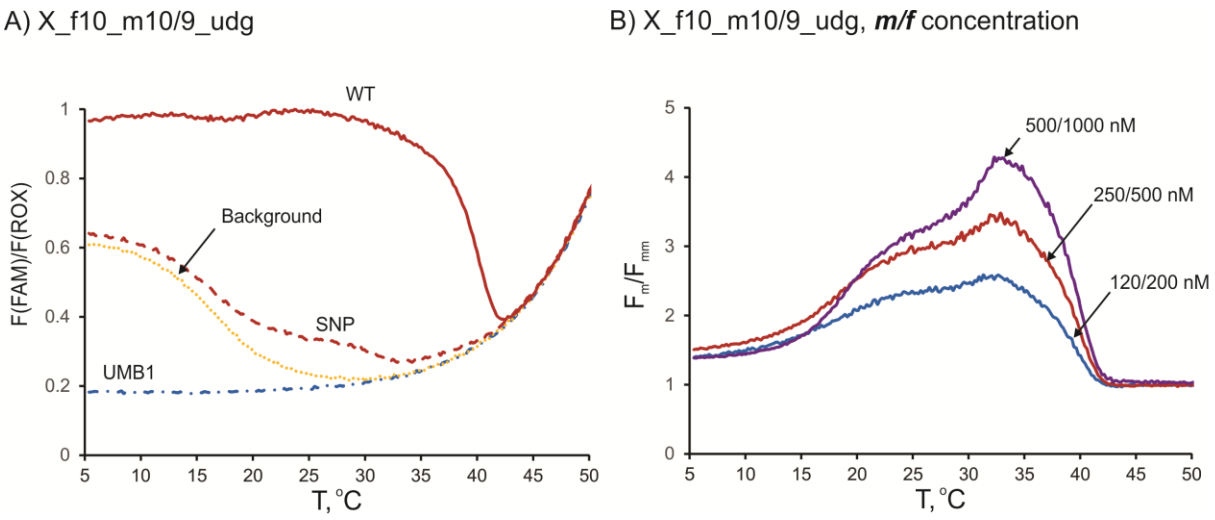

Figure 28. Performance of X_udg sensor in Phusion® HF buffer 2 mM Mg^{2+}.

A) Fluorescence response of the sensor to the presence of fully matched (solid line) and mismatched (dashed line) DNA analytes. Assay's conditions: 500 nM X_f10_udg, 250 nM X_m10/9_udg, 50 nM UMB1 and 100 nM analyte.

B) Fluorescence dependence on different adaptor strand concentrations. The ratios represent m10/9_udg strand to f10/10 strand concentrations.

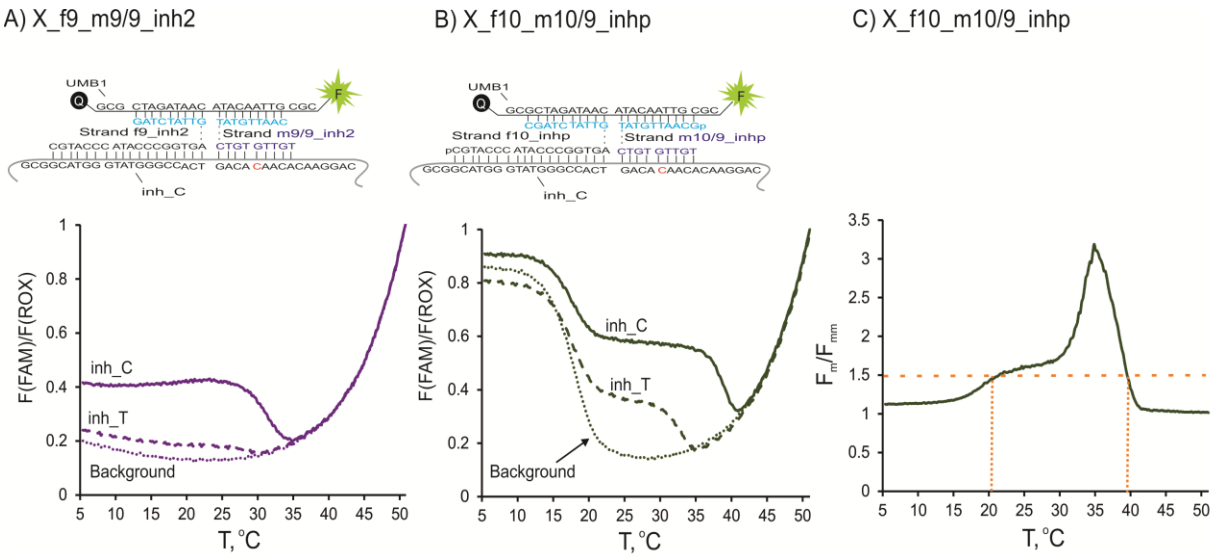

Figure 29. Performance of X_inh sensors for recognition of inh analytes in Phusion® HF buffer 2 mM Mg^{2+}.

Fluorescence responses of X_f9_m9/9_inh (A), X_f10_m10/9_inhp (B) to the presence of fully matched (solid lines) and mismatched (dashed lines) DNA analytes. Discrimination range for X_f10_m10/9_inhp (C) Assay's conditions: 50 nM UMB1, 500 nM ***f***, 250 nM ***m***, 100 nM analyte.

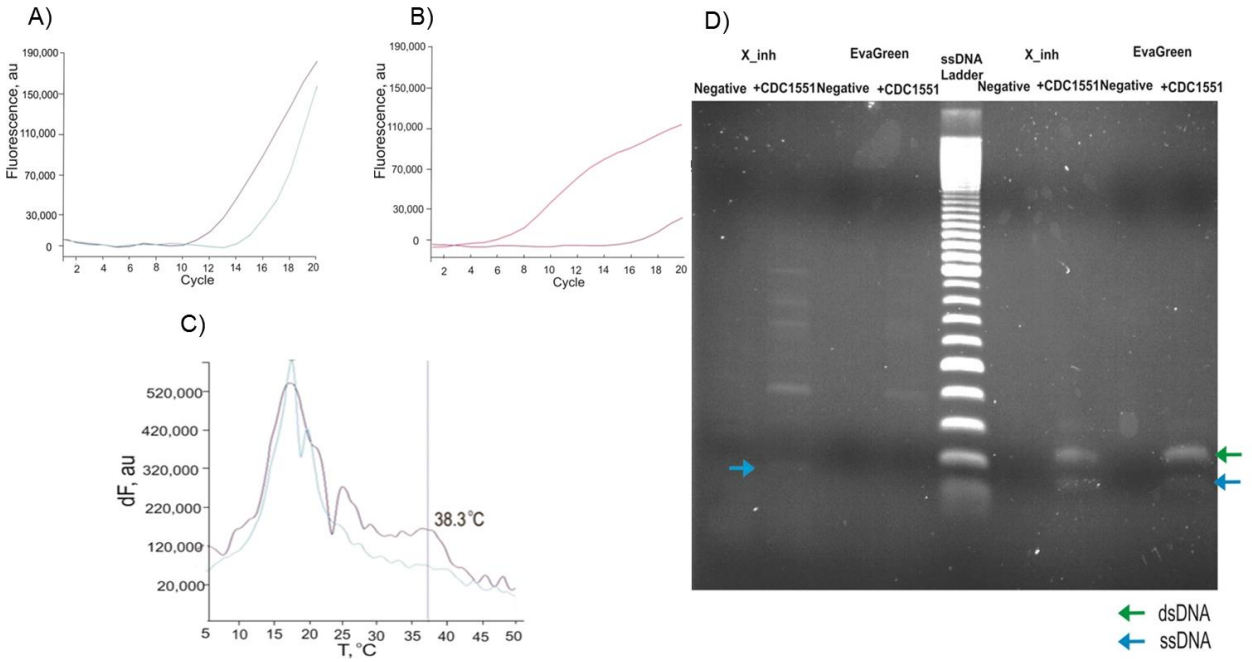

Figure 30. Performance of X_inh sensor in detection of rt PCR amplified products.

A) Amplification plot shown as Fluorescence against cycle number and monitor with X_inh sensor.
B) Amplification plot shown as Fluorescence against cycle number and monitor with EVA Green dye.
C) First derivative of melting curves of amplified products detected by X_inh sensor. Melting temperature of specific amplified product is indicated on the graph.
D) 2% Agarose gel electrophoresis of products following real time X_inh, or EVA Green PCR amplification, respectively. The middle lane is the 100 bp ladder, with 100 bp at the bottom. Note the band at ~150 bp (blue arrow), which is likely the target amplification product. On the left of the ladder were loaded products resulted from long PCR sequence (2 low temperature stages added), and on the right of the ladder products of standard PCR sequence, respectively. The 2% agarose gel was run for 50 min at 100 V in TBE 1X buffer. The gel was stained with ethidium bromide for visualization under UV light.

Table 9. Sequences of oligonucleotides used in the rt PCR amplification study.

Name	Sequence	Purification
udg_G_2	5’- TCATCCA TGACA ACTTT GGTA T CGT GGA AGG ACTCAT GA	SD
udg_A_2	5’-TCATCCA TGACA ACTTT GGTA T CGT AGA AGG ACTCAT GA	SD
X_f9_udg	5’-GAT CTA TTG/teg/TAC CAA AGT TGT CAT GGA TGA	SD
X_f10_udg	5’-C GAT CTA TTG - teg -TAC CAA AGT TGT CAT GGA TGA	SD
X_f11_udg	5'-GC GAT CTA TTG - teg -TAC CAA AGT TGT CAT GGA TGA	SD
X_f12_udg	5'-CGC GAT CTA TTG - teg -TAC CAA AGT TGT CAT GGA TGA	SD
X_m6/9_udg	5'-CCA CGA - teg -TAT GTT AAC	SD
X_m8/9_udg	5'-TT CCA CGA - teg -TAT GTT AAC	SD
X_m9/9_udg	5'-CTTC C ACG A - teg -TAT GTT AAC	SD
X_m10/9_udg	5'-CCTTC C ACG A - teg -TAT GTT AAC	SD
X_m9/10_udg	5'-CTTC C ACG A - teg -TAT GTT AAC G	SD
X_m10/11_udg	5'-CCT TCC ACG A - teg -TAT GTT AAC GC	SD
X_m10/12_udg	5'-CCTTC C ACG A - teg -TAT GTT AAC GCG	SD
inh_T	5’-GCG GCA TGG GTA TGG GCC ACT GAC ATA ACA CAA GGA C	SD
inh_C	5’-GCG GCA TGG GTA TGG GCC ACT GAC ACA ACA CAA GGA C	SD
MB_inh	/FAM/-5’-cgctc TTG TGT TGT GTC AGT gagcg/BHQ1/	HPLC
UMB1	/FAM/-5’-CGC GTT AAC ATA CAA TAG ATCGCG/BHQ1/	HPLC
X_F_inh2	5’-GAT CTA TTG/teg/AG TGG CC CAT ACCC ATGC	SD
X_m-9_inh2	5'-TGT TGT GTC/teg/TAT GTT AAC	SD
X_F_inhp	5’-CGAT CTA TTG/teg/AG TGG CC CAT ACCC ATGCp	SD
X_m9/10_inhp	5'-TGT TGT GTC/teg/TAT GTT AACGp	SD

* teg- triethylene glycol linkers; SD, standard desalting; BHQ1, black hole quencher 1; FAM, fluorescein label; SNS sites are underlined; p, phosphorylated staple; self-complementary regions of MB probes are in italic.

Table 10. Melting temperature dependence on $MgCl_2$ concentration for X_udg sensor-analyte complexes.

	100 mM $MgCl_2$			2 mM $MgCl_2$		
	Tm udg_G	Tm udg_A	ΔT_m	T_m udg_G	T_m udg_A	ΔT_m
m9/9_ f9	38.7	34.4	4.3	33.3	26	7.3
m9/10_f10	45.6	38.7	6.9	40.1	31.5	8.6
m10/11_f11	52.9	45.8	7.1	46.9	38.7	8.2
m10/12_f12	57.1	50.6	6.5	50.7	43.3	7.4

*Estimated precision in T_m is 0.2^{o}C; C buffer left, phusion buffer right. Conditions: 50 nM UMB1, 120 nM ***m***, 200 nM ***f***, 100 nM analyte

Table 11. Melting temperatures of probe-synthetic analyte complexes and PCR amplified products

	X_inhp		MB_inh	
Analytes	T_m	ΔT_m	T_m	ΔT_m
inh_C	38.9	**6.1**	57.2	**6.9**
inh_T	32.8		50.3	
inh_a	**38.3**			

*Estimated precision in T_m is 0.2 ^{o}C
a: amplified product.

REFERENCES

1. Kolpashchikov, D.M., *An Elegant Biosensor Molecular Beacon Probe: Challenges and Recent Solutions.* Scientifica, 2012: p. 1-17.

2. S. Tyagi, F.K., *Molecular Beacons: Probes that Fluoresce upon Hybridization.* Nature Biotechnology, 1996. **14**: p. 303-308.

3. G. Bonnet, S.T., A. Libchaber, F. R. Kramer, *Thermodynamic basis of the enhanced specificity of structured DNA probes.* Proc. Natl. Acad. Sci. USA, 1999. **96**: p. 6171–6176.

4. Kolpashchikov, D.M., *A Binary DNA Probe for Highly Specific Nucleic Acid Recognition.* J. Am. Chem. Soc. , 2006. **128**: p. 10625-10628

5. Y. V. Gerasimova, A.H., J. Ballantyne, D. M. Kolpashchikov, *A Single Molecular Beacon Probe Is Sufficient for the Analysis of Multiple Nucleic Acid Sequences.* ChemBioChem, 2010. **11**: p. 1762-1768.

6. Y. V. Gerasimova, D.M.K., *Detection of bacterial 16S rRNA using a molecular beacon-based X sensor.* Biosens. Bioelectron., 2013. **41**: p. 386-390.

7. E. Navarro, G.S.-H., M.J. Castañoa, J. Solera, *Real-time PCR detection chemistry.* Clinica Chimica Acta 2015. **439**: p. 231-250.

8. Broude, N.E., *Stem-loop oligonucleotides: a robust tool for molecular biology and biotechnology.* Trends in Biotechnology, 2002. **20**: p. 249-.

9. C.W. Lam, K.C.L., S.F. Tong *Microarrays for personalized genomic medicine.* Adv. Clin. Chem., 2010. **52**: p. 1-18.

10. A. P. Silverman, E.T.K., *Oligonucleotide probes for RNA-targeted fluorescence in situ hybridization.* Advances in Clinical Chemistry, 2007. **43**: p. 79-115.

11. H. J. Tanke, R.W.D., T. Raap, *FISH and immunocytochemistry: towards visualizing single target molecules in living cells.* Curr Opin Biotechnol, 2005. **16**: p. 49-54.

12. M. M. Mhlanga, L.M., *Using Molecular Beacons to Detect Single-Nucleotide Polymorphisms with Real-Time PCR.* Methods, 2001. **25**: p. 463-471.

13. Y. Xiao, K.J.I.P., X. Lou, R. J. White, J. Qian, K. W. Plaxco, H. T. Soh, *Fluorescence Detection of Single Nucleotide Polymorphisms via a Single, Self-*

Complementary, Triple-stem DNA Probe. Angew Chem Int Ed Engl. , 2009. **48**: p. 4354–4358.

14. C. Nguyen, J.G., Y. V. Gerasimova, D. M. Kolpashchikov, *Molecular beacon-based tricomponent probe for SNP analysis in folded nucleic acids.* Chemistry, 2011. **17**: p. 13052–13058.

15. A.Tsourkas, M.A.B., S. D. Rose, G. Bao, *Hybridization kinetics and thermodynamics of molecular beacons.* Nucleic Acids Research, 2003. **31**: p. 1319-1330.

16. J. Guo, J.J., N. J. Turro, *Fluorescent hybridization probes for nucleic acid detection.* Anal Bioanal Chem 2012. **402**: p. 3115–3125.

17. Kolpashchikov, D.M., *Binary Probes for Nucleic Acid Analysis.* Chem. Rev. , 2010. **110**: p. 4709–4723.

18. Wetmur, J.G., *DNA Probes: Applications of the Principles of Nucleic Acid Hybridization.* Critical Reviews in Biochemistry and Molecular Biology, 1991. **26**: p. 227-259.

19. P. M. Holland, R.D.A., R. Watson, D. H. Gelfand, *Detection of specific polymerase chain reaction product by utilizing the 5' -* 3' exonuclease activity of Thermus aquaticus DNA polymerase.* Proc. Natl. Acad. Sci. USA, 1991. **88**( ): p. 7276-7280.

20. E. Meaburn, L.M.B., L. C. Schalkwyk, R. Plomin, *Genotyping pooled DNA using 100K SNP microarrays: a step towards genomewide association scans.* Nucleic Acids Research, 2006. **34**.

21. I. V. Kutyavin, I.A.A., A. Mills, V. V. Gorn, E. A. Lukhatnov, E. S. Belousov, M. J. Singer, D. K. Walburger, S. G. Lokhov, A. A. Gall, R. Dempcy, M. W. Reed, R. B. Meyer, J. Hedgpeth, *3'-Minor groove binder-DNA probes increase sequence specificity at PCR extension temperatures.* Nucleic Acids Research, 2000. **28**: p. 655-661.

22. Tyagi, S., *Imaging intracellular RNA distribution and dynamics in living cells.* Nature Methods, 2009. **6**: p. 331-338.

23. H. Urakawa, S.E.F., H. Smidt, J. C. Smoot, E. H. Tribou, J. J. Kelly, P. A. Noble, D. A. Stahl, *Optimization of Single-Base-Pair Mismatch Discrimination in Oligonucleotide Microarrays.* Applied and Environmental Microbiology, 2003. **69**: p. 2848–2856.

24. Mardis, E.R., *Next-generation DNA sequencing methods.* Annu. Rev. Genomics Hum. Genet., 2008. **9**: p. 387–402.

25. A. A. Koshkin, S.K.S., P. Nielsen, V. K. Rajwanshi, R. Kumar, M. Meldgaard, C. E. Olsen, J. Wengel, *LNA (Locked Nucleic Acids): Synthesis of the Adenine, Cytosine, Guanine, 5-Methylcytosine, Thymine and Uracil Bicyclonucleoside Monomers, Oligomerisation, and Unprecedented Nucleic Acid Recognition.* Tetrahedron 1998. **54**: p. 3607-3630.

26. F. Silvia, B.J., M. Pedro, F. Céu, W. Jesper, A. N. Filipe, *Mismatch discrimination in fluorescent in situ hybridization using different types of nucleic acids.* Appl. Microbiol. Biotechnol. , 2015. **99**: p. 3961–3969.

27. V. V. Demidov, M.D.F.-K., *Two sides of the coin: affinity and specificity of nucleic acid interactions.* Trends in Biochemical Sciences 2004. **29**: p. 62-71.

28. B. C. Satterfield, M.B., J. A.A. West, M. R. Caplan, *Surpassing Specificity Limits of Nucleic Acid Probes via Cooperativity.* Journal of Molecular Diagnostics, 2010. **12**: p. 359-367.

29. A. Abi, E.E.F., *Electroanalysis of single-nucleotide polymorphism by hairpin DNA architectures.* Anal. Bioanal. Chem. , 2013. **405**: p. 3693–3703.

30. R. W. Roberts, D.M.C., *Specificity and stringency in DNA triplex formation.* Proc. Natl. Acad. Sci. USA, 1991. **88**: p. 9397-9401.

31. Kolpashchikov, D.M., *Triple-Stem DNA Probe: A New Conformationally Constrained Probe for SNP Typing.* ChemBioChem 2009. **10**: p. 1443-1445.

32. A. Piatek, S.T., A. C. Pol, A. Telenti, L.P. Miller, F. R. Kramer, D. Alland, *Molecular beacon sequence analysis for detecting drug resistance in Mycobacterium tuberculosis.* Nature Biotechnology, 1998. **16**: p. 359-363.

33. A. Tsourkas, M.A.B., G. Bao, *Structure±function relationships of shared-stem and conventional molecular beacons.* Nucleic Acids Research, 2002. **30**(19): p. 4208-4215

34. L. Cong, L.Y., J. Wanga, X. Tang, *A dumbbell molecular beacon for the specific recognition of nucleic acids.* Bioorganic and Medicinal Chemistry Letters, 2010. **20**: p. 6547-6550.

35. J. Grimes, Y.V.G., D. M. Kolpashchikov, *Real-Time SNP Analysis in Secondary Structure-Folded Nucleic Acids.* Angew Chem Int Ed Engl. , 2011. **49**: p. 8950–8953.

36. H. Kuhn, V.V.D., J. M. Coull, M. J. Fiandaca, B. D. Gildea, M. D. Frank-Kamenetskii, *Hybridization of DNA and PNA Molecular Beacons to Single-Stranded and Double-Stranded DNA Targets.* J. Am. Chem. Soc., 2002. **124**.

37. J. F. Hopkins, S.A.W., *Molecular beacons as probes of RNA unfolding under native conditions.* Nucleic Acids Research, 2005. **33**: p. 5763–5770.

38. L. E. Morrison, T.C.H.a.L.M.S., *Solution-phase detection of polynucleotides using interacting fluorescent labels and competitive hybridization.* Analytical Biochemistry 1989. **183**: p. 231-244.

39. Q. Li, G.L., Q. Guo, J. Liang, *A new class of homogeneous nuclei acid probes based on specific displacement hybridization.* Nucleic Acids Research, 2002. **30**: p. 2-9.

40. K-C. Luk, S.G.D., J. R. Hackett Jr, *Partially double-stranded linear DNA probes: Novel design for sensitive detection of genetically polymorphic targets.* Journal of Virological Methods 2007. **144**: p. 1-11.

41. D. Y. Zhang, G.S., *Dynamic Dna nanotechnology using stranddisplacement reactions.* Nature Chemistry, 2011. **3**: p. 103-113.

42. S. X. Chen, D.Y.Z., and G. Seelig, *Conditionally fluorescent molecular probes for detecting single base changes in double-stranded DNA.* Nat. Chem. , 2013. **5**: p. 1-16.

43. D. A. Khodakov, A.S.K., A. Linacre, A. V. Ellis, *Toehold-Mediated Nonenzymatic DNA Strand Displacement As a Platform for DNA Genotyping.* J. Am. Chem. Soc. , 2013. **135**: p. 5612−5619.

44. D. A. Khodakov, A.S.K., D. M. Huang, A. Linacre, A. V. Ellis, *Protected DNA strand displacement for enhanced single nucleotide discrimination in double-stranded DNA.* Scientific Reports 2014. **5**: p. 1-8.

45. N. Srinivas, T.E.O., S. Petr, J. M. Schaeffer, B. Yurke, A. A. Louis, J. P. K. Doye, E. Winfree, *On the biophysics and kinetics of toehold-mediated DNA strand displacement.* Nucleic Acids Research, 2013: p. 1-18.

46. L. Qian, E.W., J. Bruck, *Neural network computation with DNA strand displacement cascades.* Research Letter, 2011. **475**: p. 368-372.

47. S. Bhadra, Y.S.J., M. R. Kumar, R. F. Johnson, L. E. Hensley, A. D. Ellington, *Real-Time Sequence-Validated Loop-Mediated Isothermal Amplification Assays*

for Detection of Middle East Respiratory Syndrome Coronavirus (MERS-CoV). Plos One, 2011. **1**.

48. http://unafold.rna.albany.edu/, The DINAMelt Web Server.

49. S. A. Kushon, J.P.J., J. L. Seifert, H. Nielsen, P. E. Nielsen, B. A. Armitage, *Effect of Secondary Structure on the Thermodynamics and Kinetics of PNA Hybridization to DNA Hairpins.* J. Am. Chem. Soc. , 2001. **123**: p. 10805-10813.

50. G. Vesnaver, K.J.B., *Predicting DNA duplex stability from the base sequence.* Proc. Natl. Acad. Sci. U.S.A, 1991. **88**: p. 3569-3573.

51. Y. Gao, L.K.W., R. M. Georgiadis, *Secondary structure effects on DNA hybridization kinetics: a solution versus surface comparison.* Nucleic Acids Research, 2006. **34**: p. 3370–3377.

52. John S. Schreck1, Thomas E. Ouldridge2,3,*, Flavio Romano1, Petr ˇ Sulc4, Liam P. Shaw2, Ard A. Louis2 and Jonathan P.K. Doye1,*, *DNA hairpins destabilize duplexes primarily by promoting melting rather than by inhibiting hybridization.* Nucleic Acids Research, 2015. **43**: p. 6181–6190.

53. L.G. Kostrikis, S.T., M.M. Mhlanga, D.D. Ho, F.R. Kramer, *Spectral genotyping of human alleles.* Science, 1998. **279**: p. 1228-1229.

54. S. Tyagi, F.R.K., *Molecular Becons: Probes that fluoresce upon hybridization.* Nature Biotechnology, 1996. **14**: p. 303-308.

55. S. Tyagi, D.P.B., F.K. Kramer, *Multicolor molecular beacons for allele discrimination.* Nat Biotechnol, 1998. **16**: p. 49-53.

56. G. Orru, F.C., G. Faa, S. Pillai, C. Manieli, C. Montaldo, F. Pilia, G. Pichiri, V. Piras, P. Coni, *Rapid Multiplex Real-time PCR by Molecular Beacons for Different BRAF Allele Detection in Papillary Thyroid Carcinoma.* Diagn Mol Pathol, 2010. **19**: p. 1-8.

57. S. A. E. Marras, F.R.K., S. Tyagi, *Multiplex detection of single-nucleotide variations using molecular beacons.* Genetic Analysis: Biomolecular Engineering, 1999. **14**: p. 151-156.

58. J.C. Tan, J.J.P., A. Tan, J. C. Blain, T. J. Albert, N. F. Lobo, M. T. Ferdig, *Optimizing comparative genomic hybridization probes for genotyping and SNP detection in Plasmodium falciparum.* Genomics, 2009. **93**.

59. Klein, D., *Quantification using real-time PCR technology: applications and limitations.* Trends in Molecular Medicine, 2002. **8**: p. 257-260.

60. G. Goel, A.K., A.K. Puniya, W. Chen, K. Singh, *Molecular beacon: a multitask probe.* Journal of Applied Microbiology, 2005. **99**: p. 435–442.

61. H. el-Hajj, S.A.E.M., S. Tyagi, F. R. Kramer and a.d. alland1, *Detection of Rifampin Resistance in Mycobacterium tuberculosis in a Single Tube with Molecular Beacons.* Journal of Clinical Microbiology, 2001. **39**: p. 4131–4137.

62. A. Beloukas, D.P., C. Haida, V. Sypsa, A. Hatzakis, *Development and Assessment of a Multiplex Real-Time PCR Assay for Quantification of Human Immunodeficiency Virus Type 1 DNA.* Journal of Clinical Microbiology, 2009. **47**: p. 2194–2199.

63. G. Besson, M.K., *One-Step, Multiplex, Real-Time PCR Assay with Molecular Beacon Probes for Simultaneous Detection, Differentiation, and Quantification of Human T-Cell Leukemia Virus Types 1, 2, and 3.* JOURNAL OF CLINICAL MICROBIOLOGY, 2009. **47**: p. 1129-1135.

64. B. Faltin, R.Z., and F. von Stetten, *Current Methods for Fluorescence-Based Universal Sequence-Dependent Detection of Nucleic Acids in Homogenous Assays and Clinical Applications.* Clinical Chemistry, 2013. **59**: p. 1567-1582.

65. C.T. Wittwer, M.G.H., A.A Moss, R.P. Rasmussen *Continuous fluorescence monitoring of rapid cycle DNA amplification.* Biotechniques, 1997. **22**: p. 130-131.

66. K.J. Livak, S.J.F., J. Marmaro, W. Giusti, K.A. Deetz, *Oligonucleotides with fluorescent dyes at opposite ends provide a quenched probe system useful for detecting PCR product and nucleic acid hybridization.* PCR Methods Appl., 1995. **4**: p. 357-362.

67. D. Whitcombe, J.T., S.P. Guy, T. Brown, S. Little, *Detection of PCR products using self-probing amplicons and fluorescence.* Nat. Biotechnol., 1999. **17**: p. 804-807.

68. J.A.M Vet, B.J.M.V.d.R., H. J. Blom, *Molecular beacons: colorful analysis of nucleic acids.* Expert Rev. Mol. Diagn., 2002. **2**: p. 89-99.

69. S. A.E. Marras, S.T., F. R. Kramer, *Real-time assays with molecular beacons and other fluorescent nucleic acid hybridization probes.* Clinica Chimica Acta, 2006. **363**: p. 48 – 60.

70. S. A. E. Marras, F.R.K., S Tyagi, *Efficiencies of fuorescence resonance energy transfer and contact-mediated quenching in oligonucleotide probes.* Nucleic Acids Research, 2002. **30**(21): p. E122.

71. S. V. Balashov, R.G., S. Park,D. S. Perlin, *Rapid, High-Throughput, Multiplex, Real-Time PCR for Identification of Mutations in the cyp51A Gene of Aspergillus fumigatus That Confer Resistance to Itraconazole.* Journal of Clinical Microbiology,, 2005. **43**: p. 214-222.

72. S. A.E. Marras, F.R.K., S. Tyagi, *Multiplex detection of single-nucleotide variations using molecular beacons.* Genetic Analysis: Biomolecular Engineering, 1999. **14**: p. 151-156.

73. S. Chakravorty, B.A., M. Burday, M. Levi, S. A. E. Marra, D. Shah, H. H. El-Hajj, F. R. Kramer, D. Alland, *Rapid Universal Identification of Bacterial Pathogens from Clinical Cultures by Using a Novel Sloppy Molecular Beacon Melting Temperature Signature Technique.* Journal of Clinical Microbiology, 2010. **48**: p. 258–267.

74. J. J. Ely, A.R.-D., M.L. Campbell, S. Kohler, W.H. Stone, *Influence of Magnesium Ion Concentratio and PCR Amplification Conditions on Cross-Species PCR.* Biotechniques, 1998. **25**: p. 38-42.

75. C. Joo, S.A.M., D. M. J. Lilley, T. Ha, *Exploring Rare Conformational Species and Ionic Effects in DNA Holliday Junctions Using Single-molecule Spectroscopy.* J. Mol. Biol., 2004. **341**: p. 739–751.

76. D.L. Sokol, X.Z., P. Lu, A.M. Gewirtz, *Real time detection of DNA, RNA hybridization in living cells.* Proc. Natl Acad. Sci. USA, 1998. **95**: p. 11538–11543.

77. Poddar, S.K., *Symmetric vs asymmetric PCR and molecular beacon probe in the detection of a target gene of adenovirus.* Molecular and Cellular Probes, 2000. **14**: p. 25-32.

78. K. Barratt, J.F.M., *Improving Real-Time PCR Genotyping Assays by Asymmetric Amplification.* Journal of Clinical Microbiology, 2002. **40**: p. 1571–1572.

79. O. Henegariu, N.A.H., S.R. Dlouhy, G.H. Vance, P.H. Vogt, *Multiplex PCR: critical parameters and step-by-step protocol.* Biotechniques, 1997. **23**: p. 504-511.

80. X. Li, Y.H., C. Song, M. Zhao, Y. Li, *Several concerns about the primer design in the universal molecular beacon real-time PCR assay and its application in HBV DNA detection.* Anal Bioanal Chem, 2007. **388**: p. 979–985.